Dissertation
submitted to the
Combined Faculty of Natural Sciences and Mathematics
of Heidelberg University, Germany
for the degree of
Doctor of Natural Sciences

Put forward by
Severin Morris Meister
born in Stuttgart
Oral examination: October 20, 2021

Photoelectron spectroscopy of laser-dressed helium and sequentially ionized argon. Employing free-electron laser XUV radiation in the few-photon regime

Referees: Priv.-Doz. Dr. Robert Moshammer
              Apl. Prof. Dr. Andreas Wolf

Abstract: In this thesis, photoelectron spectroscopy in combination with extreme-ultraviolet (XUV) and infrared (IR) radiation is employed to investigate non-linear effects in rare gas atoms. Electrons are measured by means of a reaction microscope which allows to determine the particles' momentum vector in 4π solid angle.

The simultaneous interplay of XUV-photon absorption and an IR-dressing field in helium atoms allows ionization via resonances which are not accessible by single photon excitation. Scanning the XUV-photon energy between 20.4 eV and 24.6 eV reveals several ionization pathways for different combinations of XUV-photon absorption and IR-photon absorption or emission. Information about these states is encoded in the corresponding photoelectron angular distributions (PADs). PADs are analyzed for different orientations of polarization between the two radiation fields which allows to change the magnetic quantum number and to alter ionization pathways. Additionally, PADs are analyzed for changing laser-intensities which reveals Ponderomotive-/Stark shifts and higher order multiphoton effects.

Furthermore, two-photon double ionization (TPDI) in argon is investigated with intense FEL-XUV pulses. At a photon energy of 27.93 eV, we find sequential ionization to dominate and analyze the PAD of the two emitted photoelectrons. Despite the stepwise character of the process, we find both electrons being correlated via polarization of the intermediate ionic state. Moreover, PADs are found to be modulated by autoionizing states which have to be considered to properly describe the process.

Zusammenfassung: In dieser Arbeit wird Photoelektronenspektroskopie in Edelgasen in Kombination mit extrem ultravioletter (XUV) und Infrarotstrahlung genutzt, um nichtlineare Effekte zu untersuchen. Elektronen werden mit Hilfe eines Reaktionsmikroskopes gemessen, das es ermöglicht den Impulsvektor eines Teilchens in einem Raumwinkel von 4π zu bestimmen.

Das gleichzeitige Zusammenspiel aus XUV-Photonenabsorption und einem IR-dressing Feld in Heliumatomen ermöglicht die Ionisation über Resonanzen, die durch Einphotonenanregung nicht zugänglich sind. Durch einen XUV-Photonenenergiescan zwischen 20.4 eV und 24.6 eV werden verschiedene Ionisationspfade sichtbar, die durch XUV-Photonenabsorption und IR-Photonenabsorption bzw. Emission entstehen. Informationen über diese Zustände sind in den entsprechenden Photoelektronen-Winkelverteilungen kodiert. Diese werden für verschiedene Orientierungen der Polarisation zwischen den Strahlungsfeldern untersucht, wobei sich die magnetische Quantenzahl und Ionisationspfade ändern können. Zusätzlich werden Winkelverteilungen bei verschiedenen Laserintensitäten analysiert, um ponderomotive bzw. Stark-Verschiebungen und Multiphotoneneffekte höherer Ordnung zu untersuchen.

Des Weiteren wird die Zwei-Photonen Doppelionisation in Argon mit intensiven FEL-XUV-Pulsen untersucht. Bei einer Photonenenergie von 27.93 eV zeigen wir, dass sequentielle Ionisation dominiert und analysieren die Winkelverteilung des ersten und zweiten Elektrons. Trotz des schrittweisen Charakters finden wir, dass beide Elektronen über die Polarisierung des ionischen Zwischenzustandes korreliert sind. Außerdem wird gezeigt, dass die Winkelverteilungen durch autoionisierende Zustände moduliert werden und zur korrekten Beschreibung berücksichtigt werden müssen.

Mehr Licht ...

Johann Wolfgang von Goethes letzte Worte

Contents

Chapter 1

Introduction

Atomic physics is one of the fundamental areas of research in physics. Especially with the advent of a quantum description, atomic physics gained momentum and was employed as the working horse for new discoveries in the quantum world. The beginning of this era dates back over a hundred years, but is still present in state of the art research. A prominent role is given to the fundamental interaction between matter and light. Photons are the mediator of the electromagnetic force and efficiently couple to atomic systems as their constituents possess electric charges. The ubiquity of this interaction in the universe, in our ecosystem and the human body, to just name a few, has kept the research vital and growing. Over the recent decades the focus changed from static investigations to experiments which temporally resolve inner-atomic or molecular processes. The natural time scale for these small systems is typically located within the femtosecond (10^{-15} s) regime. Inter-atomic decay mechanisms or molecular dissociation can range from below 100 fs to several thousand femtoseconds [1, 2, 3], whereas fast inner-atomic processes like Auger or autoionization can exhibit life times of only several femtoseconds [4].

Real-time observations of these processes require radiation sources which provide pulse durations in the same time domain. At present there is a variety of sources to choose from, where each exhibits specific advantages and challenges. The development of new sources and the progress in atomic physics was often closely tied together. Knowledge about the atomic structure and its behavior upon electromagnetic radiation allowed to propose and to built a first laser. More recently developed sources based on high-harmonic generation (HHG) employ an elaborated photoelectron recollision mechanism to generate ultra-short ($<$ fs) pulses of small wavelength ($<$ 100 nm). Apart from atomic solutions for short-pulsed lasers there is the free-electron laser. Here electrons are accelerated to relativistic energies and emit electromagnetic radiation in an alternating magnetic field. Short pulse durations of several tens of femtoseconds can be achieved in combination with high intensities and large photon energies, which allows perform novel investigations.

An experimental realization of a time-resolved measurement is the pump-probe technique [5]. A first "pump" pulse triggers dynamics in the target while a temporally delayed second "probe" pulse stops the evolution and creates a measurable signal. By repeating the measurement with varying delays between pump and probe

pulses the evolution of certain dynamics can be sampled. The necessity of comparably short pulses is obvious in this scheme. If pulse durations exceed the life time of the considered process there is no defined start- and endpoint, so time-dependent signals vanish.

Another closely related field of investigation is non-linear processes triggered by multiphoton interaction. Absorbing multiple photons within the same target allows to examine matter under extreme conditions and test theory at new limits. This was demonstrated for example by stripping off many electrons of a xenon atom by a single intense X-ray pulse [6]. When multiphoton absorption is applied in a smart way it can be used to overcome certain limitations. Besides the previously mentioned delayed two-photon absorption to resolve dynamic processes, two-photon absorption can also be employed for Doppler-free spectroscopy [7, 8]. Another technique is resonance-enhanced multiphoton ionization (REMPI) [9, 10, 11], where electronic and vibronic states can be probed, which are not accessible by single photon absorption. The probability to absorb multiple photons within the same target increases with intensity of the radiation. This relation sets another requirement on the laser parameters and determines the most suitable radiation source. For all the processes and techniques mentioned above the wavelength of the employed radiation is a crucial quantity.

It not only determines the amount of deposited energy, but also has an impact on the prevailing ionization mechanism (Keldysh [12]) and on energy level shifts and splittings [13, 14]. Furthermore, as the wavelength is inversely proportional to the frequency, it also plays a role in dynamic phenomena like beatings. An overview about the electromagnetic spectrum is given in figure 1.1. Typical length and energy scales of routinely encountered radiation are illustrated, as well as the two energy regimes employed in this work. One regime is described as extreme ultraviolet (XUV) and lies between 10 nm and 124 nm (124 eV–10 eV). The other regime in this work is in the infrared (IR) that ranges from the red edge of the visible spectrum around 700 nm to 1000 μm ($\approx$ 1.8 eV to 1 meV).

The XUV regime covers the binding energy of valence electrons and the first lower-lying subshells. It also covers ionization potentials of low charge states and typical binding energies of molecules. Therefore the XUV regime can be considered as the realm of chemical and biological reactions which is fundamental to life on Earth. However, as interesting this regime appears as challenging it is to access in experiments. All elements exhibit large cross-sections in this energy range and therefore produce considerable background signals. In order to increase the signal to noise ratio, strict vacuum requirements and dense targets are essential. Another experimental challenge is the XUV light generation itself.
Currently there are three light sources to choose from: radiation from synchrotrons, HHG sources and free-electron lasers (FELs). While synchrotrons are a well-established
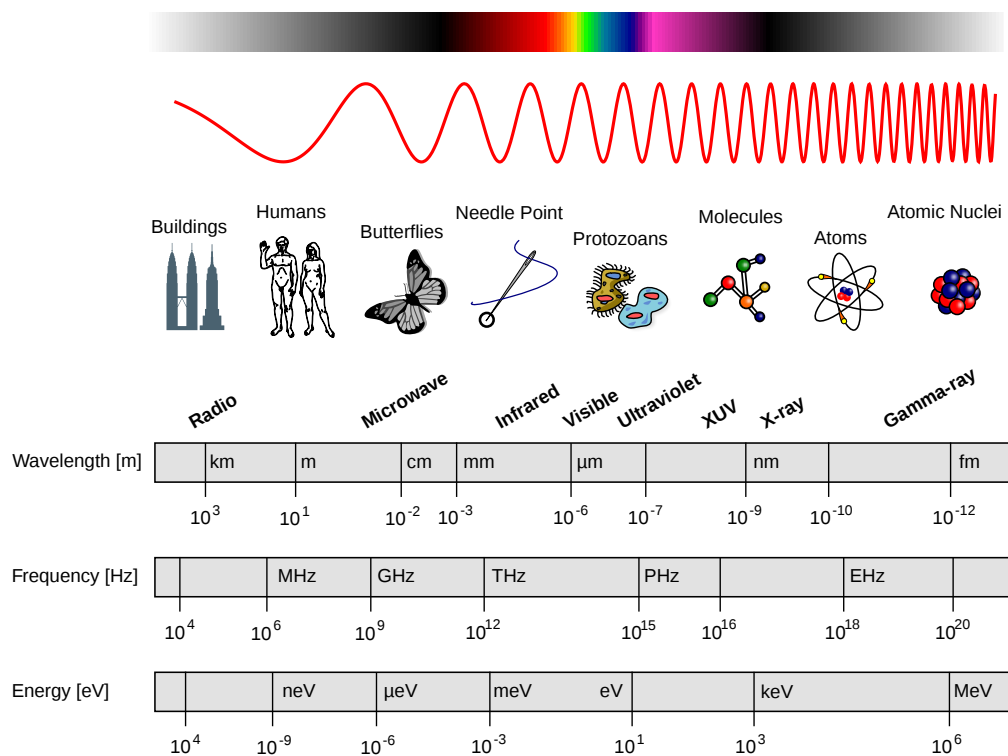
figure 1.1: *Electromagnetic spectrum. Comparison of length, time and energy scales. Adapted from [15].*

technique, FELs and HHG sources became available within the last 20 years. Synchrotron radiation can range from several electronvolts to the hard X-ray regime and exhibits a relatively small bandwidth. The radiation however is not coherent and large pulse durations hinder the investigation of dynamics. Furthermore, due to low intensities multiphoton processes can not be observed. In contrast, HHG-sources can provide ultra-short pulses down to sub-femtoseconds [16] with good coherence properties [17]. Despite short pulse durations, HHG-sources deliver intensities orders of magnitudes below FEL radiation, thus multiphoton processes are challenging to trigger. The photon energy range starts at several electronvolts and can go well beyond 100 eV [18, 19]. However, choosing a particular photon energy can be challenging as there is a comb of harmonics with a limited tuning capability. The third light source providing XUV radiation is the FEL, which will be employed in this work. FELs can deliver pulses of several tens of femtoseconds which is sufficient to investigate a variety of dynamics in atomic and molecular systems. The specialty of FEL radiation is the large intensity that can be achieved (cf. p.1225f [20]). This allowed for the first time to study multiphoton effects in the XUV and X-ray regime. Experimental challenges are the limited coherence and pulse-to-pulse instability. For some types of FELs a large

bandwidth and an uneven pulse structure has to be considered.

Within this work, three investigations have been published which contribute to the described field of research. In a first study (section 4.3), photoelectron emission from excited laser-dressed helium is analyzed. The simultaneous interplay of XUV and IR radiation allows to populate states of specific angular momentum which are not accessible by single photon ionization. Complementary transient absorption measurements referred to these states as "light-induced states" or "light-induced structures" (LIS) [21]. The experiment employed FEL-XUV radiation with tunable photon energy in combination with IR laser radiation of fixed photon energy 1.55 eV(800 nm). Various excited states can be accessed depending on the XUV energy, the IR intensity and the relative temporal delay between the two pulses. In the trivial case of preceding XUV pulses, helium atoms are excited from the $1s^2\,^1S$ ground state to $1snp\,^1P$ excited states, if the photon energy matches the transition energy. Following, the excited atom can get ionized upon photon absorption from the subsequent IR pulse. Emitted photoelectrons carry information about the excited state they are originating from. Therefore, by measuring the energy and the angular distribution of photoelectrons allows to finally assign the involved excited states. This principle is also applied to reveal and track excited states for the more complex situation of temporally overlapping pulses. In this case the helium atom is dressed by the IR radiation field during XUV photon absorption. This allows multiphoton excitations of the form: $He + \gamma_{\mathrm{XUV}} \pm N_{\mathrm{IR}}\,\gamma_{\mathrm{IR}} \Rightarrow He^*$, where N_{IR} is the number of IR photons γ_{IR} and He^* denotes the excited helium atom. The $\pm$ symbol accounts for the fact that IR photons can be absorbed by the helium atom, but can also be emitted to the dressing field in order to couple to an excited state. The various possibilities for transitions open up or close while scanning the XUV photon energy in the experiment. In order to obtain a measurable signal, the excited atom is ionized by absorbing additional IR photons and emitted photoelectrons are detected. Their analysis allows again to deduce involved excited states and their shift with laser intensity as well as the underlying excitation mechanisms.

The second successive investigation (section 4.4) exhibits the same experimental conditions than the first one, but additionally brings in the aspect of polarization. The XUV and IR radiation are both linearly polarized and can be rotated with respect to each other. In contrast to parallel orientation, an orthogonal orientation of polarizations allows to change the magnetic quantum number in a transition. In this way, an even larger variety of states can be accessed during the XUV photon energy scan. Relative polarization as an additional degree of freedom is also employed as a handle to switch on and off photoelectron emission. This is achieved as certain transitions obey selection rules which depend on the relative orientation of polarizations. The framework exhibits several aspects of the afore mentioned REMPI technique and can be seen as a model for extended REMPI-type measurements. The specialty of em-

ploying tunable XUV radiation in combination with an apparatus capable to measure complete kinematics gives extensive flexibility and allows a detailed investigation. Another aspect covered in this paper is the investigation of the transition region between the multiphoton ionization regime and the tunneling regime. When ionizing excited atoms, the transition region can be observed at lower IR intensities than for ground state ionization. Information about the process is gained by measuring the photoelectron angular distribution (PAD) in dependence of the IR intensity.

The third presented experiment covers electron correlation and the effect of autoionizing states in two-photon double ionization (TPDI). For this investigation atomic argon is irradiated with intense FEL-XUV radiation. The photon energy is chosen above the ionization threshold of Ar^+ where sequential ionization is found to dominate. The photoelectrons of the first and the second ionization step are found to be correlated via the polarized intermediate Ar^+ state. This is reflected in the observation that photoelectrons from single ionization exhibit a different angular distribution than the first step electrons in TPDI. Furthermore, autoionizing states in the Ar^+ continuum are found to impact the PAD of the second step electron decisively.

All three studies completely rely on the capabilities of the reaction microscope (REMI). It allows to measure the momentum of charged fragments in full 4π solid angle, which translates to angular and energy resolution. Furthermore, the fragments of a single reaction can be measured in coincidence, which can be essential to disentangle different reaction channels in the analysis. The general concept of a REMI and the REMI endstation at the free-electron laser in Hamburg (FLASH2) is presented in the publication in section 4.1. The paper also addresses experimental details like beam splitting, focusing and delaying, as well as the target injection and the detection scheme. Benchmarking measurements are also provided. A review about extensions to the REMI-endstation including an HHG-source and an IR laser are presented in a further publication in section 4.2. A selection of three exemplary experiments is also given to demonstrate the capabilities of the setup.

The thesis is structured in the following way: Chapter 2 contains the physical background and concepts which are essential for the presented experiments. Photoexcitation and photoionization is introduced by a perturbative ansatz. Both mechanisms are discussed for the extension to the multiphoton regime. Furthermore, intensity-dependent effects like tunnel ionization or the ponderomotive shift are introduced. Chapter 3 deals with the basic concept of a free-electron laser, its working principle and characteristic radiation. Chapter 4 contains five publications which are based on the work of this Phd project. The first two publications cover rather technical topics while the last three deal with investigations in helium and argon. A discussion and a summary of the results is given in Chapter 5.

Chapter 2

Physical Background

2.1 Absorption and emission of electromagnetic waves

In the following, a semi-classical approach to describe electric dipole transitions is presented. For the calculation we consider perturbation theory in first order, where the electromagnetic wave is treated as a small perturbation to the atom. This derivation is complied along the lines of [22] chapter 4.3 and 5.3.

In dipole approximation, the perturbation energy $\hat{U}(\boldsymbol{r}, t)$ is the product of the force on an electron in an electric oscillatory field $\boldsymbol{F} = -e_0 \boldsymbol{E}(\boldsymbol{r}, t)$ and the distance $\boldsymbol{r}$ between electron and nucleus:

$$\hat{U}(\boldsymbol{r}, t) = \boldsymbol{r} \cdot e_0 \boldsymbol{E}(\boldsymbol{r}, t) = -\boldsymbol{D} \cdot \boldsymbol{E}(\boldsymbol{r}, t), \tag{2.1}$$

where $\boldsymbol{D} = -e_0 \boldsymbol{r}$ is the effective electric dipole moment. The electric field of the wave can be expressed as:

$$\boldsymbol{E}(\boldsymbol{r}, t) = \frac{i}{2} E_0 \left(\boldsymbol{e}\, e^{i(\boldsymbol{kr}-\omega t)} - \boldsymbol{e}^*\, e^{-i(\boldsymbol{kr}-\omega t)} \right), \tag{2.2}$$

with the amplitude E_0 and the unity vector of polarization $\boldsymbol{e}$. As the wavelength λ is typically much larger than the size of the atom r_{atom}, i.e. $\boldsymbol{kr} \ll 1$, we can expand the exponential function and insert a 1 in first order:

$$\hat{U}(\boldsymbol{r}, t) = e_0 \boldsymbol{E}(\boldsymbol{r}, t) \cdot \boldsymbol{r} = \frac{i}{2} E_0 e_0\, \boldsymbol{r} \cdot \left(\boldsymbol{e}\, e^{-i\omega t} - \boldsymbol{e}^*\, e^{i\omega t} \right) \tag{2.3}$$

We want to derive the probability for the transition from state $|a\rangle$ to state $|b\rangle$. For this we have to approximate non-stationary states within the time-dependent Schrödinger equation. The time-dependent Hamilton operator $\hat{H}(t)$ is the sum of the stationary Hamilton operator $\hat{H}_0$ and the interaction $\hat{U}(\boldsymbol{r}, t)$ between electrons and the electromagnetic wave (cf. equation (2.3)):

$$\hat{H}(t) = \hat{H}_0 + \hat{U}(\boldsymbol{r}, t) \tag{2.4}$$

In order to find an ansatz for this Hamilton operator we make use of the stationary equation:

$$\hat{H}_0 \, \psi_j(\boldsymbol{r}) = \hbar \omega_j \, \psi_j(\boldsymbol{r}), \tag{2.5}$$

with the solution in zeroth order and trivial time dependence:

$$\Psi_j^{(0)}(\boldsymbol{r}, t) = \psi_j(\boldsymbol{r}) e^{-i\omega_j t} \tag{2.6}$$

This gives us the ansatz for solving equation (2.4):

$$\Psi(\boldsymbol{r}, t) = \sum_{j=0}^{\infty} c_j(t) e^{-i\omega_j t} \, \psi_j(\boldsymbol{r}) \tag{2.7}$$

This can be an exact solution, if the chosen set $\psi_j(\boldsymbol{r})$ is complete and if the summation runs over an arbitrary number of states. The probability to find the final state $\psi_j(\boldsymbol{r})$ at time t is: $p_j(t) = |c_j(t)|^2$, where the probability amplitude is denoted by $c_j(t)$.

For convenience we use the following notations: $\Psi(\boldsymbol{r}, t) \to |\Psi(t)\rangle$ and $\psi_j(\boldsymbol{r}) \to |j\rangle$. With this ansatz the time-dependent Schrödinger equation including the Hamilton operator of equation (2.4) can be written as:

$$\left[\hat{H}_0 + \hat{U}(\boldsymbol{r}, t) \right] |\Psi(t)\rangle = i\hbar \frac{\partial}{\partial t} |\Psi(t)\rangle \tag{2.8}$$

By inserting the definitions, multiplication of the target state $\langle b|$, and a differentiation, we obtain a system of linear differential equations:

$$\frac{d}{dt} c_b(t) = -\frac{i}{\hbar} \sum_j c_j(t) \, \langle b| \, \hat{U}(\boldsymbol{r}, t) \, |j\rangle \; e^{i(\omega_b - \omega_j)} \tag{2.9}$$

In order to find a solution we make use of the perturbation being small: $\langle \hat{H}_0 \rangle \gg \hat{U}(\boldsymbol{r}, t)$. For the initial state this leads to $c_a = 1$ while the other states show an insignificant change over time $|c_j(t)| \ll 1$ for $j \neq a$ and therefore are set to $c_j^0(t) \equiv 0$ in first order. The complete solution in first order reads:

$$|\Psi(t)\rangle \approx |a\rangle \, e^{-i\omega_a t} + \sum_{j \neq a} c_j(t) \, |j\rangle \, e^{-i\omega_j(t)} \tag{2.10}$$

By inserting in the differential equation (2.9) we obtain:

$$\frac{d}{dt} c_b(t) = -\frac{i}{\hbar} U_{ba}(t) \, e^{i\omega_{ba} t} \tag{2.11}$$

$$c_b(t) = \int_0^t U_{ba}(t') \, e^{i\omega_{ba} t'} dt', \tag{2.12}$$

where $\hat{U}_{\mathrm{ba}}(t) = \langle b| \hat{U}(\boldsymbol{r}, t) |a\rangle$ and $\omega_{\mathrm{ba}} = \omega_{\mathrm{b}} - \omega_{\mathrm{a}}$. In equation (2.12) the interaction is assumed to start at $t = 0$. The quantity c_{b} is the time-dependent transition amplitude in first order. Here we can insert the perturbation of equation (2.3) and introduce the transition operator $\hat{\mathcal{T}} = \boldsymbol{r} \cdot \boldsymbol{e} = -\boldsymbol{D} \cdot \boldsymbol{e}/e_0$ with $\hat{\mathcal{T}}_{\mathrm{ab}} = \langle a| \hat{\mathcal{T}} |b\rangle$:

$$c_b(t) = \frac{E_0 e_0}{2\hbar} \int_0^t \left(\hat{\mathcal{T}}_{ba} e^{i(\omega_{ba} - \omega)t'} - \hat{\mathcal{T}}_{ba}^* e^{i(\omega_{ba} + \omega)t'} \right) dt' \tag{2.13}$$

one-photon solution

$$\boxed{c_b(t) = \frac{E_0 e_0}{2\hbar} \left(\frac{\hat{\mathcal{T}}_{ba} e^{i(\omega_{ba} - \omega)t}}{i(\omega_{ba} - \omega)} - \frac{\hat{\mathcal{T}}_{ba}^* e^{i(\omega_{ba} + \omega)t}}{i(\omega_{ba} + \omega)} \right)} \tag{2.14}$$

This result serves already to draw general information on photon absorption and emission. The two terms in the brackets of equation (2.14) lead only to significant numbers if $\omega_{\mathrm{ba}} \pm \omega \approx 0$. In this case the exponential functions have a stationary phase and the denominators lead to large contributions. The frequency ω of the electromagnetic wave is defined positive, so there are two possibilities left for ω_{ba}:

$$\omega_{\mathrm{ba}} > 0 \quad \text{absorption} \tag{2.15}$$
$$\omega_{\mathrm{ba}} < 0 \quad \text{induced (stimulated) emission} \tag{2.16}$$

As the frequency ω can be written in terms of energy $E = \hbar\omega$, one can state that the energy of the electromagnetic wave has to match the energy difference of the two atomic levels for a transition to take place. In reality even laser light is not perfectly monochromatic, but has a finite bandwidth. In this case only a fraction of the spectrum drives the transition. Photo-excitation, i.e. an electronic transition upon photon absorption is an integral part for the experiments presented in Chapter 4.

Another information we can draw from the previous considerations is the laser intensity dependence in one-photon absorption or emission. The excitation probability is

$$R_{\mathrm{ab}}(t) = |c_{\mathrm{b}}(t)|^2 \propto E_0^2 \propto I. \tag{2.17}$$

This shows that the probability for one-photon processes scales linearly with the laser intensity. In the following, we extend the perturbative calculation to the next order which corresponds to two-photon absorption. In this case the intensity dependence of the excitation probability changes. The general relation for multiphoton absorption will also be discussed.

The two-photon solution can be obtained by inserting the first order solution of equation (2.13) into the differential equation (2.9):

two-photon solution

$$c_b(t) = -i \left(\frac{E_0 e_0}{2\hbar} \right)^2 \int dt \sum_{\text{k}} \left(\frac{\hat{\mathcal{T}}_{\text{bk}} \hat{\mathcal{T}}_{\text{ka}} \; e^{i(\omega_{\text{ba}} - 2\omega)t}}{\omega_{\text{ka}} - \omega} + \frac{\hat{\mathcal{T}}_{\text{bk}}^* \hat{\mathcal{T}}_{\text{k a}} \; e^{i\omega_{\text{ba}}t}}{\omega_{\text{ka}} - \omega} + \text{Em} \right) \quad (2.18)$$

By comparing to the first order solution one can already see how the two-photon solution is built up. The first term in the sum contains the exponent $(\omega_{\text{ba}} - 2\omega)$ with exactly twice the frequency of the perturbation to equate the energy difference between initial state $|a\rangle$ and final state $|b\rangle$. The denominators with $\omega_{\text{ka}} - \omega$ represent the energy difference of the initial state and an intermediate state $|k\rangle$. In general, the summation has to be extended over an infinite number of intermediate states. In practice, however one can stop after a few terms as the resonance denominator and the matrix elements $\mathcal{T}_{\text{ka}}$ lead to significant contributions for certain terms only.

In the process of two-photon absorption the intensity dependence of the excitation probability changes compared to the one-photon case in equation (2.17):

$$R_{\text{ab}}(t) = |c_{\text{b}}(t)|^2 \propto E_0^4 \propto I^2. \quad (2.19)$$

Here, the excitation probability scales quadratically with the laser intensity compared to the linearity in the one-photon process. As the cross-section of a two-photon process is relatively small, large intensities are needed to enter a regime where these events can be measured in an actual experiment.

Higher order solutions are found by following the same procedure as in the second order case. In general, the solution of the previous order can be used to solve the differential equation equation (2.9) and obtain the next higher order. In this way higher order solutions are produced iteratively. One can state a general case for multiphoton process where an atom 'At' is excited from the initial state $|a\rangle$ to the final state $|b\rangle$ by absorbing N photons:

$$\text{At(a)} + N\hbar\omega \rightarrow \text{At(b)} \quad (2.20)$$

For this general case the intensity dependence of the excitation probability reads

$$R_{\text{ab}}^{(N)} = \sigma_{\text{ba}}^{(N)} \, \Phi^N \propto I^N, \quad (2.21)$$

where $\sigma_{\text{ba}}^{(N)}$ is the generalized cross-section and $\Phi = I/\hbar\omega$ the photon flux. This equation demonstrates the scaling of higher order processes with intensity. Apparently these processes come experimentally into reach with increasing intensity. High-gain FELs can enter this region with their unique parameter combination (cf. Chapter 3), as they exhibit an unchallenged brilliance at simultaneously large photon energies. This characteristics of an FEL and multiphoton processes in general, play a central role in the publications presented in sections 4.3 to 4.5.

2.1.1 Selection rules

A photon exhibits a spin $s_{ph} = 1$. Relative to the propagation direction its spin has only two orientations $m_s = \pm 1$, which are referred to left and right helicity. The case of $m_s = 0$ does not occur due to the transversal nature of the massless photon. In the process of absorption or emission the total angular momentum $\hat{\boldsymbol{J}}$ and its projection is conserved for the combined system of atom and photon. Angular momentum of the atom (lower state: $\hat{\boldsymbol{J}}_a$, upper state $\hat{\boldsymbol{J}}_b$) and spin of the photon $\hat{\boldsymbol{S}}_{ph}$ couple like ordinary angular momenta in quantum mechanics.

$$\hat{\boldsymbol{J}}_a + \hat{\boldsymbol{S}}_{ph} = \hat{\boldsymbol{J}}_b = \hat{\boldsymbol{J}} \tag{2.22}$$

Here the equation can be read from the left for absorption and from the right for emission. The three possibilities of vector addition are illustrated in figure 2.1. The eigenvalues of operators $\hat{\boldsymbol{J}}$ are denoted with j, where j_b can take the values $j_a + 1$, j_a and $j_a - 1$. However from $j_a = 0$ there is just the transition to $j_b = 1$ allowed.
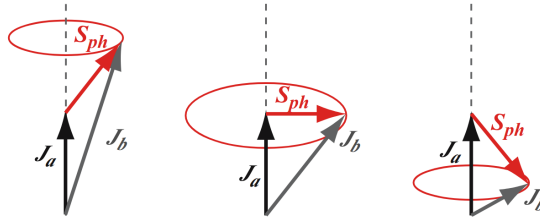
figure 2.1: *Addition of angular momenta of the initial state $\hat{\boldsymbol{J}}_a$, final state $\hat{\boldsymbol{J}}_b$ and the photon spin $\hat{\boldsymbol{S}}_{ph}$. Taken from [22].*

Furthermore the projection m of the atomic angular momentum can only change by certain values according to the photons polarization: $\Delta m = 1$ left circularly polarized, $\Delta m = -1$ right circularly polarized and $\Delta m = 0$ for linearly polarized[1] photons. The allowed changes of quantum numbers in a one-photon absorption process can be summarized in:

$$
\begin{array}{lll}
& \Delta j = 0, \pm 1 \quad (\text{where } 0 \leftrightarrow 0 \text{ is forbidden}) & (2.23) \\
\text{E1 selection rules} \Rightarrow & \Delta l = \pm 1 & (2.24) \\
& \Delta m = 0, \pm 1 & (2.25)
\end{array}
$$

---

[1]The case of $\Delta m = 0$ refers to a different coordinate system than the two other cases, due to the transversality of photons

In multiphoton absorption these selection rules change, as each photon carries angular momentum with a specific polarization. In the case of two-photon absorption both angular momenta can cancel each other leading to $\Delta l = 0$ for the atom. They also can add up leading to $\Delta l = \pm 2$. The magnetic quantum number m can take values up to $|\Delta m| = 2$. The resulting restrictions on the so called electric quadrupole transitions can be summarized in:

$$\text{E2 selection rules} \Rightarrow \quad \begin{array}{l} \Delta l = 0, \pm 2 \\ \Delta m = 0, \pm 1, \pm 2 \end{array}$$

(2.26)

(2.27)

There are various combinations in a two-color absorption process where each photon can have an individual polarization. Different scenarios with their allowed quantum numbers are given in reference [23]. Absorption processes with even more photons follow the same logic as described in the two-photon case, where photon momenta can cancel or add up.

2.2 Photoionization of atoms

The previous section covers electronic transitions in an atom between bound states. In this section we we focus on the transition of an electron from a bound state into the continuum, i.e. the emission of a photoelectron. For an electron to be emitted from an atom, a specific minimal amount of energy has to be deposited within the atom. This minimum energy corresponds to the binding energy of the electron and is often referred to ionization energy or ionization potential I_p.

Along the lines of excitation, the process of ionization can be described as a transition from an initial bound state $|a\rangle = |nl\rangle$ to a continuum state $|b\rangle = |\epsilon \ell'\rangle$ by the absorption of a photon with energy $\hbar\omega$. For simplicity, the electron spin is neglected in the following description as it is usually conserved in the one electron system we are considering. The initial state is described by the principal quantum number n and the orbital momentum ℓ while the continuum state is characterized by the kinetic energy $\epsilon = \hbar^2 k_\text{e}^2/(2m_\text{e})$ of the electron and its orbital momentum ℓ'. The photoionization of an atom 'At' can be written as:

$$\text{At}(n\ell) + \hbar\omega \rightarrow \text{At}^+ + e^-(\epsilon\ell')$$

(2.28)
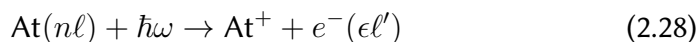
$$\text{with the energy relation:} \quad \epsilon = \hbar\omega - I_\text{p}$$

(2.29)

The cross-section for photoionization can be formulated similar to the absorption cross-section:

$$\sigma_{\epsilon a}(\hbar\omega) = 4\pi^2 \alpha \hbar\omega |\hat{\mathcal{T}}_{\epsilon a}|^2$$

(2.30)

Here, the transition matrix element $\hat{\mathcal{T}}_{\epsilon a} = \langle\epsilon|\,\hat{\mathcal{T}}\,|a\rangle$ is defined between the discrete initial state $|a\rangle$ and the continuum state $|\epsilon\rangle$. This expression can be simplified by applying the Born approximation. It is valid for large but not relativistic photon energies: $I_{\mathrm{p}} \ll \hbar\omega \ll m_{\mathrm{e}}c^2$. This allows to approximate the continuum wavefunction as a plane wave

$$\langle\boldsymbol{r}|\boldsymbol{k}_{\mathrm{e}}\rangle = \sqrt{\frac{m_{\mathrm{e}}k_{\mathrm{e}}}{(2\pi)^3\hbar^2}}\,e^{i\boldsymbol{k}_{\mathrm{e}}\boldsymbol{r}} \tag{2.31}$$

where the square root represents a normalization factor.

The geometry of the ionization process is illustrated in figure 2.2. The electromagnetic wave propagates along the z-direction exhibiting the wave vector $\boldsymbol{k}$. The polarization vector $\boldsymbol{e}$ of the linearly polarized radiation is oriented along x-direction. The electron is emitted along $\boldsymbol{k}_{\mathrm{e}}$.
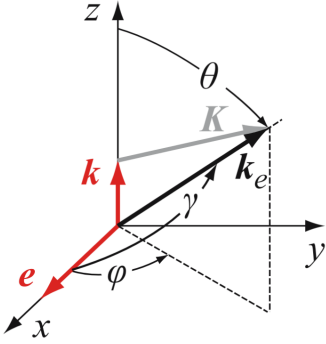
figure 2.2: *Geometry of the ionization process. Taken from [22].*

As we assumed large photon energies we no longer use the dipole approximation but the exact definition of the transition operator: $\hat{\mathcal{T}} = \frac{1}{\omega m_{\mathrm{e}}}e^{i\boldsymbol{k}\boldsymbol{r}}\,\boldsymbol{e}\cdot\hat{\boldsymbol{p}} = \frac{1}{\omega m_{\mathrm{e}}}e^{i\boldsymbol{k}\boldsymbol{r}}\,\hat{p}_{\mathrm{e}}$. With this expressions the matrix element for photoionization of state $|a\rangle$ can be written as:

$$\hat{\mathcal{T}}_{\epsilon a} = \langle\boldsymbol{k}_{\mathrm{e}}|\,\hat{\mathcal{T}}\,|a\rangle = \langle\boldsymbol{k}_{\mathrm{e}}|\,\frac{1}{\omega m_{\mathrm{e}}}e^{i\boldsymbol{k}\boldsymbol{r}}\,\hat{p}_{\mathrm{e}}\,|a\rangle \tag{2.32}$$

$$= \langle\hat{p}_{\mathrm{e}}\boldsymbol{k}_{\mathrm{e}}|\,\frac{1}{\omega m_{\mathrm{e}}}e^{i\boldsymbol{k}\boldsymbol{r}}\,|a\rangle \tag{2.33}$$

The last rearrangement is allowed because $\hat{p}_{\mathrm{e}} \parallel \boldsymbol{e} \perp \boldsymbol{k}$, so $\hat{p}_{\mathrm{e}}$ and $e^{i\boldsymbol{k}\boldsymbol{r}}$ mutually commute. Eigenvalues of $\hat{p}_{\mathrm{e}}$ are $p\cos(\gamma) = \hbar k_{\mathrm{e}}\cos(\gamma)$. By inserting equation (2.31) we obtain

$$\hat{\mathcal{T}}_{\epsilon a} = \langle\boldsymbol{k}_{\mathrm{e}}|\,\hat{\mathcal{T}}\,|a\rangle = \left(\frac{k_{\mathrm{e}}}{2\pi}\right)^{3/2}\frac{\cos(\gamma)}{\omega\sqrt{m_{\mathrm{e}}}}\int e^{i(\boldsymbol{k}-\boldsymbol{k}_{\mathrm{e}})\cdot\boldsymbol{r}}\psi_{\mathrm{a}}(\boldsymbol{r})\,d^3\boldsymbol{r}, \tag{2.34}$$

which can be further simplified by introducing $\boldsymbol{K} = \boldsymbol{k}_{\mathrm{e}} - \boldsymbol{k}$, so the integral can can be identified as a Fourier transformation

$$\psi_{\mathrm{a}}(\boldsymbol{K}) = (2\pi)^{-2/3}\int e^{-i\boldsymbol{K}\boldsymbol{r}}\psi_{\mathrm{a}}(\boldsymbol{r})\,d^3\boldsymbol{r}. \tag{2.35}$$

The differential cross-section for photoionization in Born approximation can be

stated by inserting equation (2.34) in equation (2.30):

$$d\sigma_{\epsilon a}(\hbar\omega) = 4\pi^2 \, \frac{\alpha}{\omega} \frac{\hbar k_e^3}{m_e} \cos^2(\gamma) |\psi_a(\boldsymbol{k}_e - \boldsymbol{k})|^2 \, d\Omega \qquad (2.36)$$

If we restrict our consideration to initial states with $s = 0$ and hydrogen-like atoms, we can use the following wavefunction for large $K = |\boldsymbol{k}_e - \boldsymbol{k}|$ after Bethe and Salpeter [24]

$$\psi(\boldsymbol{k}_e - \boldsymbol{k}) = \frac{2\sqrt{2}Z^{5/2}}{\pi n^{3/2}} \frac{a_0^{3/2}}{a_0^4 \, |\boldsymbol{k}_e - \boldsymbol{k}|^4} \qquad (2.37)$$

By taking this wavefunction in combination with assumptions like $\hbar\omega \approxeq \epsilon = \hbar^2 k_e^2/(2m_e)$, $v/c \ll 1$ and neglecting terms of $(k/k_e)^2$, we can come up with:

$$d\sigma_{\epsilon a}(\hbar\omega) = 64 \, a_0^2 \, \alpha \, \frac{Z^5}{n^3} \frac{\cos^2(\gamma) \left(1 + 4\frac{v}{c}\cos(\theta)\right)}{(2\epsilon/E_h)^{7/2}} \, d\Omega \qquad (2.38)$$

An integration of the solid angle yields the **integral photoionization cross-section in Born approximation for hydrogen-like atoms in** ns **states**:

$$\boxed{\sigma_{\epsilon ns}(\hbar\omega) = \frac{256\pi}{3} \, \alpha \, \frac{Z^5}{n^3} \frac{a_0^3}{(2\hbar\omega/E_h)^{7/2}}} \qquad (2.39)$$

This formula already describes the scaling of several fundamental quantities in photoionization. Remarkable for the photoionization cross-section is the strong dependence on the photon energy $(\hbar\omega)^{-7/2}$. Photoionization sets in and is maximal at the ionization threshold (in this case denoted with $E_h = 13.6\,\text{eV}$) and decreases fast with increasing photon energy. The photoionization cross-section shows also a strong dependence on the atomic number Z^5, so larger atoms can exhibit considerable values compared to lighter ones. Furthermore, the cross-section scales with n^{-3}, which leads to a decreased probability to ionize higher orbitals. Even though the findings are within the Born approximation for hydrogenic atoms, the principal behavior perpetuates also for atoms deviating from these assumptions.

2.2.1 Multiphoton ionization

Along the lines of multiphoton excitation in section 2.1, ionization can be triggered by multiphoton absorption as well. While the energy of a single photon is smaller than the ionization potential of the atom, the sum energy of multiple photons can exceed the threshold energy and ionization can take place. In this process, the lightweight photoelectron takes almost the entire excess energy. This energy is specific to experimental conditions and depends on the photon energy $\hbar\omega$ and the number N of
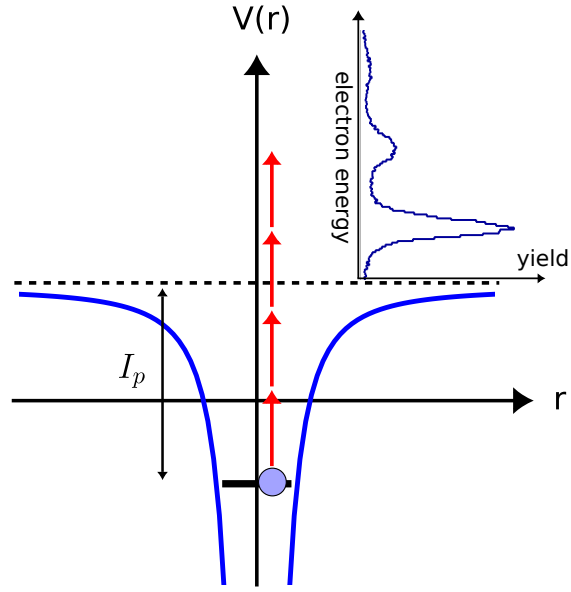
figure 2.3: *Multiphoton ionization: Atomic potential V(r) in blue with an electron in a bound state. The ionization potential I_p is indicated with the dashed line. The extra absorbed photons are imprinted in the photoelectron energy spectrum shown in the inset.*

involved photons. A schematic of multiphoton ionization is illustrated in figure 2.3. In this illustration the absorption of three photons (red arrows) is sufficient to ionize the atom. For large intensities however, there is an increasing probability for the atom to absorb more photons than required to surpass the ionization potential I_p. This process is called above-threshold ionization (ATI) [25, 26] and can be observed in the photoelectron energy spectrum. The extra energy of the additional photons is given to the photoelectron, so its kinetic energy spectrum ϵ_{kin} shows peaks with a spacing of just the photon energy. These peaks, often dubbed as "ATI-peaks", are depicted in the top right corner of figure 2.3.

Similar to the single photon ionization in equation (2.28) we can state the reaction and the energy balance for the multiphoton case:

$$\mathrm{At} + \mathrm{N}\,\hbar\omega \rightarrow \mathrm{At}^+ + e^-\left(\epsilon_{kin}\right) \tag{2.40}$$
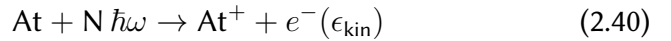
$$\text{with the energy relation:} \quad \epsilon_{kin} = \mathrm{N}\,\hbar\omega - I_p \tag{2.41}$$

The transition probability $R^{\mathrm{N}}_{\epsilon \leftarrow a}$ in multiphoton ionization scales with intensity analog to multiphoton excitation in equation (2.21). The transition from an initial bound

state $|a\rangle$ to a continuum state $|\epsilon\rangle$ in N^{th} order perturbation scales:

$$R_{\epsilon \leftarrow a}^{(N)} = \sigma^{(N)}\, \Phi^N \propto I^N \tag{2.42}$$

Where Φ is again the photon flux and $\sigma^{(N)}$ a generalized cross-section.

With the advent of high-gain FELs which deliver pulses of high intensity, it became feasible to perform experiments where multiple XUV or X-ray photons are absorbed within one atom. With this combination of large photon energies and high intensities atoms can be brought to high ionization states A^{N+} [27]. There are two mechanisms of reaching higher ionization states: Sequential ionization (SI) and non-sequential ionization (NSI) (Exp. [28] and theory paper therein). Sometimes NSI is also referred to as direct ionization.
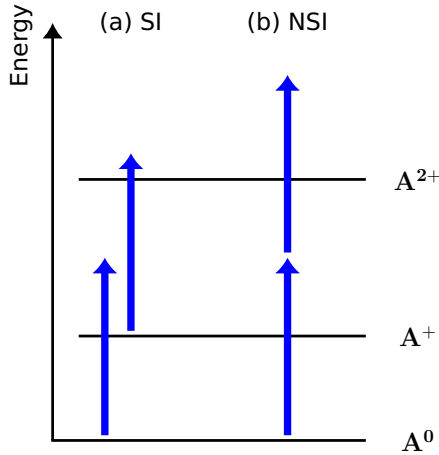
figure 2.4: *(a) Sequential ionization (b) Non-sequential ionization*

In SI the atom traverses every lower ionization state on the way to the final ionization state (cf. figure 2.4 (a)). The stepwise character of SI leads to specific signatures which allows to distinguish it from NSI. As the atom resides in an intermediate ionization state, the successive absorption of photons can be delayed. Furthermore, the excess energy above each ionization threshold is given to the respective emitted electron. It exhibits a characteristic value which depends on the ionization potential and the photon energy. On the contrary, in NSI higher ionization states are reached directly. Multiple photons are absorbed within a tiny amount of time which is governed by the Heisenberg uncertainty principle. In a short enough time interval the energy spread of photons can increase and an overlap with ionization thresholds can be established. For the case depicted in figure 2.4 (b), a signature of NSI is the energy sharing between the two emitted electrons [29].

Which mechanism is dominating cannot be stated in general as it depends on the photon energy regime, but also on the specific combination of target atom and photon energy. In the X-ray regime SI was shown to prevail [30], while in the XUV regime NSI can also have a considerable contribution [28]. Moreover, there are additional effects which demand a more complex description of reaching high charge states. For example X-ray photons can exhibit large cross sections for inner-shell ionization, which is typically followed by a cascade of Auger electrons [31]. Resonances can also play a

decisive role in the process of reaching high ionization states, especially if the energy of a single photon is smaller than the next ionization threshold [6]. In many cases, NSI involves less photons than SI to reach the same ionization state [29]. This can be a decisive factor as the ion yield Y scales with the intensity I as $Y \propto I^N$, where N is the number of photons [32]. It can be shown that for low intensities NSI can be the dominating mechanism while at high intensities SI ionization is expected to dominate [33].

The differentiation between the two mechanisms will be crucial for the experiment on the two photon double ionization in argon which is presented in section 4.5.

2.2.2 Photoelectron angular distribution

The differential photoionization cross-section in equation (2.38) already shows the angular dependency of emitted electrons. For linearly polarized light the angular dependence is mainly governed by $\cos^2(\gamma) = \sin^2(\theta)\cos^2(\varphi)$, with γ being the angle between the electron emission direction and the polarization axis. The term $4\frac{v}{c}\cos(\theta)$ in equation (2.38) is just relevant for large photon energies and can be omitted for non-relativistic electrons. In strict dipole approximation for the here assumed E1 transition we can formulate the differential cross-section of photoionization:

$$\text{single photon ionization:} \qquad \frac{d\sigma_{\epsilon a}}{d\Omega} = \frac{\sigma_{\epsilon a}}{4\pi}\left[1 + \beta_2\,P_2(\cos\gamma)\right] \qquad \text{where } -1 \leq \beta_2 \leq 2$$

(2.43)

Here, the second Legendre Polynomial $P_2(\cos\gamma) = (3\cos^2\gamma - 1)/2$ contains the angular dependence and the coefficient is the anisotropy parameter β_2. In the case of an ns initial state, the anisotropy parameter is $\beta_2 = 2$ and equation (2.38) yields the same result as this representation. Electron emission is then found along the polarization axis and vanishes perpendicular to it. The angular distribution of this continuum state corresponds to a p-orbital. In general for low energies in photoionization, the continuum states are equivalent to excited states as described in section 2.1.

In the case of multiphoton ionization the complexity of the differential cross-section increases. The angular momenta of photons can add up or cancel each other and in general different polarizations have to be considered. Furthermore, for resonant intermediate states saturation effects have to be considered. A plain formulation [34, 35, 36] can be given for multiphoton ionization with linearly polarized light without saturating intermediate states:

$$\text{multiphoton ionization:} \qquad \frac{d\sigma_{\epsilon a}}{d\Omega} = \frac{\sigma_{\epsilon a}}{4\pi}\left[1 + \sum_{n\in\mathbb{N}} \beta_{2n}P_{2n}(\cos\gamma)\right] \qquad (2.44)$$

2.2.3 Tunnel ionization

For very large laser intensities the mechanism of multiphoton ionization is superseded by tunnel ionization. In this regime the electric field strength of the electromagnetic wave gets comparable to the Coulomb potential of the atom. Bound electrons experience a distorted atomic potential V(r) as illustrated in figure 2.5. For a sufficiently strong distortion the electron can escape the atomic potential by tunneling through the remaining potential barrier.

figure 2.5: *Tunnel ionization: Atomic potential V(r) in blue is distorted by the electric field of the electromagnetic wave. The bound electron can escape the atomic potential by tunneling through the potential barrier.*

A description to quantify the transition from the multiphoton regime to the tunneling regime was first introduced by Keldysh [12]. The essential parameters like the frequency ω and the maximum field strength E_0 of the electromagnetic field and the ionization potential I_p of the atom are combined in the Keldysh parameter:

$$\gamma = \frac{\sqrt{2\,I_p}\,\omega}{E_0} \tag{2.45}$$

The magnitude of γ determines the prevailing regime. For $\gamma \gg 1$ multiphoton ionization is the dominating process, while for $\gamma \ll 1$ the tunneling regime is prevailing. The classification by the Keldysh parameter is not a strict law, but rather gives a good estimate and describes the scaling with parameters.

For even larger intensities the atomic potential can be distorted in such a way that there is no potential barrier left for the electron. It can escape the atomic potential

without the need of tunneling through a potential barrier. This process is referred to as over-the-barrier ionization.

2.2.4 Ponderomotive shift

If an atom is ionized by an intense and long wavelength laser pulse, photoelectrons are measured at a lower kinetic energy than expected by simply taking the energy difference between ionization potential and photon energy [37]. This shift in photoelectron kinetic energy is referred to as the ponderomotive shift. As the emitted electron finds itself in the strong alternating electric field of the electromagnetic wave, it performs an oscillatory motion. The energy stored within this motion is called the ponderomotive potential. The excess energy in photoionization is split between the ponderomotive potential and the kinetic energy of the linear electron motion. Under certain experimental conditions the ponderomotive potential is lost and the measured photoelectron energy is lowered.

In order to determine if the ponderomotive potential is lost or recovered by the photoelectron, its motion within the pulse has to be considered. As described in [38] we differentiate between two cases, where the relevant parameters are the pulse duration τ, the transversal beam diameter d and the linear average motion of the electron v_a:

If $\tau \gg d/v_\mathrm{a}$, the pulse duration is so large that the electron has left the pulse region before the pulse is over. The beam can be considered as stationary and the electron will be accelerated by the electric field gradient when leaving the pulse. In this case the ponderomotive potential is conservative and the energy of the oscillatory motion is recovered by the photoelectron. Consequently, there is no ponderomotive shift measured at the detector which is located outside the light field [39].

If $\tau \ll d/v_\mathrm{a}$, the electron remains within the pulse region as long as it interacts with the pulse. In this case the ponderomotive potential is time dependent and the energy is not conserved. The energy which is stored in the oscillatory motion will be lost when the pulse leaves the atom. Consequently, the measured photoelectron energy is lowered in the order of the ponderomotive potential.

The ponderomotive potential leads not only to a shift of photoelectron peaks but also to a broadening of them. The broadening however is an accumulative effect of differently pronounced energy shifts between single photoionization events. The broadening can originate from spatial and from temporal characteristics of the laser pulse. If an electron is emitted in the high-intensity region of the laser focus the ponderomotive shift is larger than in a low-intensity region. If ionization takes place at the rising edge of the laser pulse, the emitted electron experiences a lower intensity as for ionization in the pulse maximum. Both scenarios together translate to a broadening of photoelectron kinetic energy peaks.

A quantitative description of the ponderomotive potential U_p can be obtained by classical considerations. For them to be applicable, we assume the photon wavelength to be much larger than the region of space where the photoionization process takes place [38]. The derivation of U_p is straightforward and can be found for example in [22] chapter 8.5.1:

The equation of motion of a free electron in an oscillatory electrical field can be stated as

$$m_\mathrm{e}\frac{dv}{dt} = e_0 E_0 \, \cos(\omega t), \tag{2.46}$$

where E_0 is the amplitude of the electrical field with frequency ω. The velocity follows as

$$v(t) = \frac{e_0 E_0}{m_\mathrm{e}\omega} \, \sin(\omega t) \tag{2.47}$$

and the electrons kinetic energy is accordingly:

$$\frac{1}{2}m_\mathrm{e}v^2 = \frac{e_0^2 E_0^2}{2m_\mathrm{e}\omega^2} \, \sin^2(\omega t). \tag{2.48}$$

The mean energy which is stored within the oscillatory quiver motion of the electron is called ponderomotive potential:

$$U_\mathrm{p} = \overline{\frac{1}{2}m_\mathrm{e}v^2} = \frac{e_0^2 E_0^2}{2m_\mathrm{e}\omega^2} \, \overbrace{\frac{1}{T}\int_t^{t+T}\sin^2(\omega t)dt}^{=1/2} \tag{2.49}$$

$$\boxed{\Rightarrow U_\mathrm{p} = \frac{e_0^2 E_0^2}{4m_\mathrm{e}\omega^2} \propto I\lambda^2} \tag{2.50}$$

The ponderomotive potential exhibits a quadratic dependence on the laser wavelength λ and scales linearly with the laser intensity I. In order to obtain an estimate of a typical U_p magnitude we consider the widely-used Ti:Sa laser wavelength of $\lambda = 800\,\mathrm{nm}$ at an intensity of $I = 10^{14}\,\mathrm{W/cm^2}$. This yields $U_\mathrm{p} \approx 6\,\mathrm{eV}$, which is a considerable energy and comparable for example to binding energies in an atom. The ponderomotive shift is closely related to the dynamical Stark effect which leads to an energy shift of bound states.

An illustrative example of the ponderomotive shift in photoionization is shown in figure 2.6. The ponderomotive shift can be depicted by an increase of the continuum threshold with intensity. Bound states are described in the context of the AC Stark shift and shifted as well, but the magnitude depends on the binding energy [40]. Lower
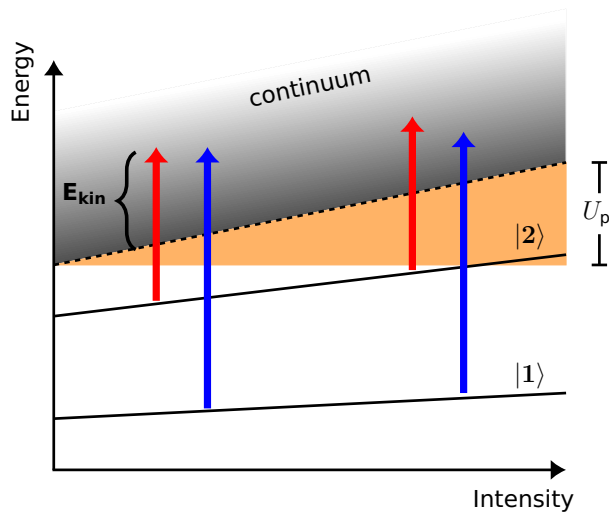
figure 2.6: *Impact of the ponderomotive potential U_p in photoionization. Ionizing from state$|1\rangle$ (blue photons) at different laser intensities leads to distinctly differing measured kinetic energies E_{kin} of the photoelectron. Ionizing from a higher lying state $|2\rangle$, which is more affected by the laser field, leads to a smaller measured kinetic energy shift.*

lying states $|1\rangle$ are less affected than higher lying states $|2\rangle$. As described above, the excess energy in photoionization is split between the kinetic energy of the photoelectron and the ponderomotive potential. U_p increases with intensity and consequently the kinetic energy share E_{kin} decreases. This effect is most prominent if the atom is ionized from a strongly bound state $|1\rangle$. This scenario is depicted in figure 2.6 for the two photoionization cases (blue photons) at different intensities. Ionizing at higher intensities leads to a lower measured photoelectron kinetic energy.

If the atom is ionized from a higher lying state $|2\rangle$ the kinetic energy shift with intensity is lower compared to the previous case. Ionization from state $|2\rangle$ for low and high intensity is illustrated by the red arrows in figure 2.6. E_{kin} differs by just a small amount compared to ionization from state $|1\rangle$.

Chapter 3

Free-electron Laser

This section provides background information on the free-electron laser which is employed for the investigations in sections 4.3 to 4.5. Detailed information on the the remaining setup, i.e. the REMI endstation, including the REMI working principle, optics, detectors and data acquisition is provided in the publication of section 4.1 and is not repeated in this section.

The word laser is an acronym for "**l**ight **a**mplification by **s**timulated **e**mission of **r**adiation". The process to generate laser radiation is partly described in the acronym. In brief, a gain medium (gas, solid, ...) is electronically excited by an external energy source and placed inside a cavity. Single atoms of the gain medium can de-excite in a statistical process called spontaneous emission. The characteristic energy of the excitation is released in form of a photon. Inside the cavity this photon can hit another excited atom which de-excites and emits an identical photon. This process is called stimulated emission. Both photons are still present in the cavity and can further trigger stimulated emission in excited atoms. A cascade of stimulated emission processes takes place generating an exponential amplification of light. Stimulated emission ensures all photons to exhibit a fixed phase relation which translates to coherence, a specific laser radiation property.

Conventional lasers have in common to work with a gain medium. The name of the laser indicates the category of material being used. For example there are gas lasers, dye lasers, metal-vapor lasers, solid-state lasers and semiconductor lasers.

A completely different mechanism to generate laser-like radiation is pursued in free-electron lasers. In this case, free electrons are brought to relativistic energies where they start to emit electromagnetic radiation upon periodic transverse acceleration. The radiation exhibits certain conventional laser characteristics like a small bandwidth, coherence to a certain degree and low beam divergence. Beyond that, FELs provide some unique features. For example, the photon energy is not restricted to specific transitions in a gain medium, but can be chosen continuously within the specifications of a given FEL. Moreover, FELs allow to enter parameter regions which are not accessible to other light sources. Particularly interesting is the combination of high intensities and large photon energies. It allows to trigger non-linear effects (e.g. multiphoton absorption) in atoms and molecules in an unprecedented energy region.
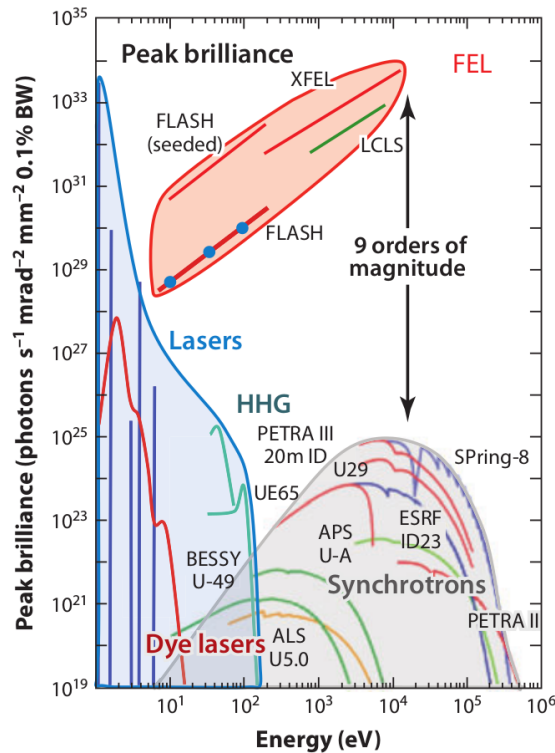
figure 3.1: *Performance overview of different light sources. Taken from [42]*

An overview of different light sources with their characteristic ranges of brilliance [1] in dependence of their photon energy is shown in figure 3.1.

The following passage gives an introduction to the working principle and radiation characteristics of FELs.

The first to describe the principles of a free-electron laser was Madey in 1971 [43]. Later on in 1981, the first scheme for high-gain FELs in the soft X-ray regime was proposed [44]. The first short wavelength FEL-facility to open for user operation was the free-electron laser in Hamburg (FLASH) in 2005 [45]. Up to date there are many other FELs working around the world[2] or being under construction[3].

Free-electron laser pulses are generated by a highly relativistic electron bunch which emits synchrotron radiation when brought to a sinusoidal motion perpendicular to

---

[1]Brilliance is a quality measure of X-ray sources. It comprises the number of photons per second related to the angular divergence of the beam, its cross-sectional area and its bandwidth [41]

[2]FERMI@Elettra in Italy [46], SACLA@SPring-8 in Japan [47], LCLS@SLAC in the USA [48], European XFEL@DESY in Germany [49], SwissFEL@PSI in Switzerland [50], PAL-XFEL@PAL in South Korea [51]

[3]SXFEL@SINAP in China [52], LCLS-2@SLAC in the USA [53]
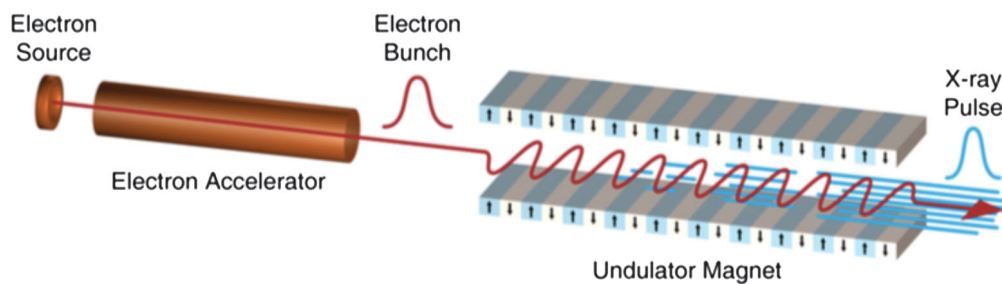
figure 3.2: *Main parts of a free-electron laser. Taken from [58].*

their propagation direction. The electromagnetic radiation is emitted in a small cone along the propagation direction of the electrons due to their relativistic velocity. The radiation also exhibits a partial coherence due to an internal feedback loop between electron bunch and its generated light field. Low divergence and coherence of the FEL radiation led to the term "laser", even though there is no stimulated emission involved.

The following section on FEL physics is compiled with information from reference [20]. The main parts of an FEL are depicted in figure 3.2. Starting from the left, electrons are generated in the "electron source" by illuminating a photocathode with a short-pulsed ultraviolet laser. The charge of each electron bunch has to be maximized and of low emittance, in order to achieve a large photon flux in the end. However, Coulomb forces between electrons set a limit to the bunch charge and the emittance. These space charge forces scale with $1/\gamma^2$, so its effect can be mitigated by accelerating the electrons to relativistic energies very fast [20, 54]. The "electron accelerator" is usually realized in form of a linear accelerator, which can provide the demanding beam parameters: "high peak current, small energy spread and small transverse emittance" [55]. There are many different types of accelerators, so we will exemplarily present the FLASH accelerator. It features seven TESLA-type [4] superconducting acceleration modules, reaching electron energies of up to 1.25 GeV. Each module comprises several radio frequency (RF) (1.3 GHz) cavities built up of solid niobium. The RF-synchronization of cavities ensures the voltage to be applied in the right period, so the electrons get accelerated from cavity to cavity. The cavities are helium-cooled to a temperature of 2 K at which niobium is superconducting. Normal-conducting cavities heat up strongly and can handle a RF duty cycle of just 0.01 %, while superconducting cavities can provide larger numbers. This difference in accelerator technology is reflected in the repetition rate of FEL pulses. FLASH exhibits a maximal repetition rate of 7500 Hz [57] while LCLS for example operates normal-conducting cavities delivering FEL pulses at a repetition rate of 120 Hz [48].

Following the acceleration, the highly relativistic electron bunches traverse the "un-

---

[4]The TESLA test facility developed superconducting accelerator technology originally for an electron-positron collider [56].

dulator magnet". The undulator consists of a periodic arrangement of permanent magnets forcing the electrons on a sinusoidal trajectory perpendicular to their propagation direction. The oscillatory motion implies an acceleration of charges and consequently synchrotron radiation is emitted. The fundamental wavelength λ_0 of this radiation is determined by several parameters of the electron bunch and the undulator:

$$\lambda_0 = \frac{\lambda_u}{2\gamma^2} \left(1 + \frac{K^2}{2} \right) \tag{3.1}$$

The period of undulator segments is denoted by λ_u, the Lorentz factor of the electrons by γ and K is the dimensionless undulator parameter. It is defined as:

$$K = \frac{eB_0\lambda_u}{2\pi m_e c}, \tag{3.2}$$

where B_0 is the peak magnetic field, e and m_e the electron charge and mass respectively, and c the speed of light. The simple relation in equation (3.1) already shows the main handles to change the photon wavelength: The electron energy represented by γ and the undulator period λ_u. While the former parameter is determined by the accelerator setup the latter is determined by the undulator setup. In most FEL facilities the photon wavelength is set by tuning the electron accelerator. FLASH2, however, features variable gap undulators which allows to quickly change the photon wavelength without changing the accelerator setup [57]. This facilitates photon energy scans during user operation, as presented in sections 4.3 and 4.4.

The difference between high-gain and low-gain FELs is that the former reaches intensity saturation within one single passage through the undulator. This is advantageous for radiation in the XUV or X-ray regime, where large absorption cross-sections make optical resonators impractical. On the contrary, low-gain FELs are often operated in the infrared (IR) or terahertz (THz) regime where optics for an optical resonator are available. In combination with an electron storage ring multiple passages through the undulator have to be performed to reach saturation. In the following and in the rest of this work we will focus on high-gain FELs in the XUV regime.

The process leading to high gain and partial coherence is called microbunching. The effect occurs within one electron bunch in the undulator, which finally generates one photon pulse. Initially each electron in the bunch wiggles with its own phase as illustrated in figure 3.3 on the left. As spontaneous radiation in the undulator travels along with the electron bunch, electrons are accelerated or decelerated depending on their phase relative to the radiation field. In this way electrons form so called microbunches along the propagation direction which are separated by the radiation wavelength. As the electrons arrange more regularly, the collective emission gets more intense and in turn the electrons experience a stronger force to arrange in the radiation field. This positive feedback loop is called self-amplified spontaneous
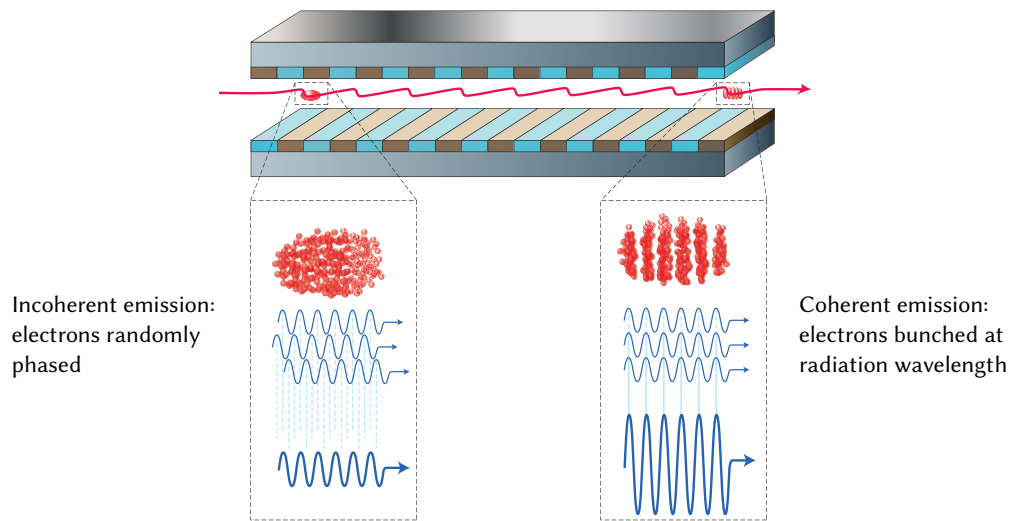
figure 3.3: *Microbunching and SASE in an undulator. Electrons within the electron bunch initially radiate at random phases. As the electrons interact with the light field they arrange (form microbunches) according to the radiation amplitude. The more the electrons arrange the more they radiate in phase enhancing the radiation field. The stronger field in turn leads to a stricter microbunching. This positive feedback loop is called SASE. Taken from [59].*

emission (SASE) [60, 61]. Besides the coherent properties obtained through microbunching, also the intensity scaling with the number of electrons is affected. If electrons are randomly distributed on the wavelength scale, they independently emit photons and the net output intensity scales with the number of electrons $N_e \propto I$. However, if the electrons are arranged according to their radiation wavelength and within a small fraction of it (cf. figure 3.3), the collectively emitted radiation scales $N_e^2 \propto I$ [61]. This scaling law is one reason why FELs can deliver radiation intensities which are many orders above synchrotrons. While FELs exhibit coherent emission, synchrotrons deliver purely incoherent radiation (cf. p.238 [20]).

Another specialty of FEL radiation is the shot-to-shot fluctuation between pulses. While other XUV radiation sources provide stable pulse characteristics from shot to shot, SASE-based FEL pulses differ in intensity, temporal structure and spectral distribution [63]. These fluctuations are owed to the stochastic character of the SASE process. For experiments which require a certain temporal and spectral resolution, the FEL pulse characteristics can be a limiting factor. Specific parameter combinations in the generation process can mitigate the spread of the crucial quantity, however fluctuations between pulses remain. Therefore it can be beneficial to analyze the pulses on a shot-to-shot basis. Figure 3.4 depicts (a) the temporal structure and (b) the spec-

figure 3.4: *Pulse analysis of single shots at FLASH. (a) Temporal structure of two long pulses obtained by THz streaking. (b) Three single shot spectra in color and an average spectrum in black. Taken and adapted from [62].*
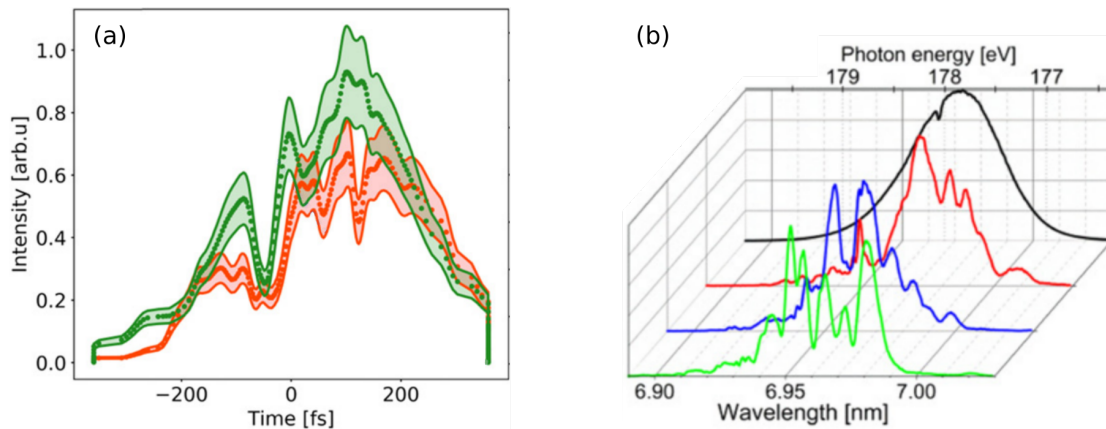
trum of individual pulses [62].

In this example the temporal structure of an XUV pulse is retrieved by THz streaking [64]. This technique exploits that photoelectrons of the ionizing XUV pulse carry temporal information of the pulse itself. If long wavelength THz radiation is superimposed during the ionization process, the photoelectron kinetic energy is modified according the THz vector potential at the moment of ionization. In this way, the temporal structure of the electron wave packet is mapped onto the photoelectron kinetic energy distribution. By measuring the kinetic energy parallel and perpendicular to the THz polarization, the temporal information on the XUV pulse can be retrieved and a pulse structure like the one depicted in figure 3.4 (a) can be obtained.

There are further techniques to investigate the temporal pulse structure on a single shot basis and additional ones for determining the average pulse duration. A comprehensive review of characterization methods for ultrashort XUV pulses is given in reference [65].

Spectral information about individual SASE pulses can be gained with an XUV spectrometer. See references [66, 67] for general information and [68, 69] for specific XUV spectrometer at FLASH. These spectrometers are based on diffraction from a grating with sufficiently small structures ($\approx$ μm). A pulse spectrum is obtained by a CCD camera recording diffracted light along the dispersive axis of the spectrometer. Exemplary spectra of individual pulses are depicted in figure 3.4 (b) in green, blue and red. An average spectrum of many pulses is plotted in black. This illustrates how the effective FEL bandwidth builds up in an experiment based on statistic.

Chapter 4

Publications

While the first two papers focus on the technical side and the capabilities of the REMI endstation, the three latter ones focus on physics and deal with laser-dressing effects in helium and electron correlations in argon.

4.1 Setup of the REMI endstation

The first half of this Phd project was dedicated to setting up a permanent REMI endstation at FLASH2. Its working principles and special features are described in the paper "Reaction microscope endstation at FLASH2" published in the Journal of synchrotron radiation.

While an idea of the setup and many basic beamline parts were already available from former beamtimes, the permanent setup opened up several possibilities to mount parts in a different way and to implement new sections. For example a main renewal was the in-line mirror chamber, replacing the back-reflecting mirror geometry. The new grazing-incidence mirrors exhibit a high reflectivity over a large XUV energy range. In this way, the mirrors can be kept in place during a photon wavelength scan, while the old setup was equipped with normal-incidence multilayer mirrors which had to be exchanged at different wavelengths. This characteristic is especially important at FLASH2 where variable gap undulators are implemented, which allow to quickly change the XUV photon wavelength (cf. Chapter 3).

Besides construction and commissioning of the endstation this paper explains the measuring scheme of the REMI. It covers the target preparation, the working principle of the detectors and the spectrometer and the data acquisition. Furthermore, it gives detailed information on the setup, like dimensions, geometries and vacuum conditions, which are not included in the experimental publications in sections 4.3 and 4.4.

Reaction microscope endstation at FLASH2[1]

Georg Schmid,[a]* Kirsten Schnorr,[a]‡ Sven Augustin,[a] Severin Meister,[a] Hannes Lindenblatt,[a] Florian Trost,[a] Yifan Liu,[a] Markus Braune,[b] Rolf Treusch,[b] Claus Dieter Schröter,[a] Thomas Pfeifer[a] and Robert Moshammer[a]*

[a]Max-Planck-Institut für Kernphysik, Saupfercheckweg 1, 69117 Heidelberg, Germany, and [b]Deutsches Elektronen-Synchrotron DESY, Notkestrasse 85, 22607 Hamburg, Germany. *Correspondence e-mail: georg.schmid@mpi-hd.mpg.de, robert.moshammer@mpi-hd.mpg.de

A reaction microscope dedicated to multi-particle coincidence spectroscopy on gas-phase samples is installed at beamline FL26 of the free-electron laser FLASH2 in Hamburg. The main goals of the instrument are to follow the dynamics of atoms, molecules and small clusters on their natural time-scale and to study non-linear light–matter interaction with such systems. To this end, the reaction microscope is combined with an in-line extreme-ultraviolet (XUV) split-delay and focusing optics, which allows time-resolved XUV-XUV pump–probe spectroscopy to be performed.

1. Introduction

A complete picture of the formation, internal rearrangement and the break-up of a molecule is only obtained if the evolution of the reaction is observed in a time-resolved manner (Zewail, 2000). As underlying processes like charge migration and energy redistribution within the molecule typically happen within a few to tens of femtoseconds, a spectroscopic technique that is fast enough to record the reaction is needed (Zewail, 1988). With the invention of short-wavelength free-electron lasers (FELs) (Ackermann *et al.*, 2007), the research area of atomic, molecular and optical (AMO) physics obtained a new experimental tool that provides femtosecond light pulses of extreme-ultraviolet (XUV) photons at unprecedented intensities (Feldhaus *et al.*, 2013; Yabashi *et al.*, 2013; Callegari *et al.*, 2016). The unique properties of XUV FEL pulses allow XUV pump–probe spectroscopy to be employed to study dynamical processes like isomerization (Jiang *et al.*, 2010*a*), nuclear wave-packet oscillations in molecules (Jiang *et al.*, 2010*b*; Magrakvelidze *et al.*, 2012), interatomic Coulombic decay (Schnorr *et al.*, 2013), electron rearrangement in dissociating molecules (Schnorr *et al.*, 2014), the expansion of clusters (Krikunova *et al.*, 2012; Sauppe *et al.*, 2018), non-equilibrium transient states in functional solids (Pontius *et al.*, 2018) and attosecond interferometry (Usenko *et al.*, 2017). Furthermore, short-wavelength FELs open up a new regime in non-linear light–matter interaction, *e.g.* multi-photon ionization can now be studied at XUV photon energies (Sorokin *et al.*, 2007*b*; Moshammer *et al.*, 2007; Richter *et al.*, 2009; Hikosaka *et al.*, 2010; Gerken *et al.*, 2014).

Besides an appropriate light source, a detection apparatus, which extracts the essential information on the process under investigation, is decisive.

Reaction microscopes (REMIs) are state-of-the-art coincidence momentum imaging spectrometers to resolve and
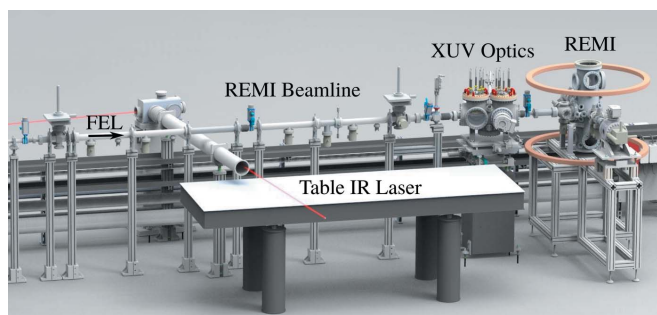
Figure 1
Overview of the REMI endstation at FL26. The FEL beam enters from the left. Shown are the REMI (*cf.* Section 2), the in-line XUV split-delay and focusing optics (*cf.* Section 3), the REMI beamline section (*cf.* Section 4) and an optical table for the IR laser (*cf.* Section 6). The figure is taken from Schmid (2018).

study fundamental reactions in atoms or molecules, triggered upon collisions with ions, the impact of electrons or absorption of photons (Ullrich *et al.*, 2003).

Taking advantage of the synergy arising from the combination of a REMI and a high-repetition-rate XUV FEL (Rudenko *et al.*, 2010; Moshammer & Schnorr, 2014), a dedicated user endstation is installed at beamline FL26 of the free-electron laser FLASH2 (Plönjes *et al.*, 2016; Faatz *et al.*, 2016). Fig. 1 shows the layout of the endstation. In this paper, the main components are introduced and commissioning results are discussed.

2. Reaction microscope

Reaction microscopes are multi-particle coincidence spectrometers for AMO physics, which allow measuring the initial energies and emission angles of the charged products, *i.e.* ions and electrons, of fundamental atomic and molecular reactions in the gas phase (Moshammer *et al.*, 1996; Dörner *et al.*, 2000).

To this end, the charged reaction fragments, *i.e.* atomic or molecular ions and electrons, are accelerated onto large-area time- and position-sensitive detectors. By measuring the time-of-flight (TOF) and the impact position of the particles on the detectors, the initial three-dimensional momentum vectors can be reconstructed. While the ions carry information about the nuclear dynamics during a reaction, the ejected electrons are sensitive to the electronic structure of the system under investigation. In the ideal case, electrons and ions are measured in coincidence and, by applying momentum conservation, fragments emerging from a single atom or molecule can be selected. This enables so-called *kinematically complete* experiments to be performed (Kurka *et al.*, 2009).

The REMI installed at FLASH2 is schematically shown in Fig. 2. The FEL beam (purple) is focused into a supersonic gas jet (*cf.* Section 2.1), which contains the target atoms, molecules or clusters (green spheres). Created ions (red trajectory) and electrons (blue trajectory) are separated by their different charges and guided onto opposing detectors (*cf.* Section 2.3) by the electric field of the spectrometer (*cf.* Section 2.2). The magnetic field generated by a pair of Helmholtz coils forces
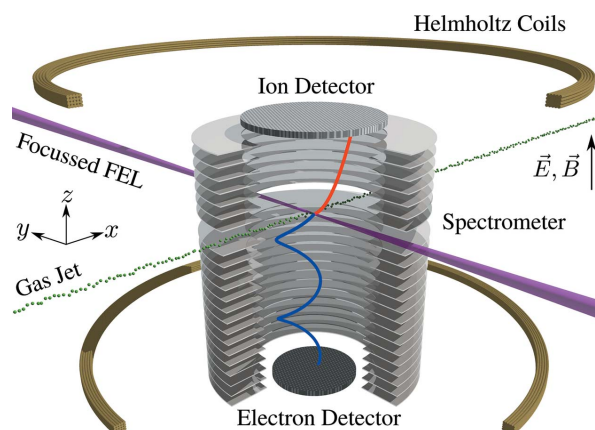
Figure 2
Schematic drawing of the REMI. Shown are the main components, *i.e.* spectrometer, ion detector, electron detector and a pair of Helmholtz coils. The FEL beam (purple) is focused into a supersonic gas jet (green spheres). Created ions (red trajectory) and electrons (blue trajectory) are guided by a combination of an electric (E) and a magnetic field (B) onto their respective detector. The coordinate system (x, y, z) used within this section is also shown. The figure is adapted from Schmid (2018).

the electrons in cyclotron orbits on their way to their detector. The combination of a homogeneous electric and magnetic field ensures a solid-angle acceptance of 4π for all ions and electrons of interest. In the following, the key components of the REMI are introduced.

2.1. Target injection

The target preparation is based on supersonic expansion of gas-phase samples. For this, gas is expanded through a nozzle from a high-pressure reservoir into vacuum and a supersonic jet is formed. In doing so, the undirected thermal energy of the gas particles is transformed into directed kinetic energy, which results in a decrease of internal temperature. The achieved temperature depends on several parameters, in particular on the specific gas, the nozzle diameter, the backing pressure and the temperature of the gas before the expansion (Scoles, 1988).

Three different nozzle assemblies are available at the REMI endstation. Firstly, a cooled nozzle allows to pre-cool the gas before the expansion. Cooling down to cryogenic temperatures is achieved by using a closed-cycle helium refrigerator cold-head, and very low jet temperatures are reached (for example ~ 0.5 K for a helium jet). This results in very low momentum uncertainty of the target atoms or molecules. Hence, this nozzle assembly is suited for experiments that ask for a high-momentum resolution for the recoil-ions (Kurka *et al.*, 2010). Secondly, a heatable nozzle can be installed to inject liquid and solid samples with low vapor pressure (Schnorr *et al.*, 2014). It is based on sublimating the sample in a heatable reservoir outside of the vacuum. The molecules are then carried to the nozzle by a seeding gas or the vapor pressure. An increasing temperature gradient from the reservoir to the nozzle circumvents re-sublimation and, thus, clogging of the system. The heatable nozzle can operate up to temperatures of 200°C. Thirdly, a nozzle assembly where the reservoir for

liquid samples is integrated into the vacuum system is available. The design is based on evaporating the liquid as close as possible to the nozzle to prevent clogging by condensation. The system can be operated with and without a seeding gas. Using this nozzle assembly, the generation of water and water–rare-gas dimers has been accomplished (Meister, 2016).

The experimental implementation of the jet system is shown in Fig. 3. It features six vacuum stages that are differentially pumped. Hence, despite backing pressures of up to 70 bar in the nozzle, ultra-high-vacuum (UHV) conditions are preserved in the REMI interaction chamber (*cf.* Section 2.4). In order to form a supersonic jet, the gas expands from a high-pressure reservoir (0) through the nozzle (typical diameters 5−50 μm) into the vacuum of the first jet stage (1). A sharp-edged conical skimmer made of pure copper (inner diameter: 180 μm) is coaxially opposing the nozzle to peel off gas particles from the so-called *zone of silence* (*cf.* inset Fig. 3), *i.e.* a region where gas particles have supersonic speeds and low internal temperatures. A subsequent second skimmer (2) (inner diameter: 400 μm) geometrically selects only gas particles with a small momentum spread in the direction perpendicular to the jet-propagation direction (*cf.* inset Fig. 3). The nozzle assemblies introduced above are mounted on a triaxial *xyz*-manipulator, which allows adjustment of the distance between the nozzle and the first skimmer in the *x*-direction as well as the position in the perpendicular (*y, z*)-plane. The coordinate system is shown in Fig. 3. The subsequent stages (3, 4, 5, 6) are separated by apertures of 2 mm inner diameter. Three pairs of slits (two vertical, one horizontal) in the stages 4, 5 and 6 allow tuning of the jet divergence in the (*y, z*)-plane and thus the target extension along the FEL beam direction. Finally, a spatially well confined (diameter ≤ 2 mm), dilute (≤10^{10} particles cm^{-3}) and cold (typically <20 K) beam of atoms, molecules or clusters enters the REMI spectrometer (*cf.* Section 2.2). The portion of the jet which is not ionized is collected in the jet dump to avoid an increase of gas pressure in the REMI interaction chamber. The REMI interaction chamber, jet dump stage (i) and jet dump stage (ii) are separated by tubes of 4 mm inner diameter for differential pumping.

2.2. Spectrometer

The REMI spectrometer is schematically depicted in Fig. 2. It consists of ring-electrodes to create a homogeneous electric field at the interaction point and between the two detectors of the REMI. The rings are separated by a distance of 10 mm and are made of annealed stainless steel. They have an inner diameter of 120 mm, an outer diameter of 200 mm and are
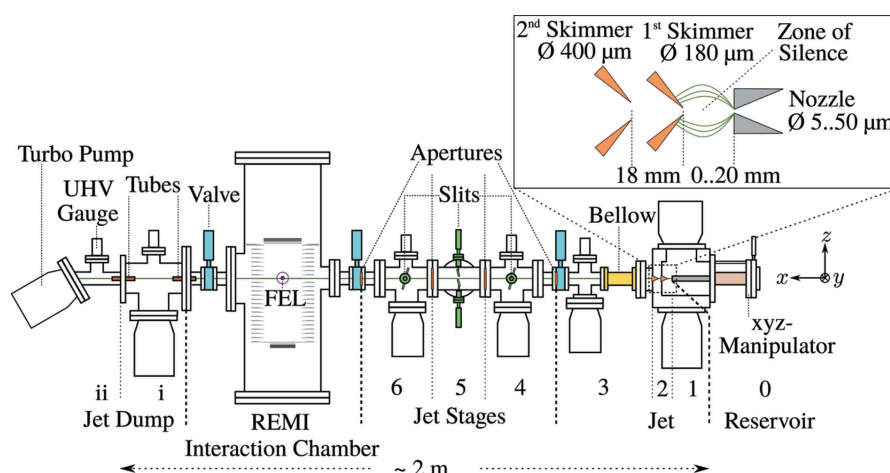
Figure 3
Schematic lateral cut through the REMI along the axis defined by the jet propagation (coming from the right side). From right to left: jet chamber (1, 2, 3), jet stages (4, 5, 6), REMI interaction chamber and jet dump (i, ii). The sections are separated by gate valves (light-blue). Details on the sections are given in the main text. Inset on the top right: detailed view of the first and second jet stage. The figure is adapted from Schmid (2018).

1 mm thick. The individual rings are electrically connected by a cascade of 100 kΩ resistors and a fixed voltage can be applied across the spectrometer. The inner boundaries of the rings are sharply edged towards the center to generate well defined equipotential planes. This ensures a homogeneous electric field over the entire inner volume of the spectrometer. Fine-meshed stainless steel grids (wire diameter: 30 μm; mesh size: 224 μm; transmittance: ∼80%) at both ends of the spectrometer ensure a defined termination of the electric field.

The spectrometer has a total length of 275 mm. In order to optimize the acceptance for ions with high kinetic energies, which emerge, for example, from Coulomb explosion of molecules (Schnorr *et al.*, 2014), the ion side of the spectrometer is kept short (94.5 mm). The electron side is about a factor of two longer. An ion (red trajectory in Fig. 2) of mass m and charge q that is created at the interaction point (center of the REMI) with zero initial momentum reaches the detector after the time-of-flight

$$\text{TOF} = d\left(\frac{2m}{qU}\right)^{1/2} \propto \left(\frac{m}{q}\right)^{1/2}. \qquad (1)$$

Here, U is the applied voltage and d is the distance between the interaction point and the detector. The proportionality of the TOF to the square root of the mass-to-charge ratio [*cf.* equation (1)] allows different ion species to be distinguished. The spectrometer does not have a field-free drift region or, in other words, the constant electric field is active over the whole length of the spectrometer, *i.e.* from the ion to the electron detector. A drift region, for, for example, time focusing (Wiley & McLaren, 1955), is not implemented since the starting point of the ions' and electrons' TOF is well defined by the small FEL focal spot diameter of <10 μm (*cf.* Section 5.1). Furthermore, a drift region would geometrically reduce the acceptance of the ion detector for ions with high kinetic energies.

Electrons with the same momenta as the recoiling ions move with much higher velocities compared with the heavier ions ($m_{proton}/m_e \simeq 1836$). With high probability they would leave the spectrometer transversally and miss the electron detector. To avoid this, a magnetic field is applied parallel to the electric field. In the magnetic field electrons fly in cyclotron orbits to their detector (blue trajectory in Fig. 2). The magnetic field (of the order of $B \simeq 10$ Gauss) is generated by a pair of Helmholtz coils (*cf.* Fig. 2). As the cyclotron frequency is given by $\omega = qB/m$, the trajectories of the heavier ions are not measurably changed by the magnetic field.

As ions from Coulomb explosions can have high kinetic energies, high electric fields of up to 100 V cm^{-1} must be applied to the spectrometer to achieve full angular acceptance for these ions. The actual acceptance depends on several parameters, in particular charge state and mass of the ions, as well as the velocity offset that the particles already have as they are contained in a propagating gas jet (*cf.* Section 2.1) before interacting with the FEL. Taking typical values for these parameters, the spectrometer has at least a full angular acceptance for ions with kinetic energies of up to 40 eV. In order to measure electrons and ions in coincidence with sufficient resolution, lower electric fields (≤ 10 V cm^{-1}) need to be applied. In this operation mode, the spectrometer typically has a full angular acceptance for electrons with maximum kinetic energies of about 40 eV.

2.3. Detectors

Large-area micro-channel plate (MCP) detectors are used to measure the TOF and the impact position of ions and electrons. Each detector is equipped with a stack of MCPs (Wiza, 1979), which generates the signals and allows the TOF information to be extracted. A delay-line anode (Lampton *et al.*, 1987) located behind the MCPs is used to obtain the position information. Fig. 4 gives an overview of the detector assembly and its working principle (Jagutzki *et al.*, 2002*b*).

An impinging primary particle (ion or electron) initiates an electron avalanche in a channel of the MCPs. This leads to a drop in the voltage over the MCPs, which gives a signal [*cf.* Fig. 4(*b*)]. The TOF is measured relative to the FEL trigger: TOF = $t_{MCP} - t_{trigger}$. The signal of t_{MCP} is read out capacitively. After the MCPs, the electron cloud is attracted by the delay-line anode. The induced signal propagates to both ends of the delay-line wire [*cf.* Fig. 4(*c*)]. One of the position coordinates is given by $x = v_\perp/2(t_2 - t_1)$. Here, $t_1 = t_1^* - t_{MCP}$ and $t_2 = t_2^* - t_{MCP}$ are the arrival times of the signal at the ends of the wire relative to the MCP timing signal t_{MCP}. The effective propagation velocity of the signal along the wire is denoted by $v_\perp$.

The ion detector is equipped with a stack of two 120 mm-diameter MCPs in a chevron arrangement [*cf.* Fig. 4(*b*)] and a delay-line anode. Specifically, it is a so-called *quadanode* as it consists of two perpendicularly oriented quadratic wire layers [*cf.* Fig. 4(*a*)]. The electron detector features three MCPs of 80 mm diameter in a *Z*-arrangement and a delay-line anode, which is made of three wire layers that are rotated by 60°
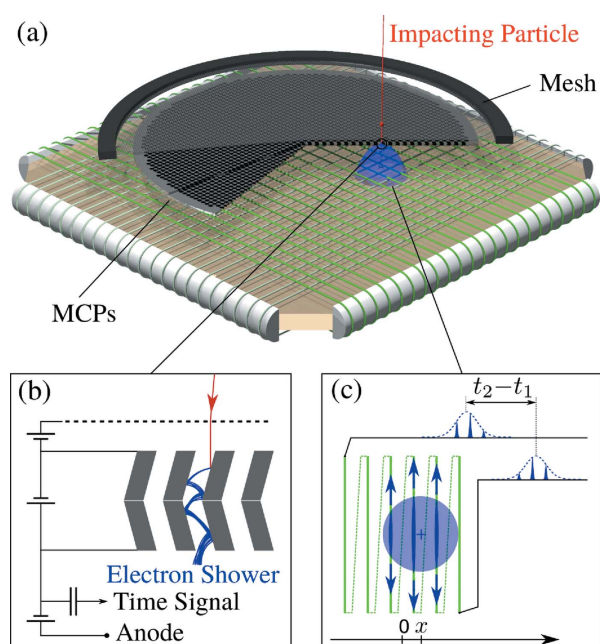
Figure 4
(*a*) CAD-like drawing showing the working principle of the time- and position-sensitive detector. (*b*) Amplification by the MCPs and out-coupling of the TOF signal. (*c*) Position detection scheme using a delay-line anode. The figure is adapted from Fechner (2014). [Reprinted by permission from Springer.]

relative to each other. This so-called *hexanode* delay-line anode improves the multi-particle hit detection efficiency by introducing redundancy (Jagutzki *et al.*, 2002*a*).

2.4. Vacuum conditions

All ions and electrons, which are created inside the volume of the spectrometer (*cf.* Section 2.2), are accelerated towards the detectors (*cf.* Section 2.3) and are registered as events. The detectors, however, cannot discriminate between particles from the target and those from residual gas. At XUV photon energies above ~ 15 eV, a single photon can ionize a residual gas molecule (*e.g.* H_2, H_2O, N_2, O_2). The XUV photoabsorption cross sections of residual-gas molecules and those of target atoms, molecules or clusters are of the same order of magnitude (Yeh & Lindau, 1985; Gallagher *et al.*, 1988). In combination with FEL pulse energies of the order of some tens of μJ, this causes a non-negligible number of background events along the FEL beam inside the REMI spectrometer.

To minimize the number of background events, vacuum conditions of $\leq 10^{-11}$ mbar need to be reached in the REMI interaction chamber. The generation of such high vacua in a large vessel like the REMI interaction chamber (CF DN250 tube, length ~ 80 cm) is difficult to achieve by turbomolecular pumps alone. Thus, the complete inner surface of the interaction chamber is coated with a thin film (~ 1.5 μm) of non-evaporable getter (NEG) material. NEG is a special alloy, *e.g.* Ti–Zr–V, which has a large surface area. Thereby, the probability of molecules to stick to the chamber walls is increased. At extreme vacua ($\sim 10^{-12}$ mbar), the thermal

outgassing of H_2 from the steel walls of the chamber is the major source of residual gas (Benvenuti *et al.*, 1999). However, turbomolecular pumps are not well suited to pump H_2 with typical H_2 pumping speeds of only several hundreds $l\,s^{-1}$ (Jousten, 2010). In contrast, the H_2 pumping speed of the NEG coating of the REMI interaction chamber is estimated to be $\sim 3600\,l\,s^{-1}$ (Benvenuti *et al.*, 1999). However, after each venting, the coating needs to be re-activated by heating the chamber to temperatures of $\geq 200^{\circ}C$ for at least 24 h (Benvenuti *et al.*, 1999).

2.5. Data acquisition

FLASH features a special pulse repetition rate pattern. At 10 Hz repetition rate, pulse trains (maximum train length 800 µs) with an intra-train pulse separation between 1 and 25 µs are provided (Faatz *et al.*, 2016). This *burst-mode* pulse pattern requires a data acquisition system, which is capable of processing the incoming signals of a REMI.

Four Acqiris DC282 digitizer cards, each with four channels, are used to record the voltage traces of each and every detector signal over a time range up to 800 µs. The highest sampling rate of the digitizer cards is 2 GHz (0.5 ns between two samples) and the maximum voltage range for each channel is ±5 V. The voltage trace for each channel recorded during the entire pulse train is stored internally on the digitizer cards. Then, the 10 Hz FEL trigger initiates the readout of the channels after the end of each pulse train. Zero suppression, peak finding on the signals and sorting of the data is done by computer algorithms in the online as well as the offline analysis (Schnorr, 2014). The analysis code *GENERiC* (*General Analysis Code for Reaction Microscopes*) is embedded in the Go4 (GSI Object Oriented On-line Off-line system) analysis environment (GSI, 2018) based on CERN's *ROOT* (CERN, 2018).

3. In-line XUV split-delay and focusing optics

The basic concept of the XUV optics is to split and focus the FEL beam before it enters the REMI.

The underlying geometry and working principle is depicted in Fig. 5. The FEL beam approaches from the left and first hits the split-mirror under a grazing angle of $\theta = 8^{\circ}$. The split-mirror is a plane mirror, which is horizontally cut into two coextensive pieces. The upper mirror is movable and can be translated back and forth along the mirror normal axis. Thus, a path difference can be introduced between the upper beam (green) and the lower beam (blue). The incoming FEL pulse is split into two and the path difference translates into a temporal delay t_d between the pump (blue) and the probe (green) pulse. After the splitting, the two beams are focused by an ellipsoidal mirror into the supersonic jet of the REMI. The grazing-incidence geometry and a carbon coating of the split and the ellipsoidal mirror guarantee high reflectivity over a broad photon energy range from 30 to 180 eV (*cf.* Fig. 7). This allows making use of the wavelength tunability of the FLASH2 variable-gap undulators (Faatz *et al.*, 2016). The use
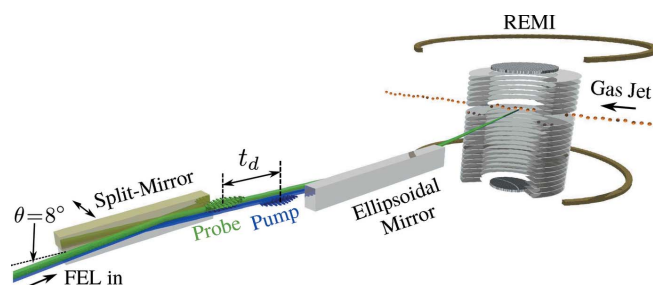
Figure 5
Design of the in-line XUV split-delay and focusing optics. Shown are the FEL beam path, the split-mirror, the ellipsoidal mirror and the REMI with gas jet. Also depicted is the generation of a pump (blue) and a probe (green) pulse by translating the upper split-mirror along the mirror normal axis. Pump and probe pulses are temporally delayed by t_d. The figure is adapted from Schmid (2018).

of a single ellipsoidal mirror instead of a KB focusing system, implemented at other beamlines at FLASH (Erk *et al.*, 2018), reduces the number of optical components in the beam path and thus increases the overall transmission of the beamline.

3.1. Split-mirror assembly

The split-mirror is the centerpiece of the XUV pump–probe optics. It consists of two plane mirrors with clear apertures of 120 mm × 10.5 mm each. In order to achieve femtosecond pump–probe resolution and to keep spatial overlap of both beams in the focus for all delay values, the upper mirror is movable by a kinematics based on piezo positioners. The split-mirror assembly is shown in Fig. 6.

The kinematics is custom-made by SmarAct GmbH. It allows the position of the upper mirror to be manipulated in three dimensions: linear motion along the mirror normal axis (*travel*), rotation along the vertical (*tilt*) and horizontal (*tip*) axis. The coordinate system is defined in Fig. 6. The rotational
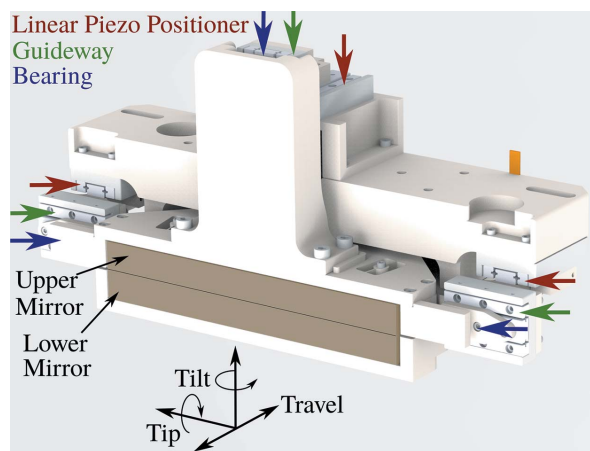
Figure 6
Split-mirror assembly. The upper mirror is movable in the three dimensions *travel*, *tilt* and *tip* by a piezo-driven kinematics. Positioners, guideways and bearings are marked by red, green and blue arrows, respectively. Details on the assembly are given in the main text. The figure is adapted from Schmid (2018).

axes are set along the mirror surface. The maximum travel range of $h = \pm 3$ mm along the mirror normal translates into a maximum delay range of $t_d = \pm 2.7$ ps. Rotations up to a few degrees are possible for the tilt axis. The maximum tip rotation of ± 20 mrad is limited by the minimal allowed gap distance of 100 µm between the two mirrors. The gap is intended to be as small as possible in order to minimize photon losses. The distance between the mirrors can be manually adjusted by three spring-mounted fine-thread screws.

The kinematics has three legs, each consisting of a linear piezo positioner, a linear guideway and a bearing (*cf.* Fig. 6). Due to the guideways and the bearings, linear motions of the piezo positioners translate into a linear motion along the *travel* direction and rotations around the *tip* or *tilt* axis. The positioners are SmarAct SLC-1730 nanometer-precision linear piezo positioners, which are based on the stick–slip principle (Hunstig, 2017). They are operated in closed-looped (encoder feedback) and are controlled by the SmarAct MCS controller module with the Advanced Sensor Calibration (ASC) option.

Based on the position resolution of the encoders (4 nm), the upper limit of the temporal resolution is estimated to be $\Delta t_d \simeq 4$ as. Tests employing the interference pattern of an optical laser (wavelength 658 nm) confirm this limit. Tests on the pointing stability, *i.e.* the ability to maintain spatial overlap of both beams in the focus for all delays, are presented in Section 5.2.

3.2. Ellipsoidal mirror

After the split-mirror, the beam is focused by an ellipsoidal mirror (*cf.* Fig. 5). It is designed for a source distance of 85 m, a focal length of 1 m and an incidence angle of $\theta = 8°$. The machining of the mono-crystalline silicon substrate was performed by Carl Zeiss SMT GmbH. The clear aperture of the mirror is 180 mm × 20 mm. The quality inspection of the manufacturer specifies the slope errors to be 0.84 arcsec (r.m.s.) tangential and 1.2 arcsec (r.m.s.) sagittal. The surface roughness is measured to be 0.19–0.24 nm. For high transmission over a broad XUV photon energy range, the mirror is coated with a 30 nm thin layer of carbon by optiXfab GmbH. The layer thickness has a relative error of ±5% and the lateral homogeneity is >97%. At $\theta = 8°$, the mirror has a reflectivity of >50% up to photon energies of 180 eV (*cf.* Fig. 7).

The split-mirrors are also carbon-coated in the same way and the mono-crystalline silicon substrates are of the same quality as the ellipsoidal mirror.

3.3. Hexapod kinematics

To obtain best focusing conditions and high transmission, the split and the ellipsoidal mirror need to be individually positioned in all three rotational and translational directions with microradian- and micrometre-precision. In order to achieve these accuracies, hexapod kinematics as shown in Fig. 8 are used.

The split-mirror assembly and the ellipsoidal mirror have their individual kinematics, which are mounted on two separate flanges of one vacuum chamber. A decoupled adjustment
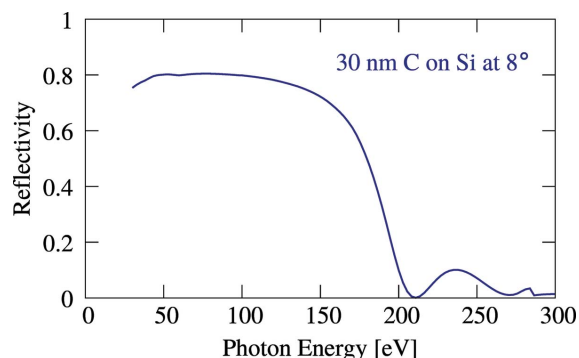
Figure 7
Calculated reflectivity at a grazing angle of $\theta = 8°$ of a carbon-coated mirror (30 nm layer thickness, mono-crystalline silicon substrate). Data taken from Henke *et al.* (1993).

of both mirrors is essential for beam alignment and also indispensable to achieve optimal focusing conditions as well as to compensate manufacturing tolerances of the mirror chamber. The mounting on two separate supporting flanges also enables an independent removal of both mirror assemblies.

The general design of the kinematics has been developed by the group around T. Noll and Th. Zeschke from the Helmholtz Zentrum Berlin (HZB)/BESSYII (Noll *et al.*, 2009). The design has been adapted by FMB Berlin GmbH, who also manufactured the kinematics and the surrounding vacuum chamber.

The hexapod has six legs, each consisting of two steel rope joints, a connection strut, a leaf spring, a bellow and a motorized actuator (*cf.* Fig. 8). By linearly pulling or pushing of the actuators, the legs react dynamically and the attached platform moves. The design uses stable steel rope joints instead of conventional bearings to increase the overall stiffness. The flexible copper–beryllium leaf springs prevent a lateral displacement of the upper joint in stressed positions of the joints. In contrast to usual hexapods, the driving motors are not directly part of the moving assembly. This decreases the total mass and potentially outgassing electrical parts stay
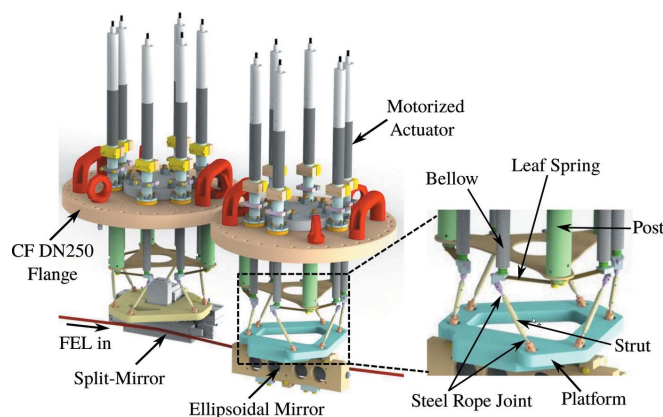
Figure 8
CAD-like drawing of the two hexapod kinematics holding the split-mirror assembly and the ellipsoidal mirror, respectively. Labels mark the main parts. The figure is adapted from Schmid (2018).

outside the vacuum. Bellows separate the actuators from the vacuum. After baking of the vacuum chamber at 120°C for about 24 h, a pressure of 10^{-10} mbar was reached in the mirror chamber.

The hexapods are designed for rotations of $R_x, R_y, R_z = \pm 0.5°$ and translations of $T_x, T_y = \pm 3$ mm laterally and $T_z = \pm 5$ mm vertically. The vertical travel of $T_z = \pm 5$ mm for the split-mirror assembly allows the complete FEL beam (10 mm diameter) to be put onto one of the split-mirrors. This option is used for experiments, which do not employ an XUV–XUV pump–probe scheme, *e.g.* XUV–IR pump–probe experiments (*cf.* Section 6). Tests have shown that the resolution for all translations is $\Delta T_{x,y,z} \simeq 0.1$ μm and for all rotations $\Delta R_{x,y,z} \simeq 1$ μrad. The movement of the hexapods is controlled by a *LabVIEW* program.[2]

4. Beamline

4.1. Accelerator tunnel section and experimental hall

An overview of the FEL beam transport and diagnostics at FLASH2 has been given by Plönjes *et al.* (2016). In the tunnel section, beam position monitors and a set of apertures followed by Ce:YAG fluorescence screens are used to monitor and to shape the FEL beam. The apertures are also utilized to adjust the transmitted pulse energy. The absolute pulse energy can be measured by a gas-monitor detector (GMD) (Tiedtke *et al.*, 2009) or a micro-channel plate (MCP) tool (Bittner *et al.*, 2007). A non-invasive online photoionization spectrometer (OPIS) measures the average photon energy (Braune *et al.*, 2016). The accelerator tunnel section ends with a gas-filled attenuator, which allows the transmitted energy per pulse to be continuously adjusted.

The photon-diagnostics section in the experimental hall is equipped again with a second GMD, a further set of apertures and Ce:YAG fluorescence screens. Transmission filters are mounted to regulate the FEL intensity and to suppress harmonics. The filters of different materials and thicknesses (typically a few 100 nm) are mounted on two consecutive motorized wheels. Depending on the photon energy and intensity, different filters and combinations can be selected.

4.2. REMI beamline

In order to protect the vacuum conditions in the REMI interaction chamber ($\leq 10^{-11}$ mbar) from the vacuum in the FLASH beamline (typically $> 10^{-9}$ mbar) and to reduce stray
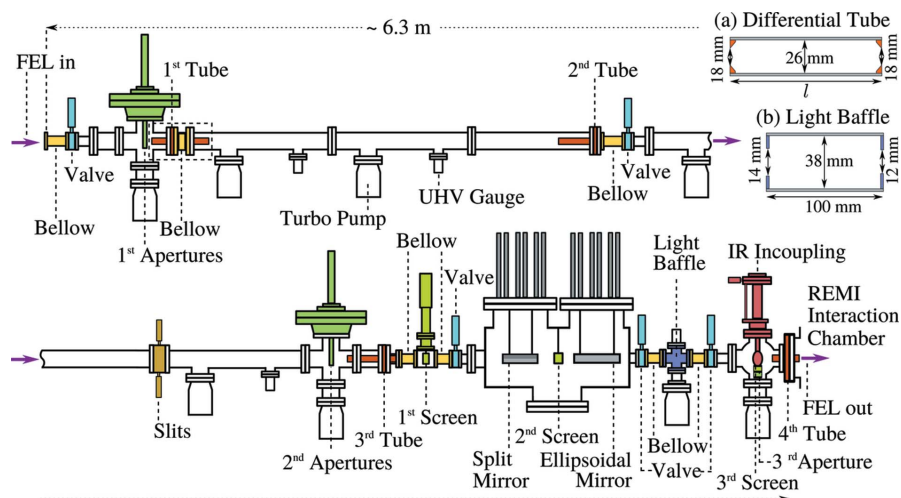
Figure 9
Schematic lateral cut through the beamline in front of the REMI. The FEL beam enters from the left. Shown are differential pumping tubes (orange), bellows (yellow), apertures (dark-green), valves (light-blue), slits (light-brown), screens (light-green) and a light baffle (blue). The XUV split-delay and focusing optics (*cf.* Section 3) is also illustrated. The IR incoupling (red) is discussed in Section 6. The inset (*a*) shows the dimensions of the differential pumping tubes (colored orange in the main figure). At the entrance and the exit, the tubes are configured with sharply chamfered copper apertures (orange). The length *l* varies between 185 and 287 mm depending on the position of the tube in the beamline. (*b*) Dimensions of the light baffle (colored blue in the main figure). At the entrance and the exit, two apertures made of roughened 625 μm thin silicon wafers (blue) are inserted. The figure is modified after Schmid (2018).

light, the beamline in front of the REMI is separated into five differentially pumped sections and has a total length of ∼6.3 m (*cf.* Fig. 9).

The sections are connected via small-diameter tubes (colored orange in Fig. 9) which leads to low gas conductance between the sections. The tubes are configured to reduce stray light. At the entrance and exit, chamfered copper apertures are clamped into the tubes. The chamfer is manufactured as sharp as possible in order to minimize the area where photons might scatter. The apertures have an inner diameter of 18 mm, while the tubes (lengths between 185 and 287 mm) themselves have an inner diameter of 26 mm [*cf.* Fig. 9(*a*)]. This configuration acts as a light baffle for photons that are scattered in off-axis directions.

After the mirror chamber, a further light baffle (colored blue in Fig. 9) is installed to prevent stray light in the direct vicinity of the REMI detectors. This light baffle consists of two apertures with respective inner diameters of 14 mm and 12 mm [*cf.* Fig. 9(*b*)]. They are made of roughened 625 μm thin silicon wafers (blue) and serve the same purpose as the copper apertures of the differential tubes, *i.e.* to remove undirected scattered photons.

At two distinct positions along the beamline, circular apertures on a moveable rail (aperture diameters from 4 to 10 mm in steps of 1 mm) are integrated (colored dark-green in Fig. 9). The apertures are chamfered with the sharp edge pointing towards the incoming beam again for reasons of stray light reduction. Additionally, the apertures' surfaces facing the beam are coated with a fluorescent ZnS powder, which facil-

itates the beam alignment. A third aperture (diameter 10 mm) which is part of the IR incoupling unit (colored red in Fig. 9, discussed in Section 6) is located directly in front of the REMI interaction chamber.

In total, three fluorescence screens (colored light-green in Fig. 9) can be inserted to monitor the position and the shape of the FEL beam. The first screen (20 mm × 20 mm) is located in front of the mirror chamber. A second screen (25 mm × 25 mm) can be placed between the split and the ellipsoidal mirror to monitor the shape of the split beam and the illumination uniformity on the split-mirrors. A third screen (20 mm × 20 mm) is located in front of the REMI. Each screen consists of a stack of a Ce:YAG plate (200 μm thick) and a roughened silicon plate (625 μm thick). The Ce:YAG plate faces the FEL beam and fluoresces upon illumination with XUV photons. The roughened silicon plate, which is mounted behind the Ce:YAG plate, is used to visualize the optical alignment laser (wavelength 658 nm).

A pair of horizontal slits (colored light-brown in Fig. 9) can be used to block the upper or the lower part of the incoming FEL beam. This option is useful for adjusting the downstream XUV split-delay and focusing optics (cf. Section 3), e.g. to check how the pulse energy in the pump and the probe pulse is distributed.

4.3. REMI interaction chamber and photon dump

In order to spatially overlap the foci at the nominal interaction point with the gas jet (cf. Section 3), a fluorescence screen can be moved into the center of the REMI spectrometer. This target screen is 10 mm × 10 mm in size and coated with a thin film of Ce:YAG powder. A CCD camera (Basler acA1300-30gc with Sony ICX445 CCD sensor, 1.3 MP, pixel size 3.75 μm × 3.75 μm, sensor size 4.9 mm × 3.6 mm) in combination with an optical magnification system (Navitar 1-60135D, overall magnification 2.4) images the fluorescence of the foci from outside. The vacuum of the REMI interaction chamber is separated from the following photon dump by two differentially pumped sections. The corresponding differential tubes are colored orange in Fig. 10.

The beam profile and position after the REMI can be monitored by a Ce:YAG fluorescence screen (20 mm × 20 mm) (colored light-green in Fig. 10). The fluorescence screen is followed by a 1 m-long CF DN40 tube. Two bellows (colored yellow in Fig. 10) at each end allow to slightly tilt or bank out the entire tube. This option is applied to minimize photon back-scattering from the FEL dump. The photon dump is terminated by a copper plate, which is electrically connected (colored brown in Fig. 10). The voltage signals induced by impinging FEL pulses serve as a reference for the pulse arrival times and the pulse energies. From the first valve (colored light-blue in Fig. 10) onwards, the entire photon
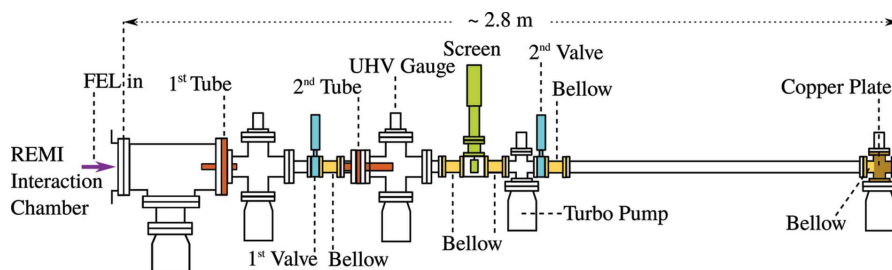
Figure 10
Schematic lateral cut through the photon dump. The FEL beam enters from the left. Shown are differential pumping tubes (orange), valves (light-blue), bellows (yellow), a retractable screen (light-green) and a copper plate (brown). The figure is taken from Schmid (2018).

dump is mounted on a single supporting frame. This way, it can be quickly removed for setting up a subsequent optional experiment behind the REMI. The first valve is located 827 mm behind the center of the REMI. Taking the maximum diameter of 10 mm of the incoming FEL beam before focusing, the diverging FEL beam has a maximum diameter of ~8.3 mm at this position.

5. Commissioning results

5.1. Focal spot size

A wavefront sensor (WFS) (Keitel *et al.*, 2016) has been used to analyze the optical properties of the new XUV split-delay and focusing optics (cf. Section 3). For the measurements at $\hbar\omega = 56$ eV a Compact Hartmann Sensor (Keitel *et al.*, 2016) was used. The intensity profile of the smallest achieved focus is shown in Fig. 11.

A diameter of $d \simeq 3$ μm (FWHM) was obtained. Assuming a pulse energy of $E_{pulse} = 10$ μJ and a typical pulse duration of $T = 50$ fs, this corresponds to an intensity of $I \simeq 10^{15}$ W cm^{-2}.
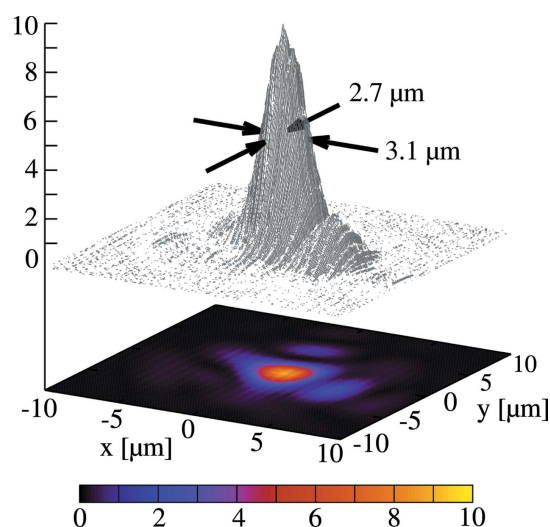
Figure 11
Intensity profile obtained by wavefront reconstruction. Shown is the smallest achieved focus. The arrows mark the FWHM in the *x*- and *y*-direction.
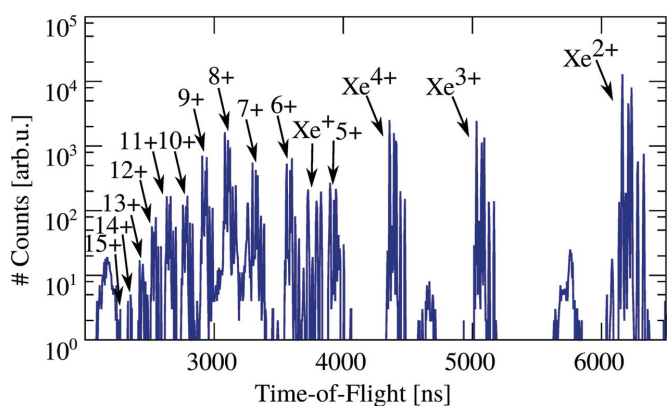
Figure 12
TOF spectrum of xenon ions recorded at $\hbar\omega = 100$ eV. For this measurement, the entire FEL beam with $E_{pulse} \simeq 20$ µJ pulse energy is put onto the lower mirror of the split-mirrors. $Xe^{(1-15)+}$ ions are marked by arrows. As TOF $\propto (m/q)^{1/2}$ [cf. equation (1)], Xe^+ ions have the longest TOFs of all Xe ions considered, which is longer than the time interval $\Delta t_{FEL} = 5000$ ns between two consecutive FEL pulses. Therefore, Xe^+ ions appear out of order at TOF(Xe^+) − $\Delta t_{FEL} = 3750$ ns. The figure is taken from Schmid (2018).

The charge states reached in multi-photon ionization of xenon are a further benchmark of the achieved intensity and thus the focus size. Fig. 12 shows the TOF spectrum of xenon ions recorded at a photon energy of $\hbar\omega = 100$ eV and a pulse energy of $E_{pulse} \simeq 20$ µJ.

For this measurement, the entire FEL beam was placed onto the lower split-mirror to avoid losses due to the gap between the two mirrors. For each charge state several close-lying TOF peaks appear reflecting the naturally abundant isotopes of xenon. The charge states are marked by arrows and Xe^{15+} is the highest charge state observed. Richter *et al.* (2009) measured Xe^{14+} at $I = 1.7 \times 10^{15}$ W cm^{-2} and Sorokin *et al.* (2007*a*) reported Xe^{15+} at $I = 2 \times 10^{15}$ W cm^{-2}. Taking these values, the intensity reached with the present setup is estimated to be 1×10^{15} to 2×10^{15} W cm^{-2}. This is in accordance with the focal spot size measured with the WFS for the given pulse energy of $E_{pulse} \simeq 20$ µJ and an estimated pulse duration of $T = 50$ fs. In XUV pump–probe operation, the FEL beam is put on both split mirrors. In this configuration, the highest recorded charge state is Xe^{11+}, which according to Sorokin *et al.* (2007*a*) corresponds to an intensity of $I \simeq 5 \times 10^{14}$ W cm^{-2}.

5.2. Pointing stability of the split-mirrors

It is crucial for any pump–probe experiment to maintain spatial overlap of the two foci during delay scans. In order to determine the pointing stability of the split-mirror assembly (*cf.* Section 3.1), the target screen is moved to the nominal focal position in the center of the REMI spectrometer (*cf.* Section 4.3). The FEL intensity needs to be strongly attenuated by the beamline filters (*cf.* Section 4.1) to not destroy the screen. The fluorescence spots of the movable and the fixed focus are then observed by the CCD camera with the optical magnification system from outside (*cf.* Section 4.3).

The CCD camera is read out with the 10 Hz FEL trigger. The two foci are spatially separated by about 150 µm, which allows the centroid positions of the fluorescence spots [spot sizes 64 ± 12 µm (FWHM)] of the movable and the fixed focus to be determined. To this end, both spots are selected by regions of interest. These regions are then projected, background is subtracted and the centroids are calculated from the center-of-mass of the projections. A sub-pixel resolution of below 1.6 µm is reached with this method. The delay is scanned and for each delay step the centroid position of the spot of the movable focus is determined relative to that of the fixed focus in the horizontal (x) and vertical (y) direction. The relative deviation Δx of the centroid positions in the x-direction is plotted as a function of the pump–probe delay in Fig. 13(a).

For this plot, the entire delay range has been scanned four times. Between $\Delta x(-2000$ fs$) = +15$ µm and $\Delta x(+2000$ fs$) = -30$ µm, an absolute deviation of 45 µm exists. Additionally, anharmonic oscillations are superimposed on this almost linear slope. The origin of this non-linear behavior is not understood. It might be caused by an imperfect synchronization of the movements of the three piezo positioners (*cf.* Section 3.1). In order to compensate the slope and the anharmonic oscillations, the position versus delay curve is recorded in a separate calibration measurement and interpolated by splines, which is then used for correcting the movements of the piezo kinematics. Four delay scans using the correction are superimposed in Fig. 13(b). The small width of the distribution [*cf.* inset of Fig. 13(b)] shows the high precision and reproducibility of the piezo kinematics. The 1σ-deviation over the entire delay range is $\sigma_{\Delta x} = (2.2 \pm 0.5)$ µm. In the vertical direction Δy, corrections are also necessary and a comparable stability is achieved as well. Hence, for pump–probe experiments, the two foci are spatially well overlapped when the delay-dependent correction obtained by the method introduced above is applied.
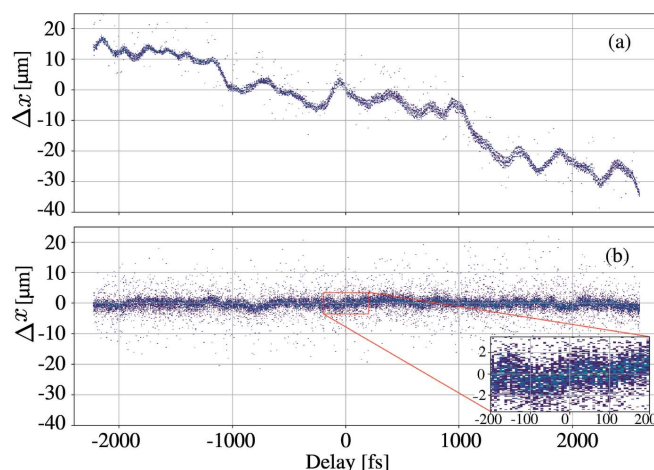
Figure 13
Relative deviation Δx of the centroid positions of the fluorescence spots of the movable and the fixed focus on the target screen as a function of the pump–probe delay. (a) Without correction. (b) With correction. The inset shows a zoom-in between -200 fs and $+200$ fs. For both plots, the delay range is scanned four times.

5.3. Stray-light reduction

Stray light, *i.e.* scattered XUV photons that trigger events at the ion or electron detector of the REMI (*cf.* Section 2.3), is a major source of background events. With the in-line XUV split-delay and focusing optics (*cf.* Section 3), a significant reduction of stray light is achieved compared with a formerly used back-reflecting split-mirror (Jiang *et al.*, 2010*a*; Schnorr *et al.*, 2013). Using similar FEL pulse energies, the stray light background is reduced by a factor of about 15. In the previous setup, an FEL beam of 10 mm diameter first passed the REMI interaction chamber before it was focused into the gas jet. This back-reflecting geometry facilitated undirected scattered photons. With the new split-delay and focusing optics, however, a well collimated FEL beam passes the REMI interaction chamber only once.

5.4. Electron-ion coincidences

As a next step, after commissioning of the FEL beamline, the REMI itself was tested. To this end, two-photon double-ionization (TPDI) of neon at a photon energy $\hbar\omega$ = 44 eV has been studied using the in-line XUV optics (*cf.* Section 3). At a photon energy of 44 eV, TPDI proceeds via the so-called sequential channel: the absorption of one photon leads to the formation of a real intermediate state of the singly charged Ne^+ ion, which then absorbs a second photon resulting in a doubly charged Ne^{2+} ion,

First step: $Ne + \hbar\omega(44 \text{ eV}) \longrightarrow Ne^+ + e_1,$

Second step: $Ne^+ + \hbar\omega(44 \text{ eV}) \longrightarrow Ne^{2+} + e_2.$ (2)
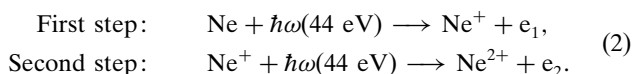
Although the two ionization steps might be regarded as completely independent at first glance, the two ejected electrons (e_1 and e_2) are correlated, which is, for example, reflected in the angular distributions of the first- and second-step electrons (Kheifets, 2007; Fritzsche *et al.*, 2008; Grum-Grzhimailo *et al.*, 2009). To unambiguously measure the angular distribution of the first-step electron in TPDI, this electron needs to be distinguished from an electron emerging from another ionization event. This is possible, if the two ejected electrons (e_1 and e_2) and the corresponding Ne^{2+} ion are measured in coincidence [*cf.* equation (2)].

A so-called photoelectron–photoelectron–photoion coincidence (PePePiCo) map may be used as feedback as to whether the coincident detection of electrons and ions was successful. In such a plot, the ion TOF is plotted against the sum of the TOFs of the first and the second electron arriving at the detector. The PePePiCo plot for TPDI of neon at a photon energy of $\hbar\omega$ = 44 eV is shown in Fig. 14.

In a true coincident event, the sum momentum of all ejected particles (electrons and ions) is constant. As the TOF of a particle is in first approximation directly proportional to its momentum, the diagonal line in Fig. 14 indicates the coincident detection of a Ne^{2+} ion and the two ejected electrons. According to the geometry of the REMI spectrometer (*cf.* Fig. 2), an ion that starts with an initial momentum towards the ion detector has a shorter TOF. Due to momentum conservation, the corresponding electrons start with initial
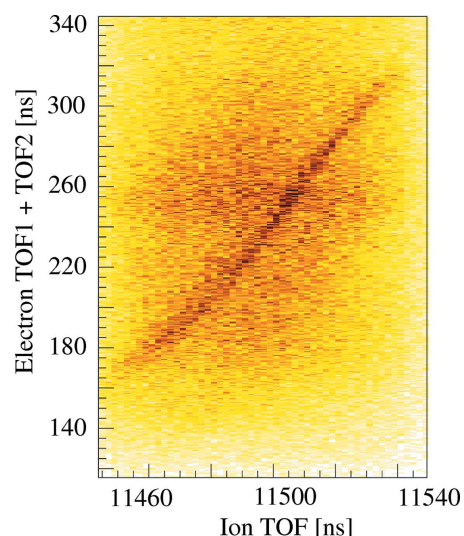
Figure 14
Photoelectron–photoelectron–photoion coincidence (PePePiCo) map for two-photon double ionization of neon at $\hbar\omega$ = 44 eV. The ion TOF is plotted on the horizontal axis. The vertical axis shows the sum of the TOFs of the first and second detected electron impinging on the detector. In total, 1.6×10^7 FEL pulses were taken to produce the histogram. The figure is taken from Schmid (2018).

momenta towards their detector and the sum TOF1 + TOF2 is short as well. In the opposite case, *i.e.* where the ion has an initial momentum towards the electron detector, the ion TOF is larger and thus also the sum TOF of the two electrons is larger. The PePePiCo map of Fig. 14 shows that with the background reduction (*cf.* Section 5.3) achieved by the design of the beamline (*cf.* Section 4.2) and by focusing with the in-line XUV optics (*cf.* Section 3), detailed studies on two- and multi-photon ionization of atoms, molecules and small clusters are possible at the REMI endstation. In contrast to previous experiments, *e.g.* TPDI of Ne at 44 eV has already been studied using a REMI at FLASH1 (Kurka *et al.*, 2009), these studies can now be carried out in a time-resolved manner using the in-line XUV split-delay and focusing optics (*cf.* Section 3).

5.5. Delay-dependent kinetic energy release spectra

The fragmentation of argon dimers (Ar_2) at a photon energy of $\hbar\omega$ = 24.8 eV is taken as a case study to test the pump–probe capability of the split-delay and focusing optics. The kinetic energy release (KER) of the dimer fragments is measured as a function of the pump–probe delay. The KER is approximately given by

$$\text{KER} \simeq \frac{q_1 q_2}{R}, \quad (3)$$

with q_1 and q_2 being the ion charges [atomic units are used in equation (3)]. The dependence of the KER on the internuclear distance R allows conclusions to be drawn on the nuclear dynamics during the fragmentation. In Fig. 15, the KER of the $Ar^+ + Ar^+$ coincidence channel is plotted as a function of the pump–probe delay t_d.
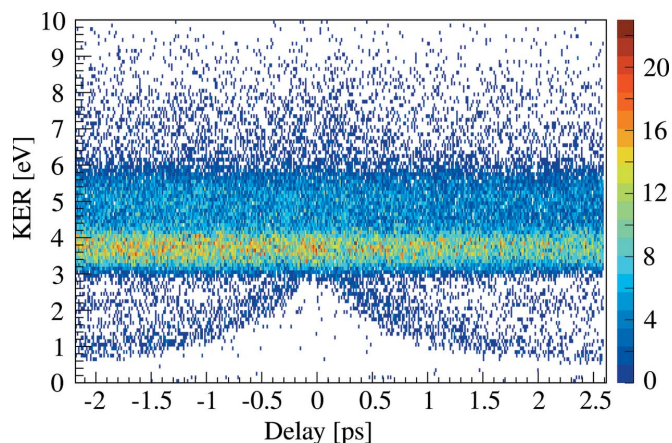
Figure 15
KER of $Ar^+ + Ar^+$ ions as a function of the pump–probe delay. The data are recorded at a photon energy of $\hbar\omega = 24.8$ eV and combined FEL intensities of $I_{FEL} = 10^{13}$–10^{14} W cm^{-2}. The pulse energies in the pump and probe are approximately equal. The figure is taken from Schmid (2018).

Figure 16
PECs of the argon dimer between 10 and 45 eV. The potential energy E is given with respect to the Ar–Ar ground state. For simplification, only a single PEC is plotted to represent $Ar^+(3p^{-2}nl)$–Ar (dark-green) and $Ar^+(3p^{-1})$–$Ar^+(3p^{-1})$ (blue) states. All curves are taken from Stoychev et al. (2008) and Miteva et al. (2014). [Reprinted with the permission of AIP Publishing.] The purple vertical arrows indicate photons of $\hbar\omega = 24.8$ eV. The dashed arrow visualizes the absorption of a second photon in the pump pulse. The Franck–Condon (FC) region lies within the two vertical dashed gray lines. The figure is taken from Schmid (2018).

Over the entire range, delay-independent contributions at 3.8 eV and 5.3 eV are present. They stem from the absorption of two photons within one pulse, the pump or the probe. The contribution at 3.8 eV is assigned to the direct fragmentation at the equilibrium internuclear distance $R_{eq} = 7.18$ a.u. by absorbing two photons. As depicted by the potential energy curves (PECs) in Fig. 16, this happens sequentially via the intermediate $Ar^+(3p^{-1})$–Ar state within one FEL pulse. The contribution at 5.3 eV is induced by an interatomic Coulombic decay (ICD) of a one-site ionized and excited $Ar^+(3p^{-2}nl)$–Ar state (Miteva et al., 2014) (cf. Fig. 16). The decay onto the repulsive $Ar^+(3p^{-1})$–$Ar^+(3p^{-1})$ state takes place at an internuclear distance $R < R_{eq}$, which according to equation (3) results in a higher KER compared with the fragmentation at R_{eq}.

Besides the delay-independent contributions, a pump–probe signal is visible in Fig. 15. It starts at time zero at 3.8 eV and asymptotically reaches KERs of $\sim$1.0 eV for large delays. This signal is attributed to dissociative photoionization. The pump pulse initiates the dissociation of the dimer into a charged and a neutral fragment (cf. Fig. 16),

$$\text{Pump}: \quad Ar-Ar \xrightarrow{XUV} Ar^+(3p^{-1})-Ar. \quad (4)$$

Then, the delayed probe pulse interrupts the dissociation at t_d by ionizing to a doubly charged state (cf. Fig. 16),

$$\text{Probe}: \quad Ar^+(3p^{-1})-Ar \xrightarrow{XUV} Ar^+(3p^{-1})-Ar^+(3p^{-1}). \quad (5)$$

The overall KER is given by the kinetic energy accumulated on the initial $Ar^+(3p^{-1})$–Ar and the final $Ar^+(3p^{-1})$–$Ar^+(3p^{-1})$ PEC,

$$KER = E_{init}(R_{eq}) - E_{init}[R(t_d)] + E_{final}[R(t_d)] - E_{final}(R \rightarrow \infty). \quad (6)$$

For large delays $|t_d| \rightarrow \infty$, $E_{final}[R(|t_d| \rightarrow \infty)] = E_{final}(R \rightarrow \infty)$ and no KER is accumulated on the final $Ar^+(3p^{-1})$–$Ar^+(3p^{-1})$ curve. Thus, the asymptotic KER of $\sim$1.0 eV of $Ar^+ + Ar^+$ ions

is a signature of the $Ar^+(3p^{-1})$–Ar precursor state. The asymptotic limit is reached at large delays $|t_d| \geq 2$ ps, which corresponds to a slow dissociation of the dimer. The visibility of the signal over at least ± 2 ps confirms the pump–probe capability over a large delay range and implies that the setup allows long-lasting dynamics to be traced.

The results presented in Sections 5.4 and 5.5 demonstrate that the in-line XUV split-delay and focusing optics opens up new opportunities for time-resolved electron–ion coincidence spectroscopy at FLASH2.

6. Future upgrades

An IR pump–probe laser is the next upgrade to the FLASH2 facility (FLASH2, 2018). It is also connected to the REMI endstation. The 800 nm laser system is OPCPA based and in the final stage will deliver pulses of sub-20 fs duration in burst-mode (10 Hz bursts with an intra-burst repetition rate of 50 kHz initially). The individual pulses are foreseen to have energies of up to 0.5 mJ. The timing jitter between FEL and IR pulses is initially <50 fs (RMS). With tight focusing, peak IR intensities of >10^{15} W cm^{-2} should be attainable. First experiments at the REMI endstation using the IR pump–probe laser were performed in the end of 2018. The incoupling mirror for the IR laser is installed in the last section of the REMI beamline (colored light-red in Fig. 9). A two-inch

silver-coated plane mirror is mounted on a precision rotational feed-through, which is installed on a triaxial *xyz*-manipulator. To overlap the FEL and the IR beam co-linearly, the IR beam is deflected by 90°. The IR incoupling mirror has a hole of 4 mm diameter for the focused FEL beam to pass through. The IR laser is focused outside of the vacuum by a lens with a focal length of 40 cm. The differential pumping tube between IR incoupling and REMI interaction chamber (4th tube in Fig. 9) has an inner diameter of 22 mm. Thus, an IR beam of ≤35 mm diameter at the position of the lens can pass through the tube without clipping.

In the near future, in cooperation with DESY and the Leibniz University of Hanover, a high harmonic generation (HHG) source will also be integrated into the REMI beamline. This will further extend the portfolio of available radiation sources and allow for two-color VUV–XUV pump–probe spectroscopy.

Furthermore, the in-line geometry of the XUV focusing optics leaves room to re-use the FEL beam in a downstream experiment taking out the photon dump (*cf.* Section 4.3). For example, a grating spectrometer operating on a shot-to-shot level could be useful to correlate the REMI data to the spectra of individual FEL pulses.

The next upgrade of the REMI apparatus itself will include a modular jet system. It will be mounted on rails and thus enables to easily switch between different sample injection systems.

7. Summary

In this contribution, the reaction microscope (REMI) endstation at beamline FL26 of the free-electron laser FLASH2 has been presented. The instrument is dedicated to time-resolved AMO-physics experiments on small quantum systems like atoms, molecules and small clusters by exploiting multi-particle coincidence spectroscopy. The sample injection, the design of the spectrometer, the functionality of the time- and position-sensitive detectors, the vacuum requirements and the data acquisition of the REMI were introduced. The design and the key parts of an in-line XUV split-delay and focusing optics were presented. The optics is based on grazing-incidence mirrors. With this the fast wavelength tunability of the FLASH2 variable-gap undulators can be efficiently exploited in XUV–XUV pump–probe experiments. A dedicated beamline section allows the FEL beam to be monitored and to be aligned before it enters the mirror chamber and the REMI. The beamline also serves as a differential pumping section to maintain UHV conditions of ≤10^{-11} mbar in the REMI interaction chamber. In the design of the beamline, special emphasis has been put on stray-light suppression, which is essential to perform multi-particle coincidence experiments at an FEL. Commissioning results demonstrate in particular the working capability of the in-line XUV split-delay and focusing optics. The endstation will be connected to the FLASH2 pump–probe laser system, which will enable XUV–IR pump–probe experiments in the near future. Further upgrades will contain an HHG source and a modular jet system.

References

Ackermann, W., Asova, G., Ayvazyan, V., Azima, A., Baboi, N., Bähr, J., Balandin, V., Beutner, B., Brandt, A., Bolzmann, A., Brinkmann, R., Brovko, O. I., Castellano, M., Castro, P., Catani, L., Chiadroni, E., Choroba, S., Cianchi, A., Costello, J. T., Cubaynes, D., Dardis, J., Decking, W., Delsim-Hashemi, H., Delserieys, A., Di Pirro, G., Dohlus, M., Düsterer, S., Eckhardt, A., Edwards, H. T., Faatz, B., Feldhaus, J., Flöttmann, K., Frisch, J., Fröhlich, L., Garvey, T., Gensch, U., Gerth, Ch., Görler, M., Golubeva, N., Grabosch, H., Grecki, M., Grimm, O., Hacker, K., Hahn, U., Han, J. H., Honkavaara, K., Hott, T., Hüning, M., Ivanisenko, Y., Jaeschke, E., Jalmuzna, W., Jezynski, T., Kammering, R., Katalev, V., Kavanagh, K., Kennedy, E. T., Khodyachykh, S., Klose, K., Kocharyan, V., Körfer, M., Kollewe, M., Koprek, W., Korepanov, S., Kostin, D., Krassilnikov, M., Kube, G., Kuhlmann, M., Lewis, C. L. S., Lilje, L., Limberg, T., Lipka, D., Löhl, F., Luna, H., Luong, M., Martins, M., Meyer, M., Michelato, P., Miltchev, V., Möller, W. D., Monaco, L., Müller, W. F. O., Napieralski, O., Napoly, O., Nicolosi, P., Nölle, D., Nuñez, T., Oppelt, A., Pagani, C., Paparella, R., Pchalek, N., Pedregosa-Gutierrez, J., Petersen, B., Petrosyan, B., Petrosyan, G., Petrosyan, L., Pflüger, J., Plönjes, E., Poletto, L., Pozniak, K., Prat, E., Proch, D., Pucyk, P., Radcliffe, P., Redlin, H., Rehlich, K., Richter, M., Roehrs, M., Roensch, J., Romaniuk, R., Ross, M., Rossbach, J., Rybnikov, V., Sachwitz, M., Saldin, E. L., Sandner, W., Schlarb, H., Schmidt, B., Schmitz, M., Schmüser, P., Schneider, J. R., Schneidmiller, E. A., Schnepp, S., Schreiber, S., Seidel, M., Sertore, D., Shabunov, A. V., Simon, C., Simrock, S., Sombrowski, E., Sorokin, A. A., Spanknebel, P., Spesyvtsev, R., Staykov, L., Steffen, B., Stephan, F., Stulle, F., Thom, H., Tiedtke, K., Tischer, M., Toleikis, S., Treusch, R., Trines, D., Tsakov, I., Vogel, E., Weiland, T., Weise, H., Wellhöfer, M., Wendt, M., Will, I., Winter, A., Wittenburg, K., Wurth, W., Yeates, P., Yurkov, M. V., Zagorodnov, I. & Zapfe, K. (2007). *Nat. Photon.* **1**, 336–342.

Benvenuti, C., Chiggiato, P., Pinto, P. C., Santana, A. E., Hedley, T., Mongelluzzo, A., Ruzinov, V. & Wevers, I. (1999). *Vacuum*, **53**, 219–225.

Bittner, L., Maschinenphysik, D., Feldhaus, J., Hahn, U., Hesse, M., Jastrow, U., Kocharyan, V., Radcliffe, P., Saldin, E., Schneidmiller, E., Tiedtke, K., Timmann, B., Treusch, R., Bargen, N., Yurkov, M., Brovko, O., Kharlamov, D., Lokhmatov, V., Matyushevskiy, E. & Syresin, E. (2007). *Proceedings of the 29th International Free-Electron Laser Conference (FEL2007)*, 26–31 August 2007, Novosibirsk, Russia.

Braune, M., Brenner, G., Dziarzhytski, S., Juranić, P., Sorokin, A. & Tiedtke, K. (2016). *J. Synchrotron Rad.* **23**, 10–20.

Callegari, C., Prince, K. C. & Ueda, K. (2016). *Synchrotron Radiat. News*, **29**(3), 21–25.

CERN (2018). *ROOT*, https://root.cern.ch/. Last request: 22/12/2018.

beamlines

Dörner, R., Mergel, V., Jagutzki, O., Spielberger, L., Ullrich, J., Moshammer, R. & Schmidt-Böcking, H. (2000). *Phys. Rep.* **330**, 95–192.

Erk, B., Müller, J. P., Bomme, C., Boll, R., Brenner, G., Chapman, H. N., Correa, J., Düsterer, S., Dziarzhytski, S., Eisebitt, S., Graafsma, H., Grunewald, S., Gumprecht, L., Hartmann, R., Hauser, G., Keitel, B., von Korff Schmising, C., Kuhlmann, M., Manschwetus, B., Mercadier, L., Müller, E., Passow, C., Plönjes, E., Ramm, D., Rompotis, D., Rudenko, A., Rupp, D., Sauppe, M., Siewert, F., Schlosser, D., Strüder, L., Swiderski, A., Techert, S., Tiedtke, K., Tilp, T., Treusch, R., Schlichting, I., Ullrich, J., Moshammer, R., Möller, T. & Rolles, D. (2018). *J. Synchrotron Rad.* **25**, 1529–1540.

Faatz, B., Plönjes, E., Ackermann, S., Agababyan, A., Asgekar, V., Ayvazyan, V., Baark, S., Baboi, N., Balandin, V., Bargen, N., Bican, Y., Bilani, O., Bödewadt, J., Böhnert, M., Böspflug, R., Bonfigt, S., Bolz, H., Borges, F., Borkenhagen, O., Brachmanski, M., Braune, M., Brinkmann, A., Brovko, O., Bruns, T., Castro, P., Chen, J., Czwalinna, M. K., Damker, H., Decking, W., Degenhardt, M., Delfs, A., Delfs, T., Deng, H., Dressel, M., Duhme, H., Düsterer, S., Eckoldt, H., Eislage, A., Felber, M., Feldhaus, J., Gessler, P., Gibau, M., Golubeva, N., Golz, T., Gonschior, J., Grebentsov, A., Grecki, M., Grün, C., Grunewald, S., Hacker, K., Hänisch, L., Hage, A., Hans, T., Hass, E., Hauberg, A., Hensler, O., Hesse, M., Heuck, K., Hidvegi, A., Holz, M., Honkavaara, K., Höppner, H., Ignatenko, A., Jäger, J., Jastrow, U., Kammering, R., Karstensen, S., Kaukher, A., Kay, H., Keil, B., Klose, K., Kocharyan, V., Köpke, M., Körfer, M., Kook, W., Krause, B., Krebs, O., Kreis, S., Krivan, F., Kuhlmann, J., Kuhlmann, M., Kube, G., Laarmann, T., Lechner, C., Lederer, S., Leuschner, A., Liebertz, D., Liebing, J., Liedtke, A., Lilje, L., Limberg, T., Lipka, D., Liu, B., Lorbeer, B., Ludwig, K., Mahn, H., Marinkovic, G., Martens, C., Marutzky, F., Maslocv, M., Meissner, D., Mildner, N., Miltchev, V., Molnar, S., Mross, D., Müller, F., Neumann, R., Neumann, P., Nölle, D., Obier, F., Pelzer, M., Peters, H., Petersen, K., Petrosyan, A., Petrosyan, G., Petrosyan, L., Petrosyan, V., Petrov, A., Pfeiffer, S., Piotrowski, A., Pisarov, Z., Plath, T., Pototzki, P., Prandolini, M. J., Prenting, J., Priebe, G., Racky, B., Ramm, T., Rehlich, K., Riedel, R., Roggli, M., Röhling, M., Rönsch-Schulenburg, J., Rossbach, J., Rybnikov, V., Schäfer, J., Schaffran, J., Schlarb, H., Schlesselmann, G., Schlösser, M., Schmid, P., Schmidt, C., Schmidt-Föhre, F., Schmitz, M., Schneidmiller, E., Schöps, A., Scholz, M., Schreiber, S., Schütt, M., Schütz, U., Schulte-Schrepping, H., Schulz, M., Shabunov, A., Smirnov, P., Sombrowski, E., Sorokin, A., Sparr, B., Spengler, J., Staack, M., Stadler, M., Stechmann, C., Steffen, B., Stojanovic, N., Sychev, V., Syresin, E., Tanikawa, T., Tavella, F., Tesch, N., Tiedtke, K., Tischer, M., Treusch, R., Tripathi, S., Vagin, P., Vetrov, P., Vilcins, S., Vogt, M., Wagner, A. Z., Wamsat, T., Weddig, H., Weichert, G., Weigelt, H., Wentowski, N., Wiebers, C., Wilksen, T., Willner, A., Wittenburg, K., Wohlenberg, T., Wortmann, J., Wurth, W., Yurkov, M., Zagorodnov, I. & Zemella, J. (2016). *New J. Phys.* **18**, 062002.

Fechner, L. (2014). *High-Resolution Experiments on Strong-Field Ionization of Atoms and Molecules.* Springer International Publishing.

Feldhaus, J., Krikunova, M., Meyer, M., Möller, T., Moshammer, R., Rudenko, A., Tschentscher, T. & Ullrich, J. (2013). *J. Phys. B At. Mol. Opt. Phys.* **46**, 164002.

FLASH2 (2018). *FLASH2 pump–probe laser system*, http://photon-science.desy.de/facilities/flash/beamlines/optical_laser_systems/index_eng.html. Last request: 12/04/2018.

Fritzsche, S., Grum-Grzhimailo, A. N., Gryzlova, E. V. & Kabachnik, N. M. (2008). *J. Phys. B At. Mol. Opt. Phys.* **41**, 165601.

Gallagher, J. W., Brion, C. E., Samson, J. A. R. & Langhoff, P. W. (1988). *J. Phys. Chem. Ref. Data*, **17**, 9–153.

Gerken, N., Klumpp, S., Sorokin, A. A., Tiedtke, K., Richter, M., Bürk, V., Mertens, K., Juranić, P. & Martins, M. (2014). *Phys. Rev. Lett.* **112**, 213002.

Grum-Grzhimailo, A. N., Gryzlova, E. V., Strakhova, S. I., Kabachnik, N. M. & Fritzsche, S. (2009). *J. Phys. Conf. Ser.* **194**, 012004.

GSI (2018). *Go4*, http://go4.gsi.de/. Last request: 22/12/2018.

Henke, B. L., Gullikson, E. M. & Davis, J. C. (1993). *At. Data Nucl. Data Tables*, **54**, 181–342.

Hikosaka, Y., Fushitani, M., Matsuda, A., Tseng, C.-M., Hishikawa, A., Shigemasa, E., Nagasono, M., Tono, K., Togashi, T., Ohashi, H., Kimura, H., Senba, Y., Yabashi, M. & Ishikawa, T. (2010). *Phys. Rev. Lett.* **105**, 133001.

Hunstig, M. (2017). *Actuators*, **6**, 7.

Jagutzki, O., Cerezo, A., Czasch, A., Dörner, R., Hattas, M., Huang, M., Mergel, V., Spillmann, U., Ullmann-Pfleger, K., Weber, T., Schmidt-Böcking, H. & Smith, G. (2002a). *IEEE Trans. Nucl. Sci.* **49**, 2477–2483.

Jagutzki, O., Mergel, V., Ullmann-Pfleger, K., Spielberger, L., Spillmann, U., Dörner, R. & Schmidt-Böcking, H. (2002b). *Nucl. Instrum. Methods Phys. Res. A*, **477**, 244–249.

Jiang, Y. H., Rudenko, A., Herrwerth, O., Foucar, L., Kurka, M., Kühnel, K. U., Lezius, M., Kling, M. F., van Tilborg, J., Belkacem, A., Ueda, K., Düsterer, S., Treusch, R., Schröter, C. D., Moshammer, R. & Ullrich, J. (2010a). *Phys. Rev. Lett.* **105**, 263002.

Jiang, Y. H., Rudenko, A., Pérez-Torres, J., Herrwerth, O., Foucar, L., Kurka, M., Kühnel, K. U., Toppin, M., Plésiat, E., Morales, F., Martín, F., Lezius, M., Kling, M. F., Jahnke, T., Dörner, R., Sanz-Vicario, J. L., van Tilborg, J., Belkacem, A., Schulz, M., Ueda, K., Zouros, T., Düsterer, S., Treusch, R., Schröter, C. D., Moshammer, R. & Ullrich, J. (2010b). *Phys. Rev. A*, **81**, 051402.

Jousten, K. (2010). *Wutz Handbuch Vakuumtechnik.* Praxis, 10th ed. Wiesbaden: Vieweg + Teubner.

Keitel, B., Plönjes, E., Kreis, S., Kuhlmann, M., Tiedtke, K., Mey, T., Schäfer, B. & Mann, K. (2016). *J. Synchrotron Rad.* **23**, 43–49.

Kheifets, A. S. (2007). *J. Phys. B At. Mol. Opt. Phys.* **40**, F313–F318.

Krikunova, M., Adolph, M., Gorkhover, T., Rupp, D., Schorb, S., Bostedt, C., Roling, S., Siemer, B., Mitzner, R., Zacharias, H. & Möller, T. (2012). *J. Phys. B At. Mol. Opt. Phys.* **45**, 105101.

Kurka, M., Feist, J., Horner, D. A., Rudenko, A., Jiang, Y. H., Kühnel, K. U., Foucar, L., Rescigno, T. N., McCurdy, C. W., Pazourek, R., Nagele, S., Schulz, M., Herrwerth, O., Lezius, M., Kling, M. F., Schöffler, M., Belkacem, A., Düsterer, S., Treusch, R., Schneider, B. I., Collins, L. A., Burgdörfer, J., Schröter, C. D., Moshammer, R. & Ullrich, J. (2010). *New J. Phys.* **12**, 073035.

Kurka, M., Rudenko, A., Foucar, L., Kühnel, K. U., Jiang, Y. H., Ergler, T., Havermeier, T., Smolarski, M., Schössler, S., Cole, K., Schöffler, M., Dörner, R., Gensch, M., Düsterer, S., Treusch, R., Fritzsche, S., Grum-Grzhimailo, A. N., Gryzlova, E. V., Kabachnik, N. M., Schröter, C. D., Moshammer, R. & Ullrich, J. (2009). *J. Phys. B At. Mol. Opt. Phys.* **42**, 141002.

Lampton, M., Siegmund, O. & Raffanti, R. (1987). *Rev. Sci. Instrum.* **58**, 2298–2305.

Magrakvelidze, M., Herrwerth, O., Jiang, Y. H., Rudenko, A., Kurka, M., Foucar, L., Kühnel, K. U., Kübel, M., Johnson, N. G., Schröter, C. D., Düsterer, S., Treusch, R., Lezius, M., Ben-Itzhak, I., Moshammer, R., Ullrich, J., Kling, M. F. & Thumm, U. (2012). *Phys. Rev. A*, **86**, 013415.

Meister, S. (2016). Master thesis, University of Heidelberg, Germany.

Miteva, T., Chiang, Y.-C., Kolorenč, P., Kuleff, A., Gokhberg, K. & Cederbaum, L. S. (2014). *J. Chem. Phys.* **141**, 064307.

Moshammer, R., Jiang, Y. H., Foucar, L., Rudenko, A., Ergler, T., Schröter, C. D., Lüdemann, S., Zrost, K., Fischer, D., Titze, J., Jahnke, T., Schöffler, M., Weber, T., Dörner, R., Zouros, T., Dorn, A., Ferger, T., Kühnel, K. U., Düsterer, S., Treusch, R., Radcliffe, P., Plönjes, E. & Ullrich, J. (2007). *Phys. Rev. Lett.* **98**, 203001.

Moshammer, R. & Schnorr, K. (2014). *Molecular Physics and Gas-Phase Chemistry with Free-Electron Lasers*, pp. 1–29. Cham: Springer International Publishing.

Moshammer, R., Unverzagt, M., Schmitt, W., Ullrich, J. & Schmidt-Böcking, H. (1996). *Nucl. Instrum. Methods Phys. Res. B*, **108**, 425–445.

Noll, T., Holldack, K., Reichardt, G., Schwarzkopf, O. & Zeschke, T. (2009). *Precis. Eng.* **33**, 291–304.

Plönjes, E., Faatz, B., Kuhlmann, M. & Treusch, R. (2016). *AIP Conf. Proc.* **1741**, 020008.

Pontius, N., Beye, M., Trabant, C., Mitzner, R., Sorgenfrei, F., Kachel, T., Wöstmann, M., Roling, S., Zacharias, H., Ivanov, R., Treusch, R., Buchholz, M., Metcalf, P., Schüssler-Langeheine, C. & Föhlisch, A. (2018). *Struct. Dyn.* **5**, 054501.

Richter, M., Amusia, M. Y., Bobashev, S. V., Feigl, T., Juranić, P. N., Martins, M., Sorokin, A. A. & Tiedtke, K. (2009). *Phys. Rev. Lett.* **102**, 163002.

Rudenko, A., Jiang, Y. H., Kurka, M., Kühnel, K. U., Foucar, L., Herrwerth, O., Lezius, M., Kling, M. F., Schröter, C. D., Moshammer, R. & Ullrich, J. (2010). *J. Phys. B At. Mol. Opt. Phys.* **43**, 194004.

Sauppe, M., Rompotis, D., Erk, B., Bari, S., Bischoff, T., Boll, R., Bomme, C., Bostedt, C., Dörner, S., Düsterer, S., Feigl, T., Flückiger, L., Gorkhover, T., Kolatzki, K., Langbehn, B., Monserud, N., Müller, E., Müller, J. P., Passow, C., Ramm, D., Rolles, D., Schubert, K., Schwob, L., Senftleben, B., Treusch, R., Ulmer, A., Weigelt, H., Zimbalski, J., Zimmermann, J., Möller, T. & Rupp, D. (2018). *J. Synchrotron Rad.* **25**, 1517–1528.

Schmid, G. (2018). PhD thesis, University of Heidelberg, Germany.

Schnorr, K. (2014). PhD thesis, University of Heidelberg, Germany.

Schnorr, K., Senftleben, A., Kurka, M., Rudenko, A., Foucar, L., Schmid, G., Broska, A., Pfeifer, T., Meyer, K., Anielski, D., Boll, R., Rolles, D., Kübel, M., Kling, M. F., Jiang, Y. H., Mondal, S., Tachibana, T., Ueda, K., Marchenko, T., Simon, M., Brenner, G., Treusch, R., Scheit, S., Averbukh, V., Ullrich, J., Schröter, C. D. & Moshammer, R. (2013). *Phys. Rev. Lett.* **111**, 093402.

Schnorr, K., Senftleben, A., Kurka, M., Rudenko, A., Schmid, G., Pfeifer, T., Meyer, K., Kübel, M., Kling, M. F., Jiang, Y. H., Treusch, R., Düsterer, S., Siemer, B., Wöstmann, M., Zacharias, H., Mitzner, R., Zouros, T. J. M., Ullrich, J., Schröter, C. D. & Moshammer, R. (2014). *Phys. Rev. Lett.* **113**, 073001.

Scoles, G. (1988). *Atomic and Molecular Beam Methods: 1. Atomic and Molecular Beam Methods.* Oxford University Press.

Sorokin, A. A., Bobashev, S. V., Feigl, T., Tiedtke, K., Wabnitz, H. & Richter, M. (2007a). *Phys. Rev. Lett.* **99**, 213002.

Sorokin, A. A., Wellhöfer, M., Bobashev, S. V., Tiedtke, K. & Richter, M. (2007b). *Phys. Rev. A*, **75**, 051402.

Stoychev, S. D., Kuleff, A. I., Tarantelli, F. & Cederbaum, L. S. (2008). *J. Chem. Phys.* **128**, 014307.

Tiedtke, K., Azima, A., von Bargen, N., Bittner, L., Bonfigt, S., Düsterer, S., Faatz, B., Frühling, U., Gensch, M., Gerth, C., Guerassimova, N., Hahn, U., Hans, T., Hesse, M., Honkavaar, K., Jastrow, U., Juranic, P., Kapitzki, S., Keitel, B., Kracht, T., Kuhlmann, M., Li, W. B., Martins, M., Núñez, T., Plönjes, E., Redlin, H., Saldin, E. L., Schneidmiller, E. A., Schneider, J. R., Schreiber, S., Stojanovic, N., Tavella, F., Toleikis, S., Treusch, R., Weigelt, H., Wellhöfer, M., Wabnitz, H., Yurkov, M. V. & Feldhaus, J. (2009). *New J. Phys.* **11**, 023029.

Ullrich, J., Moshammer, R., Dorn, A., Dörner, R., Schmidt, L. & Schmidt-Böcking, H. (2003). *Rep. Prog. Phys.* **66**, 1463–1545.

Usenko, S., Przystawik, A., Jakob, M. A., Lazzarino, L. L., Brenner, G., Toleikis, S., Haunhorst, C., Kip, D. & Laarmann, T. (2017). *Nat. Commun.* **8**, 15626.

Wiley, W. C. & McLaren, I. H. (1955). *Rev. Sci. Instrum.* **26**, 1150–1157.

Wiza, J. (1979). *Nucl. Instrum. Methods*, **162**, 587–601.

Yabashi, M., Tanaka, H., Tanaka, T., Tomizawa, H., Togashi, T., Nagasono, M., Ishikawa, T., Harries, J. R., Hikosaka, Y., Hishikawa, A., Nagaya, K., Saito, N., Shigemasa, E., Yamanouchi, K. & Ueda, K. (2013). *J. Phys. B At. Mol. Opt. Phys.* **46**, 164001.

Yeh, J. J. & Lindau, I. (1985). *At. Data Nucl. Data Tables*, **32**, 1–155.

Zewail, A. H. (1988). *Science*, **242**, 1645–1653.

Zewail, A. H. (2000). *J. Phys. Chem. A*, **104**, 5660–5694.

4.2 Review of the REMI endstation

This paper gives an overview of the FLASH REMI endstation including its extensions since the first commissioning and a selection of experiments.

The first major extension is a short pulsed IR laser provided by DESY [70], which can be used in combination with the FEL. This allows to perform XUV-IR pump-probe measurements like the ones presented in sections 4.3 and 4.4. The second extension is an XUV radiation source based on high-harmonic generation [71]. This project is a collaboration between MPIK, DESY and the University of Hanover. The combination of FEL-XUV radiation, IR laser radiation and HHG-based XUV radiation is unique and opens up a variety of new AMO experiments.

In the second half of the paper three exemplary experiments are presented. They illustrate which quantities can be measured with the REMI, what kind of targets can be used and how different light sources can be combined.

Atomic, Molecular and Cluster Science with the Reaction Microscope Endstation at FLASH2

Severin Meister [1],*[ID]**, Hannes Lindenblatt** [1][ID]**, Florian Trost** [1][ID]**, Kirsten Schnorr** [2][ID]**,
Sven Augustin** [2][ID]**, Markus Braune** [3][ID]**, Rolf Treusch** [3][ID]**, Thomas Pfeifer** [1][ID]
and Robert Moshammer [1]

[1] Max-Planck-Institute for Nuclear Physics, 69117 Heidelberg, Germany;
hannes.lindenblatt@mpi-hd.mpg.de (H.L.); trost@mpi-hd.mpg.de (F.T.);
thomas.pfeifer@mpi-hd.mpg.de (T.P.); r.moshammer@mpi-hd.mpg.de (R.M.)
[2] Paul Scherrer Institute, 5232 Villigen, Switzerland; kirsten.schnorr@psi.ch (K.S.); sven.augustin@psi.ch (S.A.)
[3] Deutsches Elektronen-Synchrotron, 22607 Hamburg, Germany; markus.braune@desy.de (M.B.);
rolf.treusch@desy.de (R.T.)
* Correspondence: severin.meister@mpi-hd.mpg.de; Tel.: +49-6221-516-438

Abstract: The reaction microscope (REMI) endstation for atomic and molecular science at the free-electron laser FLASH2 at DESY in Hamburg is presented together with a brief overview of results recently obtained. The REMI allows coincident detection of electrons and ions that emerge from atomic or molecular fragmentation reactions in the focus of the extreme-ultraviolet (XUV) free-electron laser (FEL) beam. A large variety of target species ranging from atoms and molecules to small clusters can be injected with a supersonic gas-jet into the FEL focus. Their ionization and fragmentation dynamics can be studied either under single pulse conditions, or for double pulses as a function of their time delay by means of FEL-pump–FEL-probe schemes and also in combination with a femtosecond infrared (IR) laser. In a recent upgrade, the endstation was further extended by a light source based on high harmonic generation (HHG), which is now available for upcoming FEL/HHG pump–probe experiments.

Keywords: atom; molecule; REMI; endstation; FLASH

1. Introduction

The invention of intense femtosecond infrared (IR) lasers [1] led to a new era in atomic and molecular physics, namely the devolopment of femtochemistry [2]. Today it is often mentioned as one part of a much larger multi-disciplinary field called ultra-fast physics [3]; the observation of light-induced dynamics in small quantum systems on their natural time scale in the range of femto- or even attoseconds. In many cases a first "pump" pulse triggers certain dynamics, while a delayed "probe" pulse is used to interrogate the system at a later point in time. This way, the temporal evolution of any specific process under investigation like molecular break-up [4], charge migration [5,6] or isomerization [7] within a molecule, to just name a few, can be observed on their natural time scale by using lasers with correspondingly short pulse lengths in the range of a few femtoseconds. A small number of different technologies exists to produce such short laser-like or coherent light pulses. Depending on the specific application each of them comes with characteristic advantages and drawbacks.

Free-electron lasers (FELs) are large-scale electron-accelerator-based machines. They cover a huge range of photon energies, from the microwave [8] up to the hard X-ray regime [9], with unsurpassed light intensities for photon energies above 10 eV [3,10]. However, most FELs are operated at comparably

low repetition rates (typically below 1 kHz) and are providing light pulses that are usually only partly coherent. In contrast, conventional femtosecond lasers in the visible or IR-range provide pulses with high repetition rates, high intensities and excellent coherence properties [1,11,12]. However, their spectral range is limited to photon energies of a few eV only. This limitation is resolved with high harmonic-generation (HHG) sources [13,14], where high-intensity femtosecond IR laser pulses are sent into a gaseous target to drive a non-linear light-atom interaction. This leads to the emission of frequency up-converted (higher harmonic) radiation [15] with unique temporal and spectral properties. HHG sources are ideally suited to produce extremely short pulse durations of only few tens of attoseconds [16] with photon energies of up to several hundred eV [17]. However, these sources are limited, due to the low conversion efficiencies, to light intensities that are orders of magnitude lower than those delivered by modern XUV or X-ray free-electron lasers [18].

For studies of time-dependent processes in small quantum systems it is of great advantage if an experimental station allows high flexibility with respect to the usage of one or a combination of the above mentioned light sources, which are ideally adapted to the given reaction dynamics. With the reaction microscope (REMI) endstation at FLASH2, we implemented this to a large extent. In its present stage, it routinely allows FEL-based pump–probe experiments with atomic, molecular or cluster targets in the gas phase. The experimental station consists of a multi-particle imaging spectrometer for electrons and ions (REMI), the FEL beamline with integrated split-and-delay and focussing optics for FEL pulse-pair creation [19], an IR laser for femtosecond FEL-pump laser-probe experiments, and a laser-driven HHG source for two-color XUV pump–probe measurements. A manuscript about technical details and benchmarks of the REMI endstation can be found in [19]. In contrast, this review provides with information about physical quantities and experimental schemes which are accessible by the REMI endstation. The following manuscript describes in Section 2 the experimental capabilities of the REMI endstation at FLASH2 and a selection of published results (Sections 3.2 and 3.3) as well as unpublished results (Section 3.1) is briefly discussed. Concluding statements are given in Section 4.

2. Experimental Setup

A design drawing of the REMI endstation with its main components is shown in Figure 1. It is installed at beamline FL26 in the experimental hall of FLASH2. Along the beamline, several diagnostic and beam shaping elements like imaging screens, apertures and slits can be inserted into the beampath. In the subsequent section the FEL beam impinges on the split-delay and focussing optics. The former consists of two planar mirrors that are stacked one upon the other to cut the incoming beam geometrically into two co-propagating half-moon shaped beams. By moving one planar mirror with respect to the other, a small change of the path length can be introduced, which leads to a temporal delay of one of the two pulses. The delay range is ±2500 fs, with a resolution better than 1 fs. The ellipsoidal focussing mirror has a focal length of 1 m. It creates a demagnified image of the FEL source-point (the FEL undulator is about 85 m upstream) in the center of the REMI chamber. Wavefront-sensor measurements yield an optimized focus size of about 5 µm diameter [19]. The split and delay function is optional, as each planar mirror is large enough to reflect the full FEL beam on its own surface, if centered in the beam. With the given mirror coating and the grazing incidence geometry, the overall transmission is better than 50% for all photon energies up to 180 eV. A more detailed description of the setup with limits and benchmarks can be found in Ref. [19].

2.1. The Free-Electron Laser FLASH2

The XUV free-electron laser FLASH is the first short-wavelength FEL and went into user operation in 2005 at DESY in Hamburg [20]. FLASH2 is an extension of FLASH that came into operation in 2016 ([21,22]). It shares the electron accelerator with FLASH1, but features its own set of undulators. Compared to FLASH1, the FLASH2 undulators have variable gaps allowing a fast change or a scan of the photon wavelength over a large range. Due to the shared accelerator and the fixed undulator gaps at FLASH1, the accessible wavelengths of FLASH2 depend on the delivered wavelength at FLASH1.

It ranges from the delivered wavelength at FLASH1 to approximately three times this wavelength, for a given accelerator setup [22]. Lasing in the undulator is achieved by self-amplified spontaneous emission (SASE), which results in short (10 to 200 fs [23]) and intense FEL pulses at the expense of a limited pulse-to-pulse stability with respect to intensity and spectral properties, when compared to optical lasers. FLASH2 delivers photon energies in a range from 14 to 310 eV. For light in the REMI, the upper limit is 180 eV due to the dropping reflectivity of carbon-coated mirrors under 8°. FLASH generates electron bunches, and hence photon pulses, in a burst mode. The pulse pattern consists of short pulse trains repeating at 10 Hz. Each pulse train has a length of typically 500 μs and comprises up to 500 pulses, resulting in a maximum intra-train repetition rate of 1 MHz. Averaged over time, a maximum repetition rate of 5 kHz can be delivered.
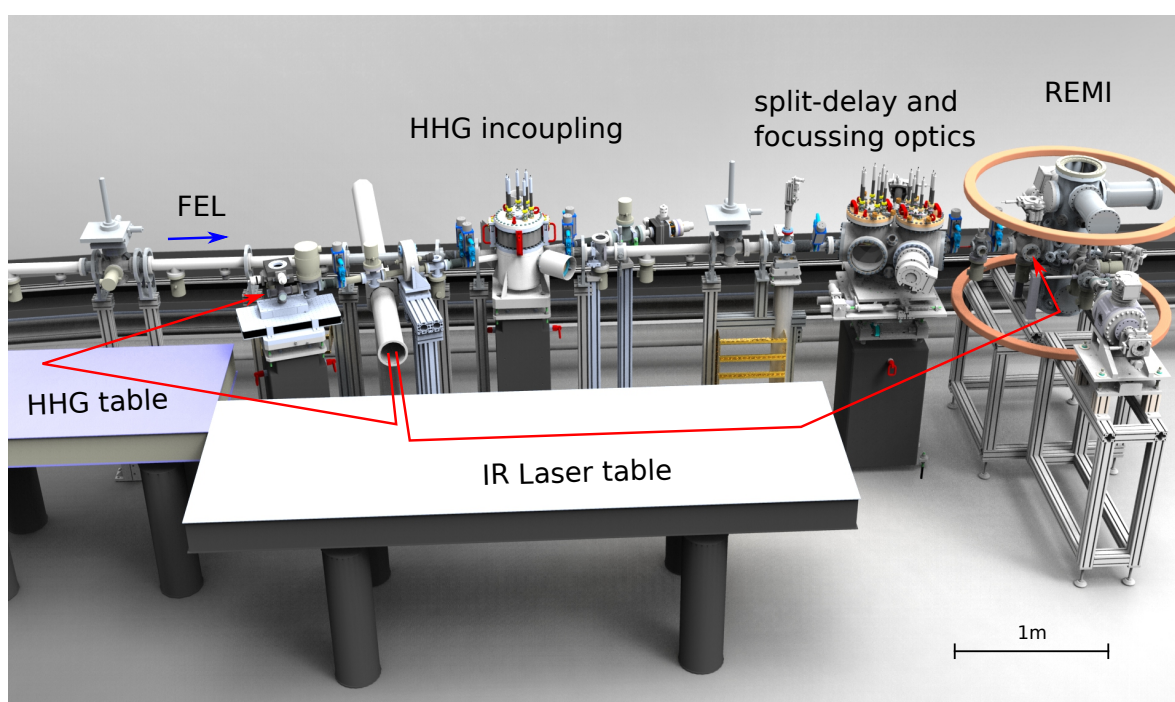
Figure 1. Overview of the reaction microscope (REMI) endstation. The free-electron laser (FEL) is delivered from the left, while the infrared (IR) laser is delivered from the rear, crossing below the beamline. The IR is coupled into the beamline right before the REMI with a holey mirror. The HHG (high harmonic-generation) light is coupled by a grazing angle about 3 m upstream (indicated by the two red arrows).

2.2. IR Laser

For XUV-IR pump–probe experiments, an 800 nm OPCPA (optical parametric chirped pulse amplification) IR-laser is operated by DESY. Pulse energies up to 500 μJ and pulse durations <15 fs can be delivered at a high repetition rate. The IR laser is synchronized to the pulse pattern of the FLASH and presently runs at a repetition rate of 100 kHz in 800 μs bursts, repeating every 100 ms (further specifications can be found in Ref. [24]). The IR laser is coupled into the FEL beamline under 90 degrees by a silver-coated planar mirror. At this position, the FEL is focused down to less than 3 mm in diameter and passes through a 4 mm hole in this incoupling mirror. From this point on, the FEL and the IR beam travel collinearly. An IR-focussing lens with a focal length of 50 cm is placed outside the vacuum. Spatial overlap is set by means of a Ce:YAG-powder coated screen in the focal plane inside the REMI. The two foci of the FEL and the IR-laser on the screen can be observed with a CCD camera and magnifying optics [19]. Temporal overlap with nanosecond precision can be found with a fast photodiode downstream of the REMI. In order to exactly overlap the pulses in time, one uses a target with a well known pump–probe signal. The chosen target (e.g., helium, xenon) depends on the FEL

photon energy and usually involves a specific excitation and a following ionization step which is just possible for the right temporal order of FEL and IR.

2.3. HHG Radiation

The setup of the HHG source is a result of a collaboration between MPIK, DESY and the university of Hanover [25]. The IR beam is transferred to a neighboring laser table where high harmonics in the XUV regime are generated in a noble-gas target [26]. The generated XUV light can be separated from the fundamental IR, either with an aluminum filter or a sufficiently small aperture, as the IR has a larger divergence than the XUV. First runs of the HHG source were successful and commissioning results can be found in Ref. [25]. The HHG-XUV light is coupled into the FEL beamline by a mirror under 8° grazing incidence. The XUV beam has a vertical offset of 7.5 mm with respect to the FEL. In this configuration, each of the two light pulses (HHG and FEL) is reflected on a separate half of the split mirror and can be steered and delayed with respect to each other.

2.4. Reaction Microscope

With the reaction microscope [27] ionization and fragmentation processes of single atoms or molecules are studied. As depicted in Figure 2, laser beam and target gas jet are oriented orthogonally to each other and cross in the center of the REMI. A stack of metal rings produces a homogeneous electric field that separates positively and negatively charged particles and guides them onto the detectors. Helmholtz coils generate a homogeneous magnetic field forcing the electrons on a spiral trajectory to ensure large acceptance for electrons with large transversal momentum inside the spectrometer. Each of the two time- and position-sensitive detectors is composed of a set of micro channel plates and a delay line anode [28]. Time-of-flight information and the impact position on the detector allow to calculate the initial momentum at the time when the charged particle was created. Momentum conservation in three-dimension is used to sort out all particles originating from the same fragmenting target particle, that is finding coincident particles. Angle- and energy-resolved measurements of charged particles in multi-coincidence are the key features of the REMI and enable to investigate atomic and molecular processes in detail [5,6,29,30].
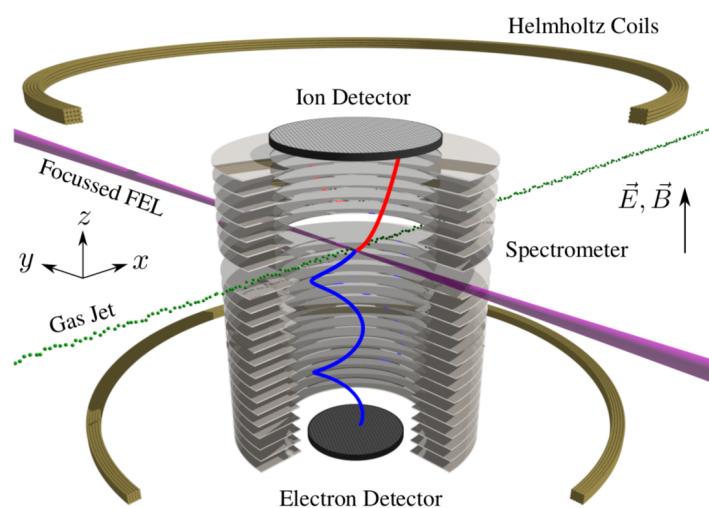
Figure 2. Schematic of the reaction microscope. Reproduced from [19], with the permission of the International Union of Crystallography.

3. Selected Results

3.1. Angle-Resolved Wavelength Scan: XUV+IR in Helium

This experiment makes use of the wavelength tunability of FLASH2 and the 4π angular acceptance of the reaction microscope. As will be shown in the following, it demonstrates a beneficial combination of the FEL and the IR laser.

In this pump–probe measurement the XUV light of the FEL was used to excite helium, while a subsequent IR-laser pulse ionizes the excited atom. Scanning the XUV photon energy from 20.4 eV to just below the ionization threshold of 24.6 eV reveals the excitation transition series $1s^2 \rightarrow 1snp$ in helium [31], in accordance with the dipole selection rules for linearly polarized light. The excited helium atom absorbs multiple photons (each 1.55 eV) of the subsequent IR pulse which bring the electron to the continuum. This process is shown in Figure 3a, where an increased photoelectron yield is observed at XUV energies that matches the specific excitation energy ($1s2p$ at 21.2 eV, $1s3p$ at 23 eV . . .). The distribution of the photoelectron kinetic energy is plotted along the ordinate and shows several peaks at specific XUV excitation energies. The underlying process is the above threshold ionization (ATI) and describes the behavior of an electron absorbing more photons than the minimal requirement to be emitted into the continuum [32,33]. The additional electron energy is directly related to the IR-photon energy (in this case ≈ 1.55 eV).
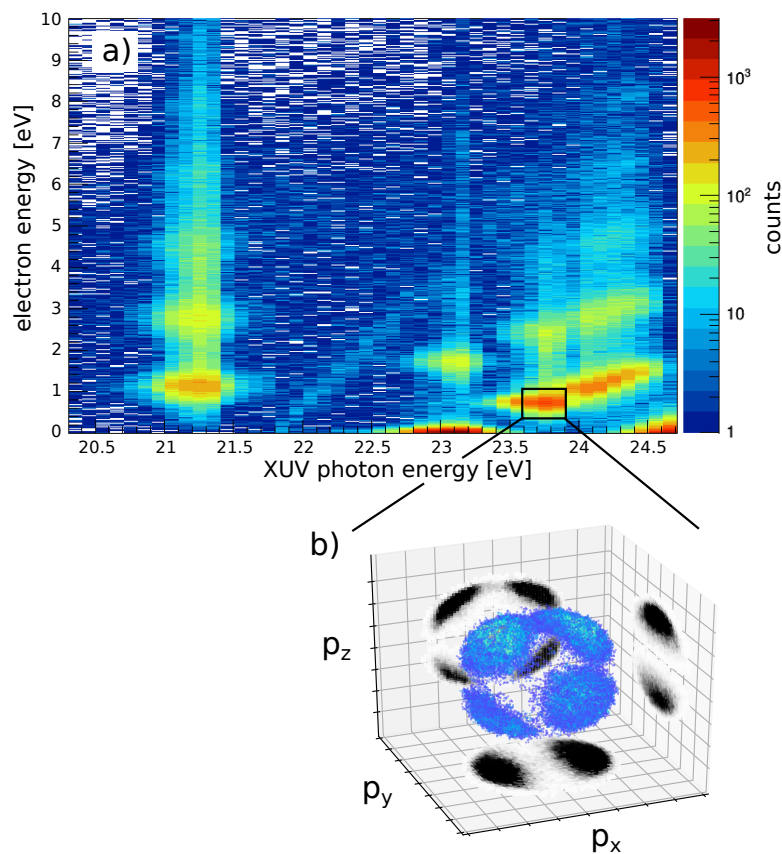
Figure 3. (**a**) XUV photon energy scan with delayed IR-laser pulse, plotted versus photoelectron kinetic energy. Resonances in helium are revealed for specific XUV energies and above threshold ionization (ATI) can be seen by the distribution of the photoelectron kinetic energy. (**b**) Electron momentum distribution at the specific region indicated by the black square. The XUV is polarized along p_x, the IR along p_z.

While in Figure 3a only the absolute electron kinetic energy is plotted, the REMI allows to measure the electron momentum in 3D as shown in Figure 3b. The XUV is polarized along the p_x direction and

the IR laser along the p_z direction. Figure 3b contains exclusively electrons recorded with parameters in the marked region of Figure 3a. First an XUV photon excites the helium atom into the $1s4p$ state (23.7 eV) and upon the additional absorption of one IR photon, the 4p-electron is emitted into the continuum. Starting from the helium groundstate, the absorption of two photons can yield to an angular momentum of $l = 2$ for the photoelectron, with the corresponding characteristic number of nodes in the angular distribution. The two orthogonal linearly polarized light fields can lead to the population of angular momentum substates with $m = 0, \pm 2$. This can be understood as in a spherical basis each light field can be described by a superposition of left- and right-handed circulary polarized light, driving $\Delta m = \pm 1$ transitions. For a detailed explanation see [34].

This experiment demonstrates the capability to precisely measure electron angular distributions which is essential to investigate many different phenomena like quantum beating [35], electron correlation [36] or propensity rules [37].

3.2. Two-Photon Double Ionization in Argon

In a kinematically complete experiment, double ionization of argon by absorption of two photons was measured [30]. Neutral argon atoms were irradiated by FEL radiation with a photon energy of 27.93 eV (averaged peak intensity $(3 \pm 2) \times 10^{13}$ W/cm^2, pulse duration approximately 50 fs). The angular distributions of the ejected photoelectrons during two-photon double ionization (TPDI) were measured. The dominant TPDI channel observed was sequential double ionization (SDI), in which both photoelectrons were emitted from the argon atom by sequential single-photon absorption (see also [38]). The two photoelectrons were confirmed to be correlated through polarization of the intermediate Ar$^+$ state. As a result, the measured angular distributions of both, the first and the second, photoelectron differ from that of the single ionization. In addition, the coincident detection method led to the discovery of the crucial role of autoionization in both steps of SDI in argon.

Both the ion and the electron detector of the REMI have multi-hit capability. This is necessary for the coincident detection of the two photoelectrons emerging from one TPDI event. Additionally, Ar$^+$ ions were measured in coincidence with the photoelectrons. This allows to differentiate between particles stemming from single ionization and the SDI channel. As both processes occur during the same experiment, the influence of systematic errors can be greatly reduced by comparing results from these two ionization pathways.

Figure 4 shows the two-dimensional kinetic energy spectrum of two photoelectrons detected in coincidence. Because the second ionization potential of argon lies just below the photon energy of the FEL radiation, there is one fast (first) and one slow (second) photoelectron expected during SDI [39]. This feature of correlated electrons in SDI is shown in Figure 4, where the kinetic energy of two photoelectrons created within one XUV pulse are plotted against each other. There is an increased yield of photoelectrons at positions where one photoelectron has a kinetic energy of 12 eV and where the other electron has a kinetic energy of 0.3 eV. The increased photoelectron yield at $E_1 = 12$ eV and $E_2 = 12$ eV shows uncorrelated electrons and can be attributed to electrons from two independent single ionization processes. The capability to record such two-dimensional energy spectra of reaction fragments detected in coincidence underlines the aptitude of the REMI as a versatile AMO (atomic, molecular, and optical physics) science station. The dynamics following multi-photon absorption processes in the XUV range is kinematically completely accessible.
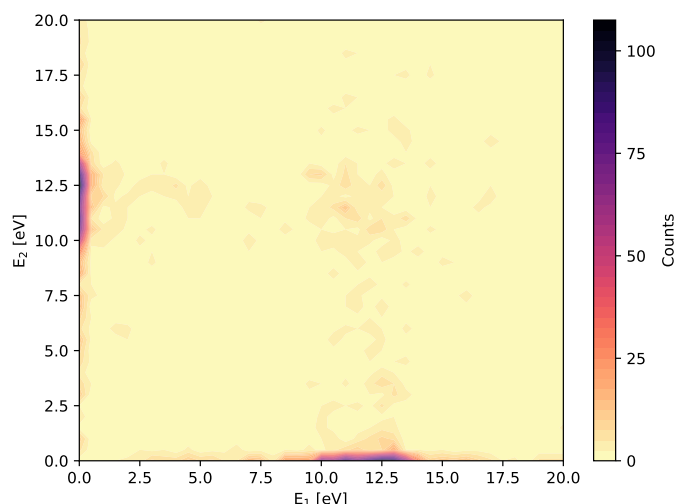
Figure 4. Two-dimensional kinetic energy spectrum of photoelectrons originating from the same laser pulse in two-photon double ionization (TPDI) in argon. The clustering at low E_1 and low E_2 are the signature of the sequential double ionization (SDI) channel. The blob on the diagonal is caused by false coincidences. Reproduced and modified from [30].

3.3. Molecular Dynamics in Ar Dimers

The pump–probe technique combined with fragment ion momentum imaging allows to track the evolution of intermediate states through observables in the final state as a function of the pump–probe delay [6].

The key observables to track molecular dynamics in REMI experiments are the yield of a specific coincidence channel and the kinetic energy release (KER) of this channel. The KER is the sum of the nuclear kinetic energies, which are generated from potential energy. While the system evolves along the potential energy curve of the intermediate state it accumulates the kinetic energy $KER_{nl}(t_d)$, until it is probed at the time t_d and at the internuclear distance $R(t_d)$. Then it accumulates further energy on the final state potential $KER_f(t_d)$ and we observe the sum $KER(t_d) = KER_{nl}(t_d) + KER_f(t_d)$ (see Figure 5).

The capabilities to observe molecular dynamics with this setup is demonstrated exemplarily in an experiment investigating charge transfer (CT) in argon dimers using an XUV-pump IR-probe scheme [5]. The experiment was performed at FLASH1, using the same reaction microscope apparatus, but a different IR pump laser [40]. Argon dimers were ionized and excited to $Ar^{2+*}-Ar$ states by absorption of three 27 eV photons. These states are still weakly bound, but the equilibrium nuclear distance is much smaller. So the nuclei start to move towards each other. At smaller internuclear distances, the potential energy curve crosses unbound states of the $Ar^{+*}-Ar^+$ type which are coupled nonadiabatically so charge transfer can happen there (see Figure 5).

The system is subsequently probed by an intense 800 nm laser pulse [40] to the $Ar^{2+}-Ar^+$ final state. This transition is only possible if charge transfer has taken place. Therefore the yield of this particular channel gives information on the transition probability of the charge transfer. In this process we actually have two intermediate states. The first can only contribute negligible kinetic energy as the potential is shallow. Thus the KER is accumulated mainly on the second intermediate state and the final state.

The value of interest is the time constant when the system transfers its charge and thus changes from the first to the second intermediate. Restricting the KER to values corresponding to the distance R_X, where crossings appear, allows to select those events that were probed directly after the charge is transferred (see Figure 6). With this restriction, the probe pulse directly tracks the transition rate depending on the time delay. This shows how the measurement of KERs combined with ion yields

for varying pump–probe delays, allows to deduce the transition rates of the process of interest as a function of time.
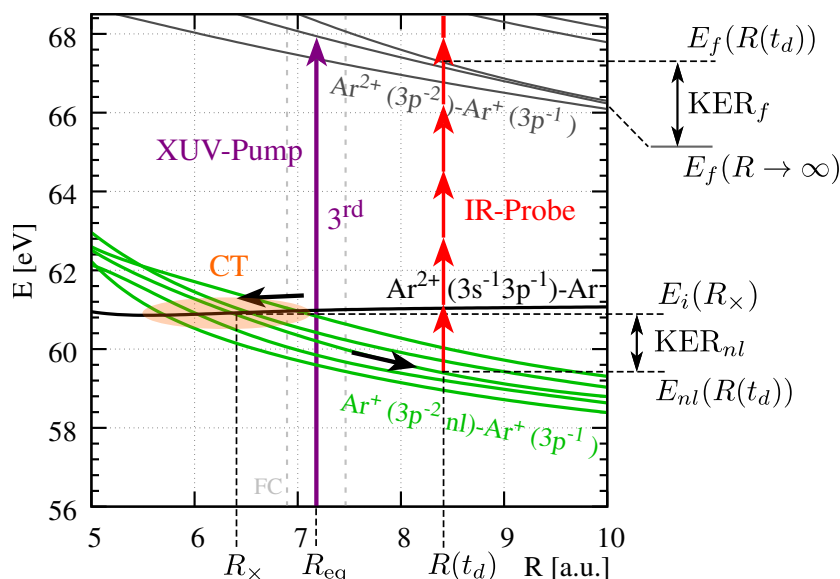
Figure 5. Potential energy curves of the argon dimer in the energy range $56\,\text{eV}$–$68.5\,\text{eV}$. The XUV pump (purple arrow) populates the initial $Ar^{2+}(3s^{-1}\,3p^{-1})-Ar$ state (black curve) at R_{eq}. The wave packet starts to evolve to smaller R. At the crossings (orange-shaded area) with $Ar^{+}(3p^{-2}\,nl)-Ar^{+}(3p^{-1})$ states (light-green curves), charge transfer (CT) happens. The IR probe (red arrows) interrogates the population of the $Ar^{+}(3p^{-2}\,nl)-Ar^{+}(3p^{-1})$ states by ionization to final $Ar^{2+}(3p^{-2})-Ar^{+}(3p^{-1})$ states (dark-grey curves). Specific potential energies and corresponding internuclear distances are indicated by horizontal and vertical dashed lines, respectively. Reproduced from [5], with the permission of AIP (American Institute of Physics) Publishing.
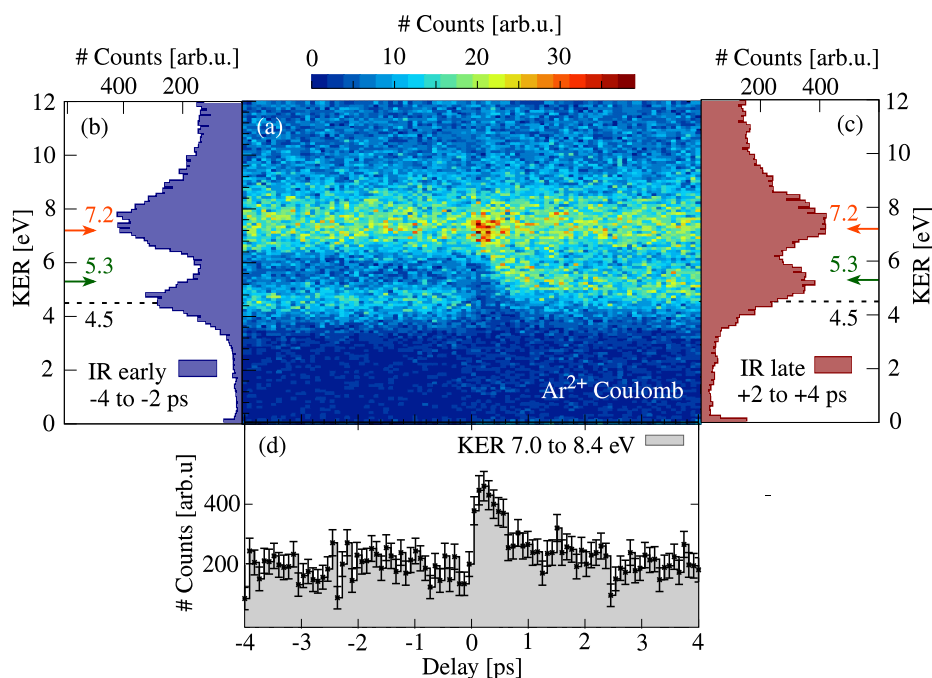
Figure 6. Coulomb-exploded Ar^{2+} ions (non-coincident). (**a**) KER (kinetic energy release) vs. delay. For negative delays, the IR is early with respect to the XUV pulse, for positive delays vice versa. (**b**) Projection of all KERs within -4 to $-2\,$ps onto the KER axis. (**c**) Same as (**b**), but for $+2$ to $+4\,$ps. (**d**) Projection of all KERs between 7.0 to 8.4 eV onto the delay axis. Reproduced from [5], with the permission of AIP Publishing.

4. Conclusions

We have presented the REMI endstation at FLASH2. The unique combination of a reaction microscope and three state-of-the-art light sources opens up the possibilities for unprecedented investigations in the field of atomic and molecular physics.

The sophisticated detection scheme of the REMI enables to measure charged fragments' momenta in 3D and in a coincident manner, which makes it an outstanding tool to extract essential information of atomic and molecular fragmentation processes. We reviewed three experiments, each pointing out specific strengths of the setup. The first experiment in Section 3.1, the XUV-pump IR-probe measurement in helium showed the capability of scanning the XUV energy of FLASH2 and the 3D momentum resolution of the REMI. The second experiment in Section 3.2 on the two-photon double ionization in argon revealed the necessity of a coincident measurement to sort out electrons stemming from specific channels. The third experiment in Section 3.3 on argon dimers showed, how to investigate dynamical processes like charge migration by means of delay-dependent KER analysis.

Besides XUV-XUV and XUV-IR experiments, future experiments aim for pump–probe experiments with the already commissioned HHG source in combination with the FEL. A future extension of the endstation is an XUV spectrometer that will be installed downstream of the REMI. The spectrometer allows to analyze FEL-pulses on a shot to shot basis, which can be used to sort REMI data according to the fluctuating SASE-generated pulses.

The REMI endstation at FLASH2 facilitates many collaborations with a large variety of experiments. Future proposals for experiments are already accepted and planned.

References

1. Strickland, D.; Mourou, G. Compression of amplified chirped optical pulses. *Opt. Commun.* **1985**, *55*, 447–449. [CrossRef]
2. Zewail, A.H. Laser Femtochemistry. *Science* **1988**, *242*, 1645–1653. [CrossRef] [PubMed]
3. Ullrich, J.; Rudenko, A.; Moshammer, R. Free-Electron Lasers: New Avenues in Molecular Physics and Photochemistry. *Annu. Rev. Phys. Chem.* **2012**, *63*, 635–660. [CrossRef] [PubMed]
4. Jiang, Y.H.; Senftleben, A.; Kurka, M.; Rudenko, A.; Foucar, L.; Herrwerth, O.; Kling, M.F.; Lezius, M.; Tilborg, J.V.; Belkacem, A.; et al. Ultrafast dynamics in acetylene clocked in a femtosecond XUV stopwatch. *J. Phys. B At. Mol. Opt. Phys.* **2013**, *46*, 164027. [CrossRef]
5. Schmid, G.; Schnorr, K.; Augustin, S.; Meister, S.; Lindenblatt, H.; Trost, F.; Liu, Y.; Miteva, T.; Gisselbrecht, M.; Düsterer, S.; et al. Tracing charge transfer in argon dimers by XUV-pump IR-probe experiments at FLASH. *J. Chem. Phys.* **2019**, *151*, 084314. [CrossRef]
6. Schnorr, K.; Senftleben, A.; Kurka, M.; Rudenko, A.; Schmid, G.; Pfeifer, T.; Meyer, K.; Kübel, M.; Kling, M.F.; Jiang, Y.H.; et al. Electron Rearrangement Dynamics in Dissociating I_2^{n+} Molecules Accessed by Extreme Ultraviolet Pump-Probe Experiments. *Phys. Rev. Lett.* **2014**, *113*, 073001. [CrossRef]
7. Jiang, Y.H.; Rudenko, A.; Herrwerth, O.; Foucar, L.; Kurka, M.; Kühnel, K.U.; Lezius, M.; Kling, M.F.; van Tilborg, J.; Belkacem, A.; et al. Ultrafast Extreme Ultraviolet Induced Isomerization of Acetylene Cations. *Phys. Rev. Lett.* **2010**, *105*, 263002. [CrossRef]
8. Orzechowski, T.J.; Anderson, B.; Fawley, W.M.; Prosnitz, D.; Scharlemann, E.T.; Yarema, S.; Hopkins, D.; Paul, A.C.; Sessler, A.M.; Wurtele, J. Microwave radiation from a high-gain free-electron laser amplifier. *Phys. Rev. Lett.* **1985**, *54*, 889–892. [CrossRef]

9. Emma, P.; Akre, R.; Arthur, J.; Bionta, R.; Bostedt, C.; Bozek, J.; Brachmann, A.; Bucksbaum, P.; Coffee, R.; Decker, F.J.; et al. First lasing and operation of an ångstrom-wavelength free-electron laser. *Nat. Photonics* **2010**, *4*, 641–647. [CrossRef]

10. Ackermann, W.A.; Asova, G.; Ayvazyan, V. Operation of a free-electron laser from the extreme ultraviolet to the water window. *Nat. Photonics* **2007**, *1*, 336–342. [CrossRef]

11. Brabec, T.; Krausz, F. Intense few-cycle laser fields: Frontiers of nonlinear optics. *Rev. Mod. Phys.* **2000**, *72*, 545–591. [CrossRef]

12. Cerullo, G.; Baltuška, A.; Mücke, O.; Vozzi, C. Few-optical-cycle light pulses with passive carrier-envelope phase stabilization. *Laser Photonics Rev.* **2011**, *5*, 323–351. [CrossRef]

13. Corkum, P.B. Plasma perspective on strong field multiphoton ionization. *Phys. Rev. Lett.* **1993**, *71*, 1994–1997. [CrossRef] [PubMed]

14. Lewenstein, M.; Balcou, P.; Ivanov, M.Y.; L'Huillier, A.; Corkum, P.B. Theory of high-harmonic generation by low-frequency laser fields. *Phys. Rev. A* **1994**, *49*, 2117–2132. [CrossRef]

15. McPherson, A.; Gibson, G.; Jara, H.; Johann, U.; Luk, T.S.; McIntyre, I.A.; Boyer, K.; Rhodes, C.K. Studies of multiphoton production of vacuum-ultraviolet radiation in the rare gases. *J. Opt. Soc. Am. B* **1987**, *4*, 595–601. [CrossRef]

16. Calegari, F.; Sansone, G.; Stagira, S.; Vozzi, C.; Nisoli, M. Advances in attosecond science. *J. Phys. B At. Mol. Opt. Phys.* **2016**, *49*, 062001. [CrossRef]

17. Vozzi, C.; Calegari, F.; Frassetto, F.; Poletto, L.; Sansone, G.; Villoresi, P.; Nisoli, M.; De Silvestri, S.; Stagira, S. Coherent continuum generation above 100 eV driven by an IR parametric source in a two-color scheme. *Phys. Rev. A* **2009**, *79*, 033842. [CrossRef]

18. Boutet, S.; Yabashi, M. X-Ray Free Electron Lasers and Their Applications. In *X-ray Free Electron Lasers: A Revolution in Structural Biology*; Springer International Publishing: Cham, Switzerland, 2018; pp. 1–21. [CrossRef]

19. Schmid, G.; Schnorr, K.; Augustin, S.; Meister, S.; Lindenblatt, H.; Trost, F.; Liu, Y.; Braune, M.; Treusch, R.; Schröter, C.D.; et al. Reaction microscope endstation at FLASH2. *J. Synchrotron Radiat.* **2019**, *26*, 854–867. [CrossRef]

20. Ayvazyan, V.; Baboi, N.; Bähr, J.; Balandin, V.; Beutner, B.; Brandt, A.; Bohnet, I.; Bolzmann, A.; Brinkmann, R.; Brovko, O.I.; et al. First operation of a free-electron laser generating GW power radiation at 32 nm wavelength. *Eur. Phys. J. D At. Mol. Opt. Plasma Phys.* **2006**, *37*, 297–303. [CrossRef]

21. Faatz, B.; Plönjes, E.; Ackermann, S.; Agababyan, A.; Asgekar, V.; Ayvazyan, V.; Baark, S.; Baboi, N.; Balandin, V.; von Bargen, N.; et al. Simultaneous operation of two soft X-ray free-electron lasers driven by one linear accelerator. *New J. Phys.* **2016**, *18*, 062002. [CrossRef]

22. Faatz, B.; Braune, M.; Hensler, O.; Honkavaara, K.; Kammering, R.; Kuhlmann, M.; Ploenjes, E.; Roensch-Schulenburg, J.; Schneidmiller, E.; Schreiber, S.; et al. The FLASH Facility: Advanced Options for FLASH2 and Future Perspectives. *Appl. Sci.* **2017**, *7*, 1114. [CrossRef]

23. Deutsches Elektronen-Synchrotron DESY. FLASH Parameters. Available online: https://photon-science.desy.de/facilities/flash/flash_parameters/index_eng.html (accessed on 9 March 2020).

24. Lang, T.; Alisauskas, S.; Große-Wortmann, U.; Hülsenbusch, T.; Manschwetus, B.; Mohr, C.; Müller, J.; Peters, F.; Schirmel, N.; Schulz, S.; et al. Versatile OPCPA Pump-Probe Laser System for the FLASH2 XUV FEL Beamline at DESY. In Proceedings of the 2019 Conference on Lasers and Electro-Optics Europe European Quantum Electronics Conference (CLEO/Europe-EQEC), Munich, Germany, 23–27 June 2019; p. 1. [CrossRef]

25. Appi, E.; Papadopoulou, C.; Mapa, J.; Wesavkar, N.; Jusko, C.; Mosel, P.; Alisauskas, S.; Lang, T.; Heyl, C.; Manschwetus, B.; et al. A synchronized VUV light source based on high-order harmonic generation at FLASH. *Sci. Rep.* **2020**, *10*, 6867. [CrossRef]

26. Heyl, C.M.; Arnold, C.L.; Couairon, A.; L'Huillier, A. Introduction to macroscopic power scaling principles for high-order harmonic generation. *J. Phys. B At. Mol. Opt. Phys.* **2016**, *50*, 013001. [CrossRef]

27. Ullrich, J.; Moshammer, R.; Dorn, A.; Dörner, R.; Schmidt, L.P.H.; Schmidt-Böcking, H. Recoil-ion and electron momentum spectroscopy: reaction-microscopes. *Rep. Prog. Phys.* **2003**, *66*, 1463–1545. [CrossRef]

28. Jagutzki, O.; Dangendorf, V.; Lauck, R.; Czasch, A.; Milnes, J. A position- and time-sensitive photon-counting detector with delay- line read-out. *Opt. Sens. Technol. Appl.* **2007**. [CrossRef]

29. Kurka, M.; Rudenko, A.; Foucar, L.; Kühnel, K.U.; Jiang, Y.H.; Ergler, T.; Havermeier, T.; Smolarski, M.; Schössler, S.; Cole, K.; et al. Two-photon double ionization of Ne by free-electron laser radiation: A kinematically complete experiment. *J. Phys. B At. Mol. Opt. Phys.* **2009**, *42*, 141002. [CrossRef]

30. Augustin, S.; Schulz, M.; Schmid, G.; Schnorr, K.; Gryzlova, E.V.; Lindenblatt, H.; Meister, S.; Liu, Y.F.; Trost, F.; Fechner, L.; et al. Signatures of autoionization in the angular electron distribution in two-photon double ionization of Ar. *Phys. Rev. A* **2018**, *98*, 033408. [CrossRef]

31. National Institute of Standards and Technology (NIST). NIST Atomic Spectra Database Levels Data. Available online: https://physics.nist.gov/cgi-bin/ASD/energy1.pl?encodedlist=XXT2&de=0&spectrum=He+I&submit=Retrieve+Data&units=1&format=0&output=0&page_size=15&multiplet_ordered=0&conf_out=on&term_out=on&level_out=on&unc_out=1&j_out=on&lande_out=on&perc_out=on&biblio=on&temp= (accessed on 16 April 2020).

32. Agostini, P.; Fabre, F.; Mainfray, G.; Petite, G.; Rahman, N.K. Free-Free Transitions Following Six-Photon Ionization of Xenon Atoms. *Phys. Rev. Lett.* **1979**, *42*, 1127. [CrossRef]

33. Corkum, P.B.; Burnett, N.H.; Brunel, F. Above-threshold ionization in the long-wavelength limit. *Phys. Rev. Lett.* **1989**, *62*, 1259–1262. [CrossRef]

34. Kerbstadt, S.; Pengel, D.; Johannmeyer, D.; Englert, L.; Bayer, T.; Wollenhaupt, M. Control of photoelectron momentum distributions by bichromatic polarization-shaped laser fields. *New J. Phys.* **2017**, *19*, 103017. [CrossRef]

35. Fechner, L.; Camus, N.; Ullrich, J.; Pfeifer, T.; Moshammer, R. Strong-Field Tunneling from a Coherent Superposition of Electronic States. *Phys. Rev. Lett.* **2014**, *112*, 213001. [CrossRef]

36. Fechner, L.; Camus, N.; Krupp, A.; Ullrich, J.; Pfeifer, T.; Moshammer, R. Creation and survival of autoionizing states in strong laser fields. *Phys. Rev. A* **2015**, *92*, 051403. [CrossRef]

37. Busto, D.; Vinbladh, J.; Zhong, S.; Isinger, M.; Nandi, S.; Maclot, S.; Johnsson, P.; Gisselbrecht, M.; L'Huillier, A.; Lindroth, E.; et al. Fano's Propensity Rule in Angle-Resolved Attosecond Pump-Probe Photoionization. *Phys. Rev. Lett.* **2019**, *123*, 133201. [CrossRef] [PubMed]

38. Braune, M.; Hartmann, G.; Ilchen, M.; Knie, A.; Lischke, T.; Reinköster, A.; Meissner, A.; Deinert, S.; Glaser, L.; Al-Dossary, O.; et al. Electron angular distributions of noble gases in sequential two-photon double ionization. *J. Mod. Opt.* **2016**, *63*, 324–333. [CrossRef]

39. Grum-Grzhimailo, A.N.; Gryzlova, E.V.; Strakhova, S.I.; Kabachnik, N.M.; Fritzsche, S. Angular distributions and correlations in sequential two-photon atomic double ionization. *J. Phys. Conf. Ser.* **2009**, *194*, 012004. [CrossRef]

40. Redlin, H.; Al-Shemmary, A.; Azima, A.; Stojanovic, N.; Tavella, F.; Will, I.; Düsterer, S. The FLASH pump–probe laser system: Setup, characterization and optical beamlines. *Nucl. Instrum. Methods Phys. Res. Sect. A Accel. Spectrom. Detect. Assoc. Equip.* **2011**, *635*, S88–S93. [CrossRef]

4.3 Laser-dressing effects in helium

In this paper we employ XUV radiation of the FLASH2 and IR laser radiation in a pump-probe scheme. Our target is atomic helium and XUV photon energies are kept below the ionization potential. The interplay of both radiation fields allows to excite a variety of states which are not accessible by single-photon absorption or in a single-color scheme. Photoelectrons which are emitted from the excited helium atoms are analyzed to deduce excitation pathways.

Besides the assignment of excited states we investigate their laser intensity dependence. Due to the new undulator technique of FLASH2 (cf. Chapter 3), we were able to scan the XUV photon energy fine enough to track intensity dependent shifts of excited states. The scheme also allowed us determine intensity thresholds were higher order excitation pathways open up.

Similar measurements were performed with HHG-based XUV radiation in a transient absorption (TA) scheme [72, 73, 74]. They report on excited states which are only accessible due to the IR laser-dressing of the helium atom. These multi-color multi-photon excited states were referred to as light induced states (LIS) [75]. Our measurement can be seen as a complementary investigation compared to the TA measurements. While we measure photoelectrons, TA measurements analyze the absorption spectrum of a broadband XUV pulse from a gas sample.

There are comparable photoelectron measurements in helium employing XUV radiation (synchrotron, FEL, HHG) below the ionization threshold in combination with IR radiation [76, 77, 36]. These measurements however are not dealing with multi-color multi-photon excitation, so their relevance is limited.

Photoelectron spectroscopy of laser-dressed atomic helium

Severin Meister [⊙],[1,*] Aaron Bondy,[2,3] Kirsten Schnorr,[4] Sven Augustin,[4] Hannes Lindenblatt [⊙],[1] Florian Trost [⊙],[1]
Xinhua Xie,[4] Markus Braune [⊙],[5] Rolf Treusch [⊙],[5] Bastian Manschwetus,[5] Nora Schirmel,[5] Harald Redlin,[5] Nicolas Douguet,[6]
Thomas Pfeifer,[1] Klaus Bartschat [⊙],[2] and Robert Moshammer[1]

[1]*Max-Planck-Institute for Nuclear Physics, 69117 Heidelberg, Germany*
[2]*Department of Physics and Astronomy, Drake University, Des Moines, Iowa 50311, USA*
[3]*Department of Physics, University of Windsor, Windsor, Ontario N9B 3P4, Canada*
[4]*Paul Scherrer Institute, 5232 Villigen, Switzerland*
[5]*Deutsches Elektronen-Synchrotron, 22607 Hamburg, Germany*
[6]*Department of Physics, Kennesaw State University, Marietta, Georgia 30060, USA*

Photoelectron emission from excited states of laser-dressed atomic helium is analyzed with respect to laser intensity-dependent excitation energy shifts and angular distributions. In the two-color extreme ultraviolet (XUV)-infrared (IR) measurement, the XUV photon energy is scanned between 20.4 eV and the ionization threshold at 24.6 eV, revealing electric dipole-forbidden transitions for a temporally overlapping IR pulse ($\approx 10^{12}\,\mathrm{W\,cm^{-2}}$). The interpretation of the experimental results is supported by numerically solving the time-dependent Schrödinger equation in a single-active-electron approximation.

DOI: 10.1103/PhysRevA.102.062809

I. INTRODUCTION

Photoelectron spectroscopy is a powerful technique to obtain compositional and structural information about matter and to investigate light-matter interactions in general. It has been successfully employed and continuously developed over many decades in atomic and molecular physics [1]. Photoelectrons carry information about the electronic bound and continuum states of the corresponding atom, as well as information about the absorbed and emitted photons.

With the advent of intense optical lasers, multiphoton absorption in atoms and molecules became feasible, enabling the observation of a variety of new phenomena, e.g., multiphoton excitation microscopy [2], resonance-enhanced multiphoton ionization (REMPI) [3], Doppler-free two-photon spectroscopy [4,5], and high-order harmonic generation (HHG) [6,7], to name just a few. One step further in the investigation of light-matter interactions is the implementation of two-color ionization and excitation schemes, which reveal laser-induced continuum structures [8] and light-induced structures (LIS) [9]. In the former case, the dressing laser field couples bound states to the continuum, giving rise to a resonant structure [10–13]. In the latter case, the ground state is coupled to

excited states beyond the one-photon allowed dipole transition via two-color photoexcitation [14–17].

In this paper, we report the use of XUV (extreme ultraviolet) radiation with tunable wavelength provided by the free-electron laser in Hamburg (FLASH) in combination with a synchronized infrared (IR) laser to obtain a detailed picture of excited states in laser-dressed atomic helium. The extreme ultraviolet (XUV) photon energy is scanned over the $1snp\,^1P$ Rydberg excitation series to a value just below the ionization threshold. The superimposed IR pulses (800 nm wavelength) arrive with a freely adjustable time delay with respect to the excitation pulses. Their intensity is too low to ionize He in its ground state, but strong enough to ionize it from excited states that are temporarily reached via a combination of XUV and IR photons. The ionization yield and angular distributions are analyzed as a function of the XUV photon energy, the IR time delay, and the IR intensity. In the case of temporally overlapping pulses, by absorption of one XUV and one or more IR photons, one electron is lifted from the ground into a continuum state through laser-dressed excited states, including those that are not accessible by pure single-photon excitation. The interpretation of the experimental results is supported by numerical calculations based on the time-dependent Schrödinger equation (TDSE) within the single-active electron (SAE) approximation.

This two-color scheme has the clear advantage over, e.g., single-color REMPI setups, where the dominant contribution to the excitation energy is delivered by only one XUV photon, and hence the laser intensity can be kept low. Therefore, field-induced changes to energy levels and fragmentation are minimized. This opens up precision-spectroscopic studies of atoms and molecules under less-perturbing conditions.

---

*severin.meister@mpi-hd.mpg.de

There are photoionization measurements employing HHG-based XUV radiation in combination with IR laser radiation [18–20]. However, these experiments rely on single-photon excitation of $1snp$ ^1P states and the following ionization through IR photon absorption. In contrast, the presented measurement focuses on multiphoton excitation, enabled by the combined interaction of XUV and IR photons.

II. EXPERIMENTAL AND THEORETICAL METHODS

The experiment was carried out with the reaction microscope (REMI) end station [21,22] at the free-electron laser (FEL) FLASH2 [23,24]. FLASH2 features variable-gap undulators that allow us to quickly change the photon wavelength [25] over a broad spectral range. During the measurements, the XUV photon energy was scanned in steps of 0.2 eV from 20.4 eV to just below the ionization threshold of atomic helium at 24.6 eV [26]. The FEL pulse-length was about 40 fs full-width at half maximum (FWHM) in intensity, and the pulse energy (< 10 nJ) was reduced to a level such that two-XUV-photon absorption in He can be neglected. Synchronized, but with a timing jitter of several ten femtoseconds, the IR probe laser (800 nm) was superimposed collinearly with the XUV beam. In order to ensure optimal temporal overlap with the FEL pulses, an IR pulse-duration of about 90 fs FWHM was chosen. The IR pulse energy and the focusing conditions were adjusted such that intensities in the order of up to 10^{13} W cm^{-2} were reached in the target. With a diameter of about 30 μm, the focus of the IR beam was significantly wider than the FEL focus ($\approx$10 μm). XUV and IR radiation were linearly polarized and aligned parallel to each other. Both beams were focused onto a dilute supersonic gas jet of atomic helium in the center of the REMI, which is equipped with two time- and position-sensitive detectors [27] to collect all charged fragments (electrons and ions) within the full 4π solid angle. Time-of-flight and position information is used to retrieve the particles' momentum vectors at the time of ionization.

During the XUV photon-energy scans, the FEL pulse energy and the FEL beam diameter change slightly. Together with the energy-dependent absorber-foil transmissions and mirror reflectivities, this leads to small variations in the photon flux. In our analysis, these effects are corrected by normalizing the data for each XUV energy with the simultaneously recorded yield of H$_2^+$ ions, which stem from a constant and weak background of H$_2$ gas in the REMI chamber. The ionization cross section of H$_2$ was taken from Ref. [28].

In the experiment, two sets of data were taken, one with an IR intensity of approximately $I_{\text{high}} \approx 8 \times 10^{12}$ W cm^{-2} and one with $I_{\text{low}} \approx 1 \times 10^{12}$ W cm^{-2}. We note that the temporal jitter between FEL and IR, which is comparable to the IR pulse duration, leads effectively to a lowering of the average IR intensity for the case of overlapping pulses. The influence of this imperfect overlap of both pulses increases with the IR intensity in the same way as the contribution of nonlinear multiphoton transitions increases. Therefore, in the comparison to theory, a smaller difference in intensity between the low and high IR intensity case was chosen in our calculations in order to mimic the corresponding experimental conditions.

The theoretical part of this study is based on numerically solving the TDSE in the SAE approximation. Electrons are assumed to be noninteracting, while the ground state is effectively described as a $1s1s'$ ^1S state, where the $1s$ is close to the He$^+$ orbital and the $1s'$ is treated like a valence orbital. As always in theory, the binding energies of the $n\ell$ valence electrons are not exact. While $1sn\ell$ Rydberg states with angular momenta $\ell \geqslant 2$ have very accurate binding energies, this is not quite the case for p electrons and particularly for s electrons, due to the small or missing centrifugal barrier. Since excitation energies are measured from the ground state, much of the remaining discrepancies are due to the binding energy of the $1s'$ orbital.

Specifically, we used the same one-electron potential as Birk *et al.* [29],

$$V(r) = -\frac{1}{r} - \left(\frac{1}{r} + 1.3313\right) \exp(-3.0634\,r), \quad (1)$$

where r is the distance from the nucleus, to calculate the valence orbitals. The difference of excitation energies compared to the recommended excitation from the NIST database [26] is less than 0.2 eV even in the worst-case scenario and does not alter the essential conclusions presented below. We will sometimes omit the inner $1s$ electron to simplify the notation, keeping in mind that only two-electron singlet spin states are accessible, since spin-forbidden transitions are negligible.

The laser parameters were chosen according to the available knowledge regarding the actual experimental conditions. The XUV pulse duration was taken as 40 fs (FWHM value of a peak intensity of 1×10^{12} W/cm^2 with a Gaussian envelope) and the IR pulse duration as 80 fs. While the XUV photon energy was varied over a range in steps of 0.05 eV, the central IR photon energy was held fixed at 1.55 eV (800 nm). Since both beams are linearly polarized along the same direction, the initial state can be propagated very efficiently and accurately. Specifically, we used an updated version of the code described by Douguet *et al.* [30].

III. RESULTS

Over the XUV scanning range, the helium atom can be excited from the $1s^2$ ^1S ground state to a $1snp$ ^1P excited state for specific XUV photon energies, according to the electric-dipole selection rules. The excited atom can be ionized by absorbing one or more IR photons ($\hbar\omega = 1.55$ eV) of a subsequent laser pulse, promoting the weakly bound electron into the continuum. This mechanism is depicted in an energy-level scheme in the upper part of Fig. 1.

Experimental data for the corresponding process are shown in Fig. 2, where the yield of photoelectrons is plotted against the XUV photon energy for a nonoverlapping temporally delayed IR pulse with intensity I_{high}. Clearly visible are the yield enhancements for XUV energies that match the $1snp$ ^1P excitation energies in helium ($2p$ at 21.2 eV, $3p$ at 23.1 eV, $4p$ at 23.7 eV, etc. [26]). Also shown in Fig. 2 is the photoelectron yield for XUV and IR pulses in temporal overlap (yellow distribution). Compared to delayed ionization, the ^1P-excitation peaks remain while an additional maximum appears around 22.4 eV. This feature was observed and described in transient-absorption measurements as a LIS [9,15,16,31]. As XUV
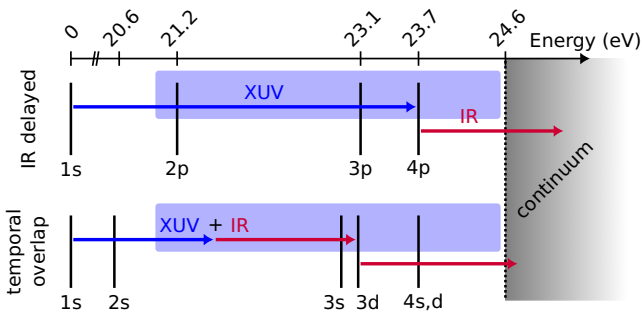
FIG. 1. Electronic energy level scheme of helium with different ionization pathways through intermediate excited states. The XUV energy scanning range is indicated by the blue box.

and IR radiation are simultaneously present, the helium atom can undergo dipole-forbidden (for single photons) transitions, provided the XUV photon absorption is accompanied by the absorption or emission of IR photons of the dressing laser field. In the simplest and dominant case, one XUV photon and one IR photon combined drive $1s^2 \rightarrow 1sns$ or $1s^2 \rightarrow 1snd$ transitions. By absorbing additional IR photons, the excited atom is ionized.

This mechanism is depicted in the lower part of Fig. 1. Direct two-photon absorption couples the ground state to $1sns$ and $1snd$ states. In contrast to P-state ionization, peaks of LIS emerge at XUV energies matching the energy of the excited state plus or minus one IR photon.

In Fig. 3, the measured yield distributions for overlapping pulses are shown for the two cases of low and high IR intensity. The purple distribution in the background is recorded with I_{low}, while the yellow distribution is again for the significantly larger intensity I_{high}. The latter exhibits a gradual decrease in the yield from the peak corresponding to the $2p$ state at 21.2 eV over the $3p$ state at 23.2 eV up to

the higher np states (not visible due to the resolution). This overall decrease with rising XUV energy can be explained by the energy dependence of the cross section for the excitation step [32]. The excitation probabilities are directly mapped to the ionization yield in the case of I_{high}, where the IR intensity is large enough to ionize all excited states independent of the number of photons (N) needed. For low IR intensity (purple distribution in Fig. 3), on the other hand, the scaling law $R \sim I^N$ of the transition rate R with the laser intensity I in multiphoton processes becomes relevant [33]. Therefore, the ionization yield of the $2p$ state, which requires $N = 3$ IR photons, is reduced compared to the yield from the $3p$ and higher np states ($N = 1$).

Two approaches are employed to assign the LIS to specific field-free atomic excited states. First, we analyze the calculated distributions for excitation in combination with ionization and compare them with the experimental ionization yield. Second, the inspection of the measured photoelectron angular distribution allows us to deduce the intermediate bound state that the electron was emitted from.

Figure 4 shows theoretical predictions for XUV and IR pulses in temporal overlap. The calculated ionization probability is plotted against the XUV photon energy for two different IR intensities, color coded in yellow and purple for high and low IR intensity, respectively (similar to the measurement shown in Fig. 3). In addition to the ionization yield, our calculations predict the population distribution of excited atomic states at the end of the pulses as a function of the XUV energy and the IR intensity. The most prominently populated states in the theoretical excitation-probability distributions are marked by arrows in Fig. 4. They serve as an indicator of the role of the respective excited states and their population (either direct or light-induced) at a given XUV energy en route to ionization. This allows assignment of the peaks in the ionization probability distribution (bottom panel of Fig. 4) to the excited states from which the atom is ionized.
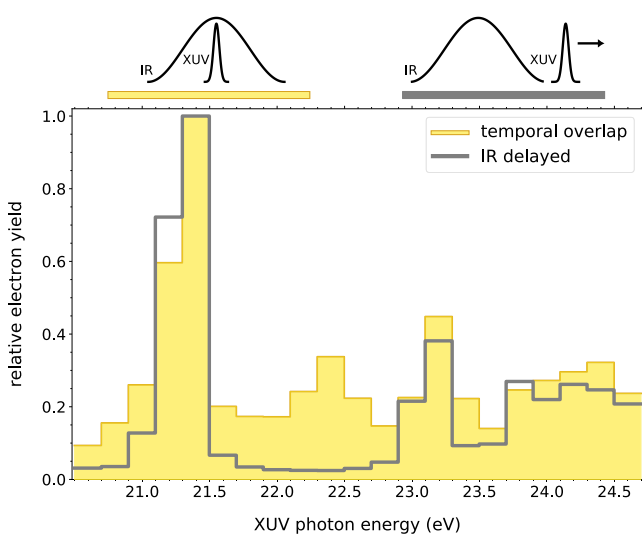
FIG. 2. Photoelectron yield measured for two different delays between the XUV and IR pulses. Both curves are normalized to their maximum yield, and statistical error bars are much smaller than the line thickness.
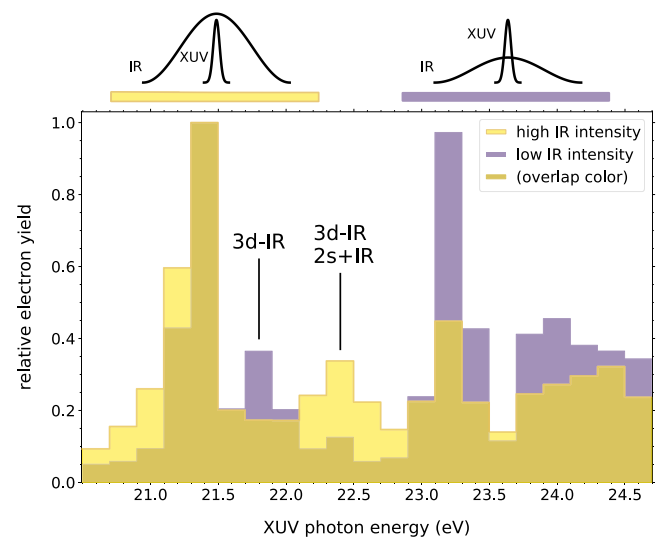
FIG. 3. Photoelectron yield measured for temporally overlapping XUV and IR pulses. The distribution for high IR intensities (I_{high}) is shown in yellow (light gray), and the distribution for low IR intensities (I_{low}) in purple (dark).
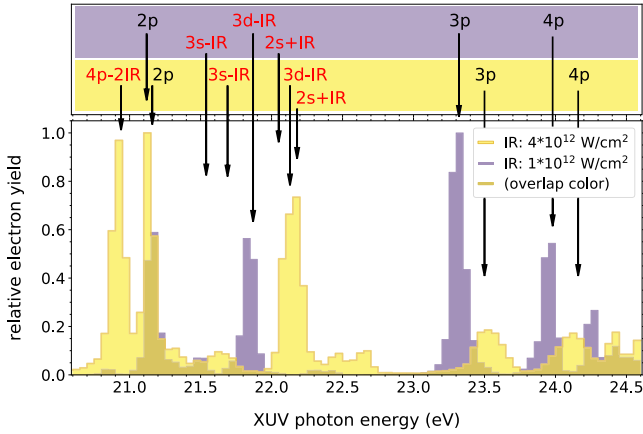
FIG. 4. Calculated ionization probability for two different IR intensities. Arrows in the top panel indicate the calculated positions of excited (black) and light-induced (red) states. + (−) IR denotes the emission (absorption) of an IR photon.

FIG. 5. PAD for the dominant LIS at high IR intensity. (Exp: E_{XUV} from 22.2 to 22.5 eV and E_e from 0.2 to 0.5 eV, Calc: E_{XUV} from 22 to 22.3 eV and E_e from 0.2 to 0.5 eV). The experimental counts are normalized to theory. The inset shows the corresponding measured 3D photoelectron momentum distribution.

Electronic energy levels experience an AC Stark shift due to the IR laser field [34,35]. This shift is clearly seen for the $3p$ state in theory (see Fig. 4), but is much smaller in the experiment (see Fig. 3). However, experimental Stark shifts can be seen in the photoelectron kinetic energy spectrum (not shown here). Overall, we see good agreement between experiment and theory when comparing the purple distributions in Figs. 3 and 4. Similar to the experiment, the calculated ionization yield shows a reduced contribution of the $2p$ state relative to the $3p$ state when the IR intensity is lowered. Moreover, the strengths and the positions of the LIS peaks, which only appear in temporal overlap, are well reproduced by the calculations. Small shifts in energy are attributed to the already mentioned inherent inaccuracies of electronic binding energies in the SAE model. Most importantly, for low IR intensity the dominating LIS peak is found around 21.8 eV as in the experimental counterpart. As the enhancements by other excited states appear at distinctively different positions and are much less pronounced, this dominating LIS peak at 21.8 eV (purple distribution in Fig. 3) can be assigned to the $3d$ state.

The situation changes for high IR intensity where the dominant LIS peak is shifted to a larger XUV energy of about 22.4 eV in experiment (yellow in Fig. 3). Comparison with theory indicates that in this case ionization proceeds through the Stark-shifted $3d$ and $2s$ excited states. Both contribute to the dominating LIS peak at about 22.2 eV according to our state assignment in Fig. 4. Relative to the $3d$ state, the $2s$ contribution becomes more relevant at high intensity because, in order to populate the $2s$ state, the atom absorbs one XUV photon while emitting one IR photon. Ionization takes place by absorbing another three IR photons. In contrast to this effective four IR-photon transition, ionization via the $3d$ state involves only two IR photons. We note that the large shift of the $3d$ LIS with IR intensity seen in the experiment is also consistent with the calculation by Chen *et al.* [9].

The electronic structure of the dominant LIS involving both the $2s$ and $3d$ excited states at 22.4 eV for high IR intensity in Fig. 3 can also be deduced from the photoelectron
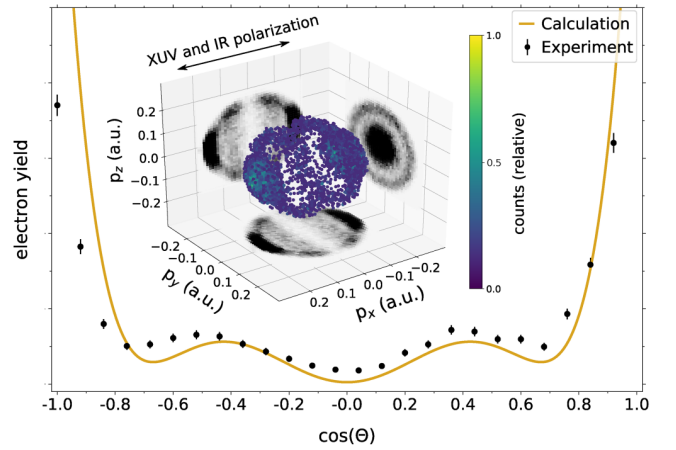
angular distribution (PAD). This is shown in Fig. 5 where the yield of electrons is plotted as a function of their emission angle Θ with respect to the laser polarization axis.

The distribution exhibits a typical "F-like" shape, indicating the angular quantum number of the continuum state to be $L = 3$. Starting from a ^1S state ($L = 0$), an angular quantum number of $L = 3$ can only be reached by absorbing at least three photons. For an atom in a ^1D state ($L = 2$), absorbing one IR photon is sufficient to obtain an F-like PAD. One can deduce the populated bound states by taking the photoelectron kinetic energy (0.4 eV) minus the IR photon energies (each 1.55 eV) while also accounting for the Stark-shifted continuum level. One finds that the matching states are the $3d$ and $2s$ excited states. The yellow solid line in Fig. 5 shows the calculated PAD for the considered LIS. We find very good agreement between experiment and theory, thereby supporting our interpretation of the mechanism.

The three-dimensional PAD of the dominant LIS is also contained in the measured three-dimensional photoelectron momentum distribution, shown in the inset of Fig. 5. Dots in the plot represent a bin in momentum space, with the yield within each bin being color coded. The energy range was chosen from 0.3 to 0.5 eV, resulting in a spherical shell of dots in the plot. The projections on the walls show the integrated yield along one specific direction. The two small maxima in Fig. 5 are found as two rings around the polarization axis, while the large maxima are found in the three-dimensional distribution for maximal absolute p_x momentum, i.e., along the polarization axis of IR and XUV.

IV. CONCLUSION

We have measured and analyzed photoelectrons stemming from laser-dressed atomic helium. The helium atoms were photo-excited over a large energy range by XUV FEL radiation in the presence of a moderately strong IR laser ($\approx 10^{12}$ W cm^{-2}). The scheme allowed us to reveal light-induced

structures alongside the ^1P Rydberg series. The observed excitation energies of the LIS for varying IR intensities were supported by TDSE calculations. The photoelectron angular distribution and the kinetic energy were used to assign the LIS. The dominant LIS in the photoelectron yield of laser-dressed helium was identified as stemming from the $1s3d\ ^1D$ excited state for an IR intensity of about $1 \times 10^{12}\ \mathrm{W\,cm^{-2}}$, while for a higher IR intensity of about $4 \times 10^{12}\ \mathrm{W\,cm^{-2}}$ the $1s2s\ ^1S$ state also contributes significantly.

Our investigation complements previous transient-absorption measurements on light-induced structures but brings up additional aspects. While transient-absorption measurements reveal LIS in the absorption spectrum without the need for ionization, our measurement is sensitive to the excited states from which electrons are emitted and allows us to measure and assign angular distributions of the corresponding continuum final states.

The presented analysis suggests the preference to populate the $1s3d\ ^1D$ state rather than the $1s3s\ ^1S$ state. This is can be seen in the high IR intensity case, where all excited states get ionized, so the yield is independent of the number of ionizing photons. We find the propensity of helium in its ground state to increase angular momentum by two-photon absorption, thus driving a bound-bound transition. This can be understood in the context of Fano's propensity rule [36], originally stated between bound and continuum states, and the propensity analysis of continuum-continuum transitions by Busto *et al.* [37], both stating the propensity to increase the angular momentum in photoabsorption.

[1] E. O. Lawrence and M. A. Chaffee, On the direction of emission of photoelectrons from potassium vapor by ultraviolet light, Phys. Rev. **36**, 1099 (1930).

[2] A. Diaspro, P. Bianchini, G. Vicidomini, M. Faretta, P. Ramoino, and C. Usai, Multi-photon excitation microscopy, BioMed. Eng. OnLine **5**, 36 (2006).

[3] T. Streibel and R. Zimmermann, Resonance-enhanced multi-photon ionization mass spectrometry (REMPI-MS): Applications for process analysis, Annu. Rev. Anal. Chem. **7**, 361 (2014).

[4] L. S. Vasilenko, V. P. Chebotaev, and A. V. Shishaev, Line shape of two-photon absorption in a standing-wave field in a gas, ZhETF Pis. Red. **12**, 161 (1970) [JETP Lett. **12**, 113 (1970)].

[5] C. Wieman and T. W. Hänsch, Doppler-Free Laser Polarization Spectroscopy, Phys. Rev. Lett. **36**, 1170 (1976).

[6] P. B. Corkum, Plasma Perspective on Strong Field Multiphoton Ionization, Phys. Rev. Lett. **71**, 1994 (1993).

[7] M. Lewenstein, P. Balcou, M. Y. Ivanov, A. L'Huillier, and P. B. Corkum, Theory of high-harmonic generation by low-frequency laser fields, Phys. Rev. A **49**, 2117 (1994).

[8] Y. Heller, V. Lukinykh, A. Popov, and V. Slabko, Experimental evidence for a laser-induced autoionizing-like resonance in the continuum, Phys. Lett. A **82**, 4 (1981).

[9] S. Chen, M. J. Bell, A. R. Beck, H. Mashiko, M. Wu, A. N. Pfeiffer, M. B. Gaarde, D. M. Neumark, S. R. Leone, and K. J. Schafer, Light-induced states in attosecond transient absorption spectra of laser-dressed helium, Phys. Rev. A **86**, 063408 (2012).

[10] P. Knight, M. Lauder, and B. Dalton, Laser-induced continuum structure, Phys. Rep. **190**, 1 (1990).

[11] P. Coleman, P. Knight, and K. Burnett, Laser-induced continuum structure in multiphoton ionisation, Opt. Commun. **42**, 171 (1982).

[12] Y. Heller and A. Popov, Parametric generation and absorption of tunable vacuum-ultraviolet radiation controlled by laser-induced autoionizing-like resonances in the continuum, Opt. Commun. **18**, 449 (1976).

[13] L. Armstrong, B. L. Beers, and S. Feneuille, Resonant multi-photon ionization via the fano autoionization formalism, Phys. Rev. A **12**, 1903 (1975).

[14] M. Chini, X. Wang, Y. Cheng, Y. Wu, D. Zhao, D. A. Telnov, S.-I. Chu, and Z. Chang, Sub-cycle oscillations in virtual states brought to light, Sci. Rep. **3**, 1105 (2013).

[15] M. Reduzzi, J. Hummert, A. Dubrouil, F. Calegari, M. Nisoli, F. Frassetto, L. Poletto, S. Chen, M. Wu, M. B. Gaarde, K. Schafer, and G. Sansone, Polarization control of absorption of virtual dressed states in helium, Phys. Rev. A **92**, 033408 (2015).

[16] J. E. Bækhøj and L. B. Madsen, Light-induced structures in attosecond transient-absorption spectroscopy of molecules, Phys. Rev. A **92**, 023407 (2015).

[17] M. J. Bell, A. R. Beck, H. Mashiko, D. M. Neumark, and S. R. Leone, Intensity dependence of light-induced states in transient absorption of laser-dressed helium measured with isolated attosecond pulses, J. Mod. Opt. **60**, 1506 (2013).

[18] P. Ranitovic, X. M. Tong, B. Gramkow, S. De, B. DePaola, K. P. Singh, W. Cao, M. Magrakvelidze, D. Ray, I. Bocharova, H. Mashiko, A. Sandhu, E. Gagnon, M. M. Murnane, H. Kapteyn, I. Litvinyuk, and C. L. Cocke, IR-assisted ionization of helium by attosecond extreme ultraviolet radiation, New J. Phys. **12**, 013008 (2010).

[19] N. Mayer, P. Peng, D. M. Villeneuve, S. Patchkovskii, M. Ivanov, O. Kornilov, M. J. J. Vrakking, and H. Niikura, Population transfer to high angular momentum states in infrared-assisted XUV photoionization of helium, J. Phys. B: At., Mol. Opt. Phys. **53**, 164003 (2020).

[20] L. H. Haber, B. Doughty, and S. R. Leone, Continuum phase shifts and partial cross sections for photoionization from excited states of atomic helium measured by high-order harmonic optical pump-probe velocity map imaging, Phys. Rev. A **79**, 031401(R) (2009).

[21] S. Meister, H. Lindenblatt, F. Trost, K. Schnorr, S. Augustin, M. Braune, R. Treusch, T. Pfeifer, and R. Moshammer, Atomic, molecular and cluster science with the reaction microscope endstation at FLASH2, Appl. Sci. **10**, 2953 (2020).

[22] G. Schmid, K. Schnorr, S. Augustin, S. Meister, H. Lindenblatt, F. Trost, Y. Liu, M. Braune, R. Treusch, C. D. Schröter, T. Pfeifer, and R. Moshammer, Reaction microscope endstation at FLASH2, J. Synchrotron Radiat. **26**, 854 (2019).

[23] B. Faatz, E. Plönjes, S. Ackermann, A. Agababyan, V. Asgekar, V. Ayvazyan, S. Baark, N. Baboi, V. Balandin, N. von Bargen, Y. Bican, O. Bilani, J. Bödewadt, M. Böhnert, R. Böspflug, S. Bonfigt, H. Bolz, F. Borges, O. Borkenhagen, M. Brachmanski *et al.*, Simultaneous operation of two soft x-ray free-electron lasers driven by one linear accelerator, New J. Phys. **18**, 062002 (2016).

[24] W. Ackermann, G. Asova, V. Ayvazyan, A. Azima, N. Baboi, J. Bähr, V. Balandin, B. Beutner, A. Brandt, A. Bolzmann, R. Brinkmann, O. I. Brovko, M. Castellano, P. Castro *et al.*, Operation of a free-electron laser from the extreme ultraviolet to the water window, Nat. Photon. **1**, 336 (2007).

[25] B. Faatz, M. Braune, O. Hensler, K. Honkavaara, R. Kammering, M. Kuhlmann, E. Plönjes, J. Roensch-Schulenburg, E. Schneidmiller, S. Schreiber *et al.*, The FLASH facility: Advanced options for FLASH2 and future perspectives, Appl. Sci. **7**, 1114 (2017).

[26] A. Kramida, Yu. Ralchenko, J. Reader, and NIST ASD Team, *NIST Atomic Spectra Database* (National Institute of Standards and Technology, Gaithersburg, MD, 2020, https://physics.nist.gov/asd.

[27] J. Ullrich, R. Moshammer, A. Dorn, R. Dörner, L. P. H. Schmidt, and H. Schmidt-Böcking, Recoil-ion and electron momentum spectroscopy: Reaction microscopes, Rep. Prog. Phys. **66**, 1463 (2003).

[28] J. A. R. Samson and G. N. Haddad, Total photoabsorption cross sections of H_2 from 18 to 113 eV, J. Opt. Soc. Am. B **11**, 277 (1994).

[29] P. Birk, V. Stooß, M. Hartmann, G. D. Borisova, A. Blättermann, T. Heldt, K. Bartschat, C. Ott, and T. Pfeifer, Attosecond transient absorption of a continuum threshold, J. Phys. B: At., Mol. Opt. Phys. **53**, 124002 (2020).

[30] N. Douguet, A. N. Grum-Grzhimailo, E. V. Gryzlova, E. I. Staroselskaya, J. Venzke, and K. Bartschat, Photoelectron angular distributions in bichromatic atomic ionization induced by circularly polarized VUV femtosecond pulses, Phys. Rev. A **93**, 033402 (2016).

[31] M. B. Gaarde, C. Buth, J. L. Tate, and K. J. Schafer, Transient absorption and reshaping of ultrafast XUV light by laser-dressed helium, Phys. Rev. A **83**, 013419 (2011).

[32] W. L. Wiese and J. R. Fuhr, Accurate atomic transition probabilities for hydrogen, helium, and lithium, J. Phys. Chem. Ref. Data **38**, 565 (2009).

[33] I. V. Hertel and C.-P. Schulz, *Atome, Moleküle und optische Physik 1* (Springer, Berlin, 2017), p. 289.

[34] A. M. Bonch-Bruevich, N. N. Kostin, V. A. Khodovoi, and V. V. Khromov, Changes in the atomic absorption spectrum in the field of a light wave, Sov. Phys. JETP **29**, 144 (1969).

[35] N. B. Delone and V. P. Krainov, AC Stark shift of atomic energy levels, Phys. Usp. **42**, 669 (1999).

[36] U. Fano, Propensity rules: An analytical approach, Phys. Rev. A **32**, 617 (1985).

[37] D. Busto, J. Vinbladh, S. Zhong, M. Isinger, S. Nandi, S. Maclot, P. Johnsson, M. Gisselbrecht, A. L'Huillier, E. Lindroth, and J. M. Dahlström, Fano's Propensity Rule in Angle-Resolved Attosecond Pump-Probe Photoionization, Phys. Rev. Lett. **123**, 133201 (2019).

Correction: The fourth affiliation contained an error and has been fixed.

4.4 Dichroism in laser-dressed helium

This paper is a follow-up of the previous one. Here we investigate the multicolor excited states in dependence of the relative polarization of XUV and IR. Both radiation fields are linearly polarized and can be rotated with respect towards each other. This gives an additional degree of freedom compared to a single-color experiment. We find certain states which can only be populated for a specific orientation of polarizations. Consequently, along with the population ionization vanishes. In this way, polarization can be used as a handle to switch on and off ionization at specific XUV photon energies.

Furthermore, additional states are identified and assigned compared to the investigation in the previous section. The analysis of photoelectron angular distributions (PADs) shows states with magnetic quantum numbers m differing from the ground-state value $m = 0$. This situation is found for orthogonal polarization between XUV and IR polarization.

Finally the paper discusses the laser intensity dependence of PADs. In our scheme the XUV photon provides the main energy contribution for ionization. In this way, helium can be ionized with just a few IR photons, in contrast to IR laser ionization only. This allows to enter a region between multi-photon ionization and tunnel ionization.

Regular Article – Ultraintense and Ultrashort Laser Fields

Linear dichroism in few-photon ionization of laser-dressed helium

Severin Meister[1,a], Aaron Bondy[2,3], Kirsten Schnorr[4], Sven Augustin[4], Hannes Lindenblatt[1], Florian Trost[1], Xinhua Xie[4], Markus Braune[5], Bastian Manschwetus[5], Nora Schirmel[5], Harald Redlin[5], Nicolas Douguet[6], Thomas Pfeifer[1], Klaus Bartschat[2], and Robert Moshammer[1]

[1] Max-Planck-Institute for Nuclear Physics, 69117 Heidelberg, Germany
[2] Department of Physics and Astronomy, Drake University, Des Moines, IA 50311, USA
[3] Department of Physics, University of Windsor, Windsor, ON N9B 3P4, Canada
[4] Paul Scherrer Institute, 5232 Villigen, Switzerland
[5] Deutsches Elektronen-Synchrotron, 22607 Hamburg, Germany
[6] Department of Physics, Kennesaw State University, Marietta, GA 30060, USA

Abstract. Ionization of laser-dressed atomic helium is investigated with focus on photoelectron angular distributions stemming from two-color multi-photon excited states. The experiment combines extreme ultraviolet (XUV) with infrared (IR) radiation, while the relative polarization and the temporal delay between the pulses can be varied. By means of an XUV photon energy scan over several electronvolts, we get access to excited states in the dressed atom exhibiting various binding energies, angular momenta, and magnetic quantum numbers. Furthermore, varying the relative polarization is employed as a handle to switch on and off the population of certain states that are only accessible by two-photon excitation. In this way, photoemission can be suppressed for specific XUV photon energies. Additionally, we investigate the dependence of the photoelectron angular distributions on the IR laser intensity. At our higher IR intensities, we start leaving the simple multi-photon ionization regime. The interpretation of the experimental results is supported by numerically solving the time-dependent Schrödinger equation in a single-active-electron approximation.

1 Introduction

The fundamental interaction of photons and matter is omnipresent in nature. Scientists not only employ light to investigate matter to high precision, but also as a tool to modify it in a well-controlled manner. The continuous development and optimization of light sources and combining them in a variety of ways makes it possible to enter unprecedented realms in light–matter interaction. For example, intense infrared (IR) pulses focused into a gas target can trigger high-harmonic generation of extreme ultraviolet (XUV) photons [1,2]. The two intrinsically synchronized radiation fields can be used in a variety of experiments on atoms and molecules. The scheme of XUV excitation and subsequent IR ionization is employed in photoelectron measurements to determine angular-distribution parameters, relative population strengths, and delay-dependent ionization yields [3–6]. Complementary transient absorption measurements employed an energetically broad XUV spectrum in combination with the IR driving laser and revealed light-induced states (LIS) in helium [7]. These LIS can be attributed to two-color multiphoton excitation, allowing transitions beyond the one-photon electric-dipole selection rules. LIS were investigated in the context of transient absorption (see [8] for a review) with regard to their intensity dependence [9], quantum interference [10,11], and also for molecules [12]. Reduzzi *et al.* [13] brought up the aspect of polarization control, as the population of LIS depends on the relative orientation of the laser polarizations. We note that apart from the transient absorption context these states are dubbed dark states, as they are not accessible by single-photon absorption. In the following we will refer to the basic helium eigenstates, but the notation obviously depends on the viewing angle.

XUV-IR photoelectron measurements employing synchrotron [14] or free-electron laser (FEL) [15] radiation in combination with an IR laser have also been reported. These experiments, however, focused on photoelectron angular distributions (PADs) stemming from single-photon excited states. Building upon our earlier work on photoelectron yields originating from multiphoton excited states [16], the present study comprises a detailed analysis by employing multidimensional data sets. Here, we focus on polarization-

ᵃe-mail: severin.meister@mpi-hd.mpg.de (corresponding author)

dependent or dichroic effects of PADs and their laser-intensity dependence.

The measurement employs FEL-XUV radiation in combination with a synchronized IR laser. Both sources are linearly polarized with adjustable orientation relative to each other. For temporally separate (non-overlapping) pulses, the preceding XUV pulse excites the helium atom to specific $(1snp)^1P$ states, while the delayed IR pulse ionizes the excited atom. For parallel orientation of polarizations and pulses in temporal overlap however, helium can be excited from its $(1s^2)^1S$ ground state to $(1sns)^1S$ and $(1snd)^1D$ states by simultaneous two-photon XUV-IR excitation. By absorbing additional IR photons, the excited atom can be ionized while details of the excited state can be inferred from the angular distribution and the kinetic energy of the emitted electrons. Measured PADs resemble hydrogen orbitals with varying angular momentum ℓ but conserved magnetic quantum number $m = 0$. For orthogonal orientation of the polarization axes, the PAD is altered fundamentally. The axial symmetry of the PAD along the polarization axis is broken, as the magnetic quantum number is $m = \pm 1$ with the IR defining the quantization axis. Furthermore, in this configuration excitation of ^1S states is completely suppressed, as predicted by selection rules for two-photon excitation [17]. Along with excitation, photoionization is suppressed at specific XUV energies, as the resonance enhancement is not available anymore.

We also report on a multiphoton feature just below the $(1s2p)^1P$ resonance involving excitation by one XUV and two IR photons. The analysis of the PADs allows to infer the excitation mechanism and an assignment to the $(1s4f)^1F$ resonance.

Moreover, the IR intensity dependence of PADs is analyzed. Since the XUV pulse deposits most of the required excitation energy into the helium, IR ionization of excited states can be studied at lower laser intensities than in a single-color experiment. Our analysis suggests that the simple multi-photon description is valid except for high IR intensities, as our high-intensity data set shows. Finally, the interpretation of our experimental results is supported by numerical solutions of the time-dependent Schrödinger equation (TDSE) in the single-active electron (SAE) approximation.

This manuscript is organized as follows. Section 2 provides a summary of the experimental (Sect. 2.1) and theoretical (Sect. 2.2) methods. Our results are presented in Sect. 3, separated for ionization via the $(1s3d)^1D$ and $(1s2s)^1S$ excited states 3.1, the $(1s4f)^1F$ excited state 3.2, and the IR intensity dependence of the PADs 3.3. A summary is given in Sect. 4.

2 Methods

2.1 Experimental Setup

The experiment was carried out with the reaction microscope (REMI) endstation [18,19] at the free-electron laser in Hamburg (FLASH2) [20,21] and a short-pulse IR laser based on optical parametric chirped-pulse amplification (OPCPA) [22]. The wavelength tunability of FLASH2 [23] was employed by scanning the XUV photon energy between 20.4 eV and 23.2 eV in steps of 0.1 eV with a bandwidth of 0.2 eV full-width at half maximum (FWHM). The FEL pulse duration was estimated to be about 40 fs FWHM in intensity and the FEL pulse energy was reduced to < 10 nJ, a level where two-XUV-photon absorption is suppressed. The IR laser was stretched to pulse durations of 90 fs (FWHM) to maintain, temporal overlap with the XUV pulses despite the timing jitter of several ten femtoseconds. The IR focal spot diameter of about 30 µm is significantly larger than the FEL focus ($\approx 10\,\mu$m) and reached an intensity on the order of 10^{12} W/cm^2. The effective repetition rate in the measurement was 500 Hz.

The IR and FEL pulses enter the REMI collinearly while their foci overlap in the REMI center. Both the XUV and the IR radiation are linearly polarized, and the IR polarization can be rotated with respect to XUV polarization. A dilute supersonic gas jet of atomic helium crosses the laser foci, triggering single photoionization events. Charged fragments are separated by a homogeneous electric field and guided onto two time- and position-sensitive detectors. In order to achieve high momentum resolution, we selected a low electric field strength of 1.2 V/cm. A magnetic field, collinear with the electric field, forces charged particles on spiral trajectories ensuring a detection in the entire solid angle of 4π [24]. The chosen settings allow a 4π detection of electrons with kinetic energy up to 5 eV. Time-of-flight and position information is used to retrieve the particles' momentum vectors at the time of emission. Imposing momentum conservation on ions and electrons produced during the same laser pulse makes it possible to sort out fragments stemming from the same parent particle.

2.2 TDSE Calculation

The theoretical part of this study is based on numerically solving the TDSE in the SAE approximation. Although the model was described already in [16], we repeat it here for completeness and describe the extensions to implement the polarization. The ground state is effectively described as a $(1s1s')^1S$ state, where the $1s$ is close to the He$^+$ orbital and the $1s'$ is treated like a valence orbital, similar to the $n\ell$ orbitals in all the other $1sn\ell$ Rydberg states. As always in theory, the binding energies of the $n\ell$ valence electrons are not exact (see Fig. 1 for a quantitative overview), especially since we used a single-electron model potential rather than fully accounting for the electron-electron interaction and correlation in an *ab initio* manner. While $1sn\ell$ Rydberg states with orbital angular momenta $\ell \geq 2$ have very accurate binding energies, this is not quite the case for p electrons and particularly for s electrons, due to the small or missing centrifugal barrier. Since excita-
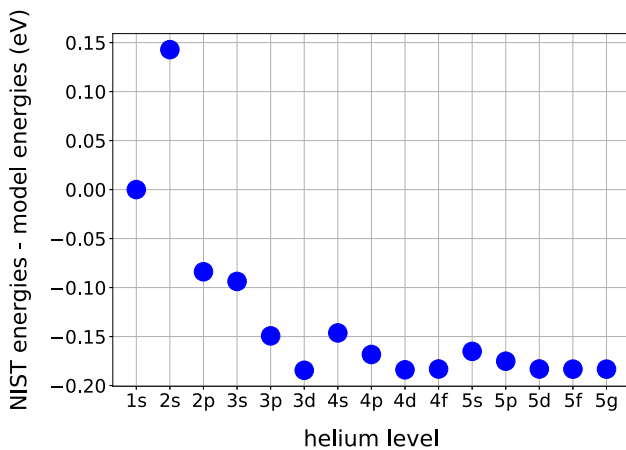
Fig. 1 Comparison of helium excitation energies between NIST [25] and the model of this study. With the ground state set at 0.00 eV, this indicates that the excitation energy of the $2s$ state is underestimated, while all the other excitation energies are slightly overestimated

tion energies are measured from the ground state, much of the remaining discrepancies are due to the binding energy of the $1s'$ orbital.

Specifically, we used the one-electron potential,

$$V(r) = -\frac{1}{r} - \left(\frac{1}{r} + 1.3313\right) \exp(-3.0634\,r), \quad (1)$$

where r is the distance from the nucleus, to calculate the valence orbitals. The deviations in the excitation energies, compared to the recommended values from the NIST database [25], are less than 0.2 eV even in the worst-case scenario (see Fig. 1) and do not alter the essential conclusions presented below. In the following we will usually omit the inner $1s$ electron and the total spin state (it would be a singlet in the two-electron description) to simplify the notation. Doubly excited states are not accessible with the photon energies used in the present experiment, and spin-forbidden transitions (i.e., excitation of triplet states) are negligible.

The laser intensity was chosen according to the available knowledge regarding the actual experimental conditions. The XUV pulse duration was taken as 40 fs (FWHM value of a peak intensity of 10^{10} W/cm^2 with a Gaussian envelope) and the IR pulse duration as 80 fs (FWHM). While the XUV photon energy was varied over a range in steps of 0.05 eV, the central IR photon energy was held fixed at 1.55 eV (800 nm).

Due to the fact that the lasers are linearly polarized along different directions, the cylindrical symmetry of the problem that we could take advantage of in the previous work [16] is no longer valid. The complications, however, are manageable in a straightforward way by employing an updated version of the code described by Douguet *et al.* [26]. Specifically, we used the velocity gauge and a variable radial grid step starting at 0.1 a.u. near the nucleus and gradually increasing to 0.2 a.u. far away, where we only need to describe rel-
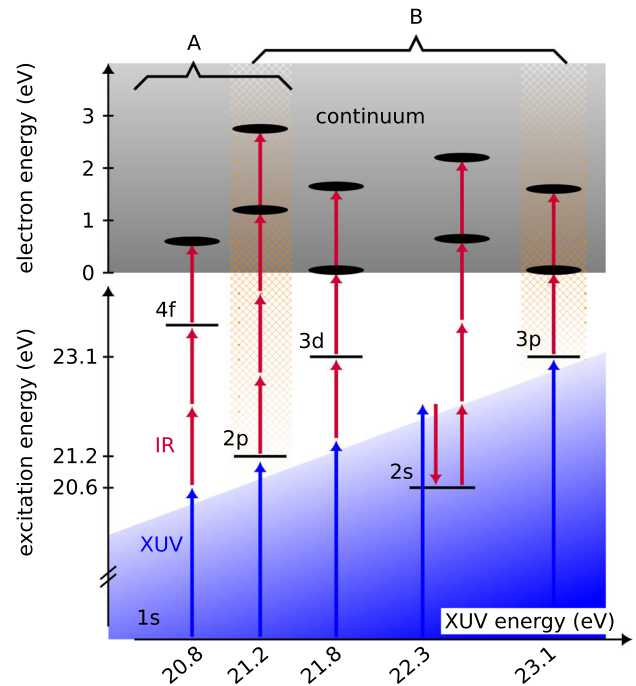
Fig. 2 Excitation and ionization scheme of the XUV energy scan in helium. For preceding XUV pulses there is only single XUV-photon absorption inducing p-state excitation (hatched orange region). For excitation into states with $\ell \neq 1$ a combination of an XUV photon and IR photons is required. Two-color multi-photon excitation is only possible for temporally overlapping pulses

atively slow electrons. The timestep was set constant at 0.05 a.u., partial waves up to $\ell_{max} = 12$ were coupled, and the numerical convergence of the predictions was checked by varying the parameters. Any apparent shortcomings of the theoretical results presented below are expected to be due to either the deficiency of the SAE model itself and/or the remaining uncertainties in the knowledge and, consequently, the description of the laser parameters.

3 Results and Discussion

3.1 Dichroism in Ionization via the 3d and 2s Excited States

A straightforward interpretation of the presented excitation and ionization mechanism is provided for XUV pulses preceding IR pulses. At matching XUV photon energies in the scanning range, the helium atom can be excited from the $1s$ ground state to np states. By absorbing additional photons of the moderately intense ($\approx 4 \times 10^{12}$ W/cm^2) delayed IR pulse, the excited atom can be ionized. The energy of the measured photoelectron depends on the binding potential of the excited state and the number of absorbed IR photons. Figure 2 shows schematically the underlying excitation and ion-
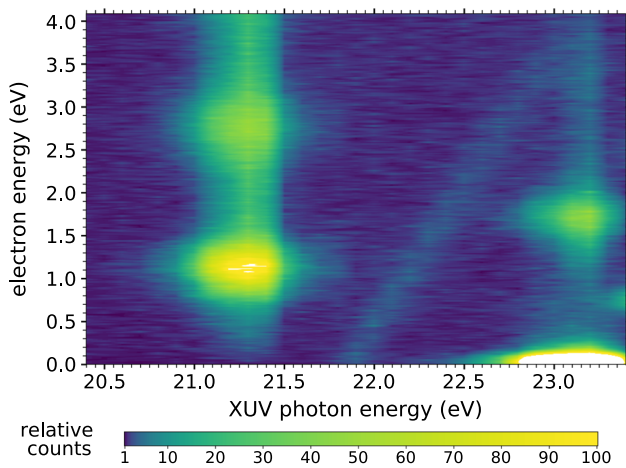
Fig. 3 Measured photoelectron yield as function of the photoelectron kinetic energy and XUV photon energy ($E\gamma$-plot) for preceding XUV pulses. At 21.2 eV (23.1 eV) the $2p$ ($3p$) state gets populated by the XUV. A subsequent IR pulse ionizes the excited atom. The emitted electrons appear as ATI peaks on the electron-energy axis. The diagonal line shows shakeup-ionization by the third harmonic of the FEL, leaving the He$^+$ in its first excited state

ization mechanism. The hatched regions in orange indicate the pathways that are accessible in the case of preceding XUV pulses. For example, the hatched region on the left shows ionization of helium via the $2p$ (21.2 eV) state. One XUV photon excites the atom to the $2p$ state and the additional absorption of at least three IR photons (1.55 eV each) from the delayed IR pulse results in ionization. The emitted photoelectron is detected and its measured kinetic energy can be reproduced by calculating the excess energy as follows:

$$E_{\mathrm{XUV}}(21.2 \text{ eV}) + 3 \cdot E_{\mathrm{IR}}(1.55 \text{ eV})$$
$$- I_{\mathrm{p}}(24.6 \text{ eV}) = E_{\mathrm{ele}}(1.2 \text{ eV}) \quad (2)$$

The atom can also absorb more photons than the minimum number required for ionization. The effect of above-threshold ionization (ATI) [27,28] manifests itself as regions of high yield separated by 1.55 eV in the electron energy.

The gray "continuum" region in the top of Fig. 2 illustrates the experimentally accessible part of the scheme. Respectively, Fig. 3 depicts the measured photoelectron yield as a function of the photoelectron kinetic energy and the scanned XUV photon energy ($E\gamma$-plot) for temporally delayed IR pulses. Here, the same XUV energy range as in Fig. 2 is depicted, while Fig. 4 and Sect. 3.2 will focus on regions B and A (cf. Fig. 2), respectively. According to the mechanism described, Fig. 3 shows a high yield of photoelectrons at XUV photon energies of the $2p$ (21.2 eV) and the $3p$ (23.1 eV) states. ATI peaks are found along the electron-energy axis, separated by the energy of one IR photon.

The diagonal line, starting at around 21.8 eV in Fig. 3, can be attributed to the third harmonic of the FEL. At this fundamental frequency, the third harmonic has an energy of 65.4 eV, just sufficient to ionize the helium atom ($I_{\mathrm{p}} = 24.6$ eV) and leaving the He$^+$ ion in its first excited state ($n = 2$, 40.8 eV). The diagonal has a slope of three, as the photoelectron takes the excess energy.

For XUV and IR pulses in temporal overlap, the situation changes substantially, as various excitation pathways open up. In this case the helium atom is dressed in the IR radiation field during the XUV pulse and can absorb or emit IR photons, allowing access to transitions beyond the one-photon electric dipole selection rules. The simplest case of two-color two-photon excitation allows to couple the $1s$ ground state to ns and nd states. By absorbing additional IR photons, the excited atom can again get ionized, and the emitted photoelectron is measured.

In the case where both radiation fields are simultaneously present, all ionization pathways depicted in Fig. 2 are accessible. For excitation into the $3d$ state, the helium atom conjointly absorbs one XUV photon and one IR photon from the laser field. We also observe excitation into the $2s$ state, where conjointly to the XUV-photon absorption one IR photon is emitted to the laser field. As reported in reference [16], these two states dominate the light-induced features for the chosen IR and XUV parameters between the $2p$ and the $3p$ states. A detailed measurement in the XUV energy region B (cf. Fig. 2) is presented in Fig. 4. Subplot (a) is recorded for parallel polarization and shows two regions of high yield around 21.8 eV and 22.3 eV, which can be attributed to the $3d$ and the $2s$ states, respectively. The distribution of electron energies is broad due to the IR laser bandwidth and shortened lifetimes of the rapidly ionizing states. The broadness of the peaks along the XUV energy axis can be attributed to the XUV bandwidth and the AC Stark shift. The latter effect becomes
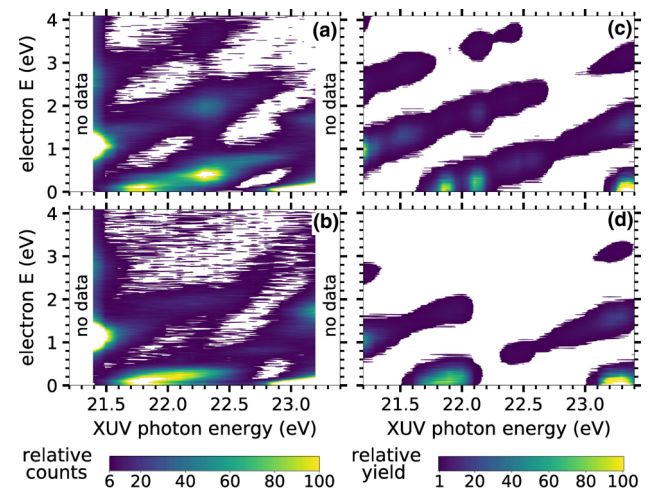
Fig. 4 $E\gamma$-plot of region B (cf. Fig. 2). Experiment: **a** parallel, **b** orthogonal polarization. Calculation: **c** parallel, **d** orthogonal polarization

even more pronounced as the timing jitter between pulses leads to varying IR intensities when the XUV pulses are present. This effect was accounted for in the TDSE calculation of Fig. 4c by summing over three IR intensities (1, 2 and 3×10^{12} W/cm^2). Here, the two dominant multiphoton excitation features of the experiment are well reproduced, even though they are located at slightly different XUV photon energies. As mentioned in Sect. 2.2, the binding and, consequently, the excitation energies of our model deviate from the ones recommended by NIST. In fact our model underestimates the excitation energy of the $2s$ state and overestimates that of the $3d$ state, which explains the remaining differences between calculation and experiment.

Two-color multi-photon excitation includes the additional degree of freedom to change the relative orientation of the polarizations. By exploiting this handle, specific excitation pathways, and with it photoionization, can be deliberately suppressed. The measurement depicted in Fig. 4b is recorded with the same parameters as in (a), except for the orthogonal orientation of the polarization axes. While the $3d$ feature remains, the signal of the $2s$ state vanishes. This finding is predicted by the "two-photon electric-dipole selection rules" [17] for photons of differing frequency. According to this rule, the transition $\Delta J : 0 \rightarrow 0$ of the total electronic angular momentum is forbidden, while the magnetic quantum number m has to change by $\Delta m = \pm 1$. Since spin-flips during the excitation process are negligible, the ground-state spin (S = 0) is conserved and $L = J$.

The elongated region of high yield from the $3d$ state along the XUV photon-energy axis can be explained by the AC Stark shift. A pronounced shift of this state is described in Chen *et al.* [7] and Meister *et al.* [16]. In combination with the temporal jitter of the two radiation fields, it leads to the elongated feature. The calculated data for the orthogonal case are depicted in Fig. 4d. Similar to the experimental observation, the $2s$ state disappears while the $3d$ feature remains.

In addition to the kinetic energy of the photoelectrons, their angular distribution is measured. This allows us to deduce the quantum numbers of the excited state from which the electron was emitted. Figure 5 shows the measured three-dimensional photoelectron momentum distribution, which contains the PAD. Bins in momentum space are color-coded by the number of counts; each dot represents a photoelectron count. The two-dimensional plots on the walls depict the momentum distribution integrated along one axis.

Electrons in both subplots stem from the $3d$ resonance and were recorded at 21.8 eV XUV photon energy with their kinetic energy in the range from 0.07 eV to 0.16 eV. The weak contribution of the third harmonic is negligible and shows an isotropic PAD.

The PAD in Fig. 5a was measured for parallel polarization axes. In this configuration, each contributing photon changes the angular momentum by $\Delta \ell = \pm 1$ while the magnetic quantum number $m = 0$ is conserved from its ground-state value. The change of ℓ and m upon photon absorption is depicted in Fig. 6. For the measured "f-like" ($\ell = 3$) continuum distribution emission is found along the polarization axes and in two rings orthogonal to them. This suggests that the ionization proceeds via a d state.
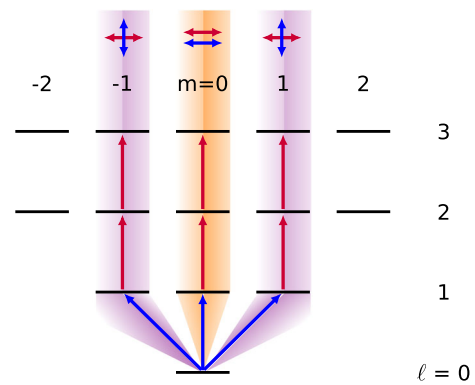
Fig. 6 Scheme of angular momentum ℓ and magnetic quantum number m upon multi-photon excitation. For XUV (blue) and IR (red) polarization parallel to each other, $\Delta m = 0$. For orthogonal orientation, $\Delta m = \pm 1$
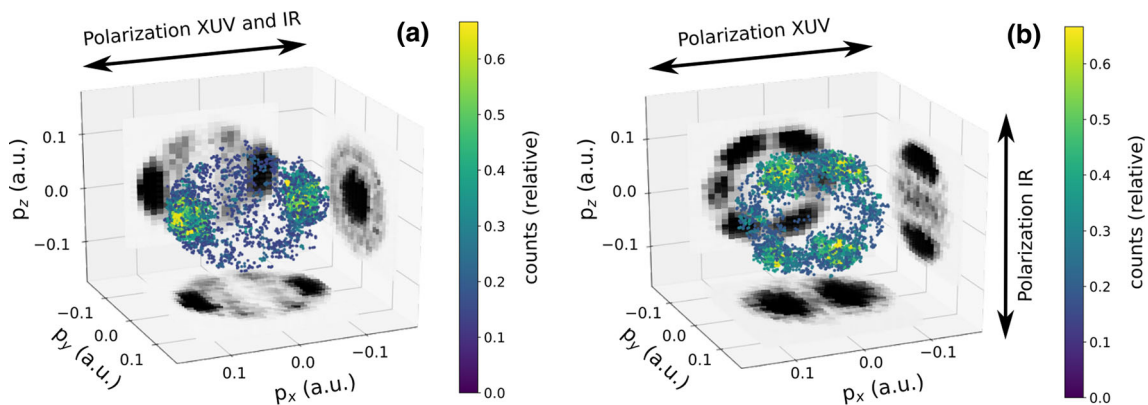
Fig. 5 Momentum distribution of photoelectrons stemming from the $3d$ LIS. The polarization axes of the XUV and IR are **a** parallel and **b** orthogonal to each other
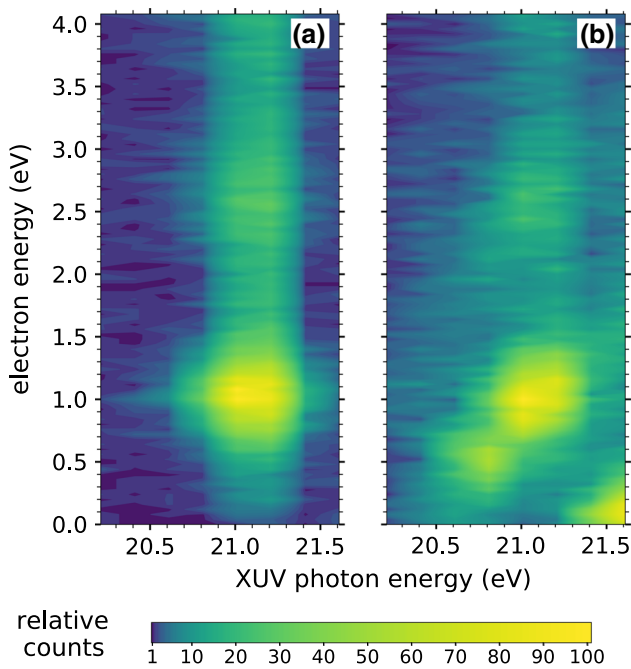
Fig. 7 Measured $E\gamma$-plot for region A (cf. Fig. 2) and parallel polarization. **a** Preceding XUV pulse, **b** temporal overlap. Ionization through a 2-IR-photon-coupled $4f$ state is observed at an XUV photon energy of 20.8 eV

Fig. 8 Photoelectron momentum distributions integrated along the laser propagation direction y for parallel polarization axes. The measured distributions are displayed in the top row, the calculated distributions in the bottom row

The PAD changes substantially in the case of orthogonal polarizations. The axial symmetry along the IR polarization is broken, and the distribution resembles that of a hydrogen orbital with $\ell = 3$ and $m = \pm 1$. This can be explained by taking the IR polarization as the quantization axis, so the linear polarization of the XUV is expressed as a superposition of right-hand and left-hand circularly polarized radiation fields. In this way, it is straightforward to see that the magnetic quantum number changes according to $\Delta m = \pm 1$ upon absorption of an XUV photon. The absorption of IR photons, on the other hand, does not change m. This is illustrated in Fig. 6.

3.2 Ionization via the 4f Excited State

For high IR intensities ($\approx 8 \times 10^{12}$ W/cm^2), we find a further peak at 20.8 eV, below the $2p$ resonance peak . A LIS for similar IR parameters in the same XUV energy range was observed by Chini *et al.* [10] in a transient-absorption (TA) measurement. It was tentatively assigned to excitation of np states by the absorption of one XUV photon and two IR photons. The present measurement however, suggests the feature to be a resonant enhancement of ionization via the $4f$ state as explained in the following.

Figure 7 shows an $E\gamma$-plot of region A (cf. Fig. 2) for parallel polarization axes. In subplot (a), the XUV pulse precedes the IR pulse, and thus ionization is restricted to resonant enhancement via p-state excitation. Within the depicted XUV energy range (scanned

in 0.2 eV steps), there is only ionization via the $2p$ state at around 21.2 eV. The electron energy is about 1.2 eV, as the excited atom becomes ionized by absorbing three IR photons. This ionization pathway was previously described in Sect. 3.1 and is depicted in Fig. 2. For pulses in temporal overlap, the dressing IR-field opens up an additional excitation pathway. A new peak appears in Fig. 7b at slightly lower XUV photon energies and electron kinetic energies ($E_{\mathrm{XUV}} \approx 20.8$ eV, $E_{\mathrm{kin}} \approx 0.6$ eV) compared to the first ATI peak from the $2p$ state.

The following energetic considerations rule out certain excitation pathways and lead to the final assignment of the involved state. As the peak is only present for overlapping pulses, two-color excitation has to be considered. For excitation by one XUV photon plus one IR photon, even the lowest s and d states are out of reach (20.8 ± 1.55 eV) to be connected to the peak. The $2s$ (20.6 eV) state is too close to be populated, while the next $3s$ (22.9 eV) and $3d$ (23.1 eV) states are already too high to be populated. By considering an excitation involving absorption of one XUV photon plus two IR photons, there are nf and np states available. The angular momenta of the three photons either add up, changing the ground-state angular momentum by $\Delta\ell = +3$, or two angular momenta cancel each other resulting in $\Delta\ell = +1$. The case of negative $\Delta\ell$ is omitted, because the angular momentum of the helium ground state is already the lowest possible. The total available excitation energy is $E_{\mathrm{EXC}} = E_{\mathrm{XUV}}(20.8\ \mathrm{eV}) + 2 \cdot E_{\mathrm{IR}}(1.55\ \mathrm{eV}) = 23.9$ eV.

Possible excited states are $4p$ and $4f$, both with a binding energy of about 23.75 eV, and the $5p$ and $5f$ states, both with a binding energy of about 24.05 eV. In order to decide which states are more likely to be populated (either $n = 4$ or $n = 5$), we consider the AC Stark shift. To estimate the shift of these higher excited states, we take the shift between the $2p$ peak at 1.05 eV in Fig. 7b and the field-free value of Eq. 2 at 1.2 eV. By including the shift of about 0.15 eV, the binding energy of the $4p$ and $4f$ states is found at the matching excitation energy of 23.9 eV. This estimate is reasonable, as the highly excited states ($n = 4, 5$) experience a similar energetic shift with IR intensity as the continuum level. The possible resonances involved in the laser-dressing peak in Fig. 7b are narrowed down to the $4p$ and the $4f$ states.

The final identification is performed by analyzing the angular distribution of the photoelectrons stemming from the excited state. Figure 8 shows the measured and calculated photoelectron momentum distributions for parallel orientation of the polarization axes. The three-dimensional data are integrated along the mutual propagation direction y of the radiation fields and normalized to the total yield to provide a convenient comparison. The two plots in the upper row show the measured PAD of ionization through the $2p$ state and the nearby light-induced $4f$ state. In both cases emission is found along the polarization axis x and in three rings around the axes, appearing as three vertical lines. This distribution is "g-like" and corresponds to a continuum state with angular momentum $\ell = 4$. Consequently, this PAD pinpoints the excited state to be the $4f$ state rather than the $4p$ state, supported by monitoring the excited-state population during and after the pulse, which is possible in the calculation.

The two plots in the bottom row of Fig. 8 were generated by the numerical calculation described in Sect. 2.2. The electron kinetic energy was cut off at 1.8 eV to avoid an overlay of higher ATIs in the projection. The IR intensity was set to 3×10^{12} W/cm^2 and the XUV photon energy range was adapted to select the peak of interest. We introduced a Gaussian uncertainty in the electron energy of 0.2 eV to mimic the experimental conditions, including the IR bandwidth and the Stark broadening due to the temporal jitter between the pulses.

The $4f$ peak is also observed for orthogonal polarization axes. The measured $E\gamma$-plot in Fig. 9 samples region A (cf. Fig. 2) in steps of 0.1 eV. Similar to Fig. 7, subplot (a) is recorded for preceding XUV pulses, while (b) is recorded in temporal overlap. The peak appears at the same electron energy and XUV photon energy as in the case of parallel polarization.

Again, by analyzing the PAD of the peak, the ionization-enhancing resonance can be identified. Subplots in the top row of Fig. 10 depict the measured photoelectron momentum distribution for orthogonal polarization. In this case the magnetic quantum number increases to one, following the same argumentation as given in Sect. 3.1. Electrons are emitted in eight equally spaced solid-angle sections perpendicular to the
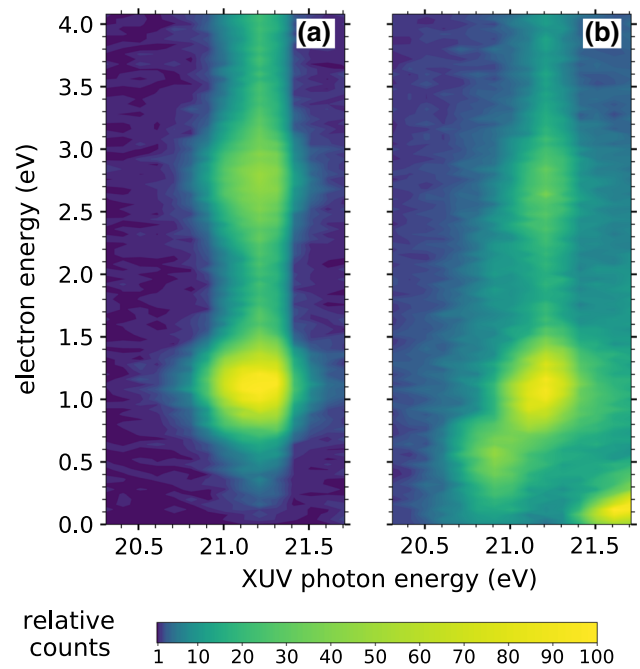
Fig. 9 Measured $E\gamma$-plot for region A (cf. Fig. 2) and orthogonal polarization. **a** Preceding XUV pulse, **b** temporal overlap. Ionization through a 2-IR-photon-coupled $4f$ state is observed at an XUV photon energy of 20.8 eV
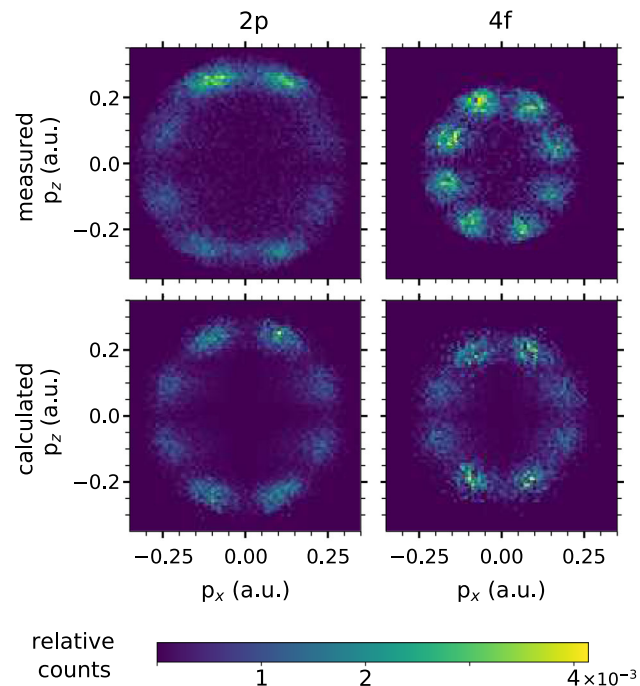
Fig. 10 Photoelectron momentum distributions integrated along the laser propagation direction y for orthogonal polarization axes. The measured distributions are displayed in the top row, the calculated distributions in the bottom row

laser propagation axis y. The node count corresponds to an $\ell = 4$ continuum state and, therefore, to an $\ell = 3$ excited f-state the electron was emitted from. There is good agreement in Fig. 10 between the experimental data in the top row and the theoretical predictions in the bottom row. Characteristics like the number of nodes and their relative intensity are reproduced as well as the diameter corresponding to the photoelectron kinetic energy.

3.3 IR Intensity Dependence of PADs

In the present XUV-IR scheme, the main energy contribution to ionization is provided by one XUV photon. This allows ionization of helium from excited states where electrons are less strongly bound. Electrons can be lifted over the remaining potential barrier by absorbing just a few additional IR photons, in contrast to ionization by an IR laser only, where strong fields are required. In the extreme case of tunnel ionization, electrons are predominantly emitted along the polarization axis, giving rise to the classical picture of electrons being accelerated along the electric field lines. On the contrary, at lower laser intensities within the multiphoton regime, complex PADs emerge, corresponding to discrete number of absorbed photons and angular momenta.

The present measurement exhibits PADs that indicate the photoionization process leaving the simple multi-photon regime. The Keldysh parameter γ [29] can be used to roughly quantify the localization within the continuous transition from the tunneling regime ($\gamma < 1$) to the multi-photon regime ($\gamma \gg 1$). The parameter is defined as

$$\gamma = \frac{\sqrt{2I_p}\,\omega}{E_0}. \tag{3}$$

Here I_p is the ionization potential, ω the frequency, and E_0 the maximum field strength (all in atomic units). In the present experiment, helium is ionized from the $2p$ state, yielding $\gamma_{\mathrm{high}} = 1.9$ in the high IR intensity case ($\approx 8 \times 10^{12}$ W/cm^2) and $\gamma_{\mathrm{low}} = 5.3$ in the low IR intensity case ($\approx 1 \times 10^{12}$ W/cm^2). While γ_{low} is well within the multi-photon regime, γ_{high} enters the transition region.

Figure 11 shows calculated PADs for XUV and IR pulses in temporal overlap with parallel polarization axes. The angle Θ is defined as the angle between the polarization axis and the emission direction of the photoelectron. Photoelectrons in Fig. 11 are selected to cover the first ATI peak of ionization via the $2p$ state (XUV energy from 21.1 eV to 21.5 eV, electron energy from 0.6 eV to 1.4 eV). The data are normalized to the total integral yield. The number of maxima in Fig. 11 corresponds to the four absorbed photons (compare Fig. 2) and thus to the accumulated angular momentum. At low IR intensity, the PAD exhibits very pronounced minima and maxima, while at higher IR intensity the distribution changes distinctly. The minima at
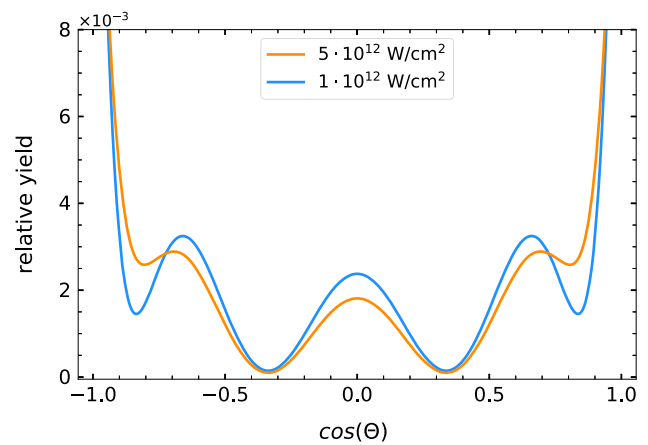
Fig. 11 Calculated PAD of the first ATI peak at 21.2 eV for temporal overlap and parallel polarization
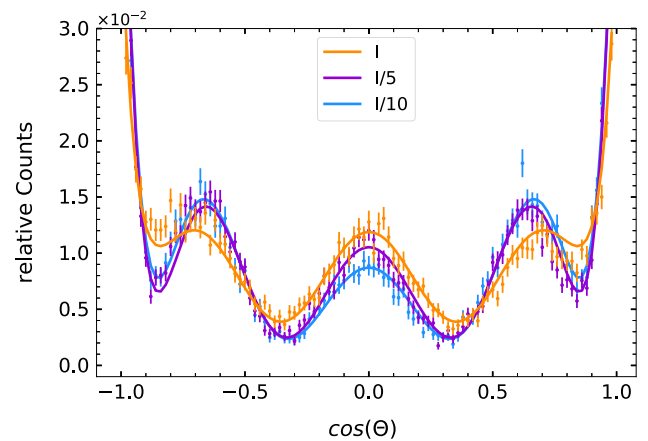
Fig. 12 Measured PAD according to Fig. 11. The selected electron energy range is 0.8 eV to 1.4 eV. The solid lines are fits to the data. See text for details

$\cos(\Theta) = \pm 0.8$ smear out and the center maximum decreases. This trend can be regarded as the onset of the transition region to tunnel ionization, where emission is predominantly found along the polarization axis, where $\cos(\Theta) = \pm 1$.

Corresponding to the calculation, Fig. 12 shows the measured PAD of electrons emitted from the first ATI at $E_{\mathrm{XUV}} \approx 21.2$ eV and $E_{\mathrm{kin}} \approx 1.2$ eV. Similar to theory, we find the PAD to change with IR intensity. This is not obvious in first place as the number of absorbed photons stays the same. The two minima around $\cos(\Theta) = \pm 0.8$ smear out for increasing IR intensity, as predicted by the calculation. However, in contrast to theory, the center maximum increases in magnitude.

The solid lines in Fig. 12 depict fitted results to the data with their corresponding parameters listed in Table 1. The PAD can be described by the finite sum of even-rank Legendre polynomials P_n scaled with β_n

Table 1 Beta parameters of the fit in Fig. 12. All absolute errors $\leq \pm 0.05$

Int	β_2	β_4	β_6	β_8	β_{10}	β_{12}
I	0.83	0.75	0.18	**1.22**	-0.10	**0.10**
I/5	1.12	0.90	0.98	**1.95**	-0.22	**-0.02**
I/10	1.27	0.76	0.95	**1.85**	-0.16	**-0.09**

parameters [30,31]:

$$\frac{d\sigma}{d\Omega} = \frac{\sigma_0}{4\pi}\left(1 + \sum_{n\in\mathbb{N}} \beta_{2n} P_{2n}(\cos(\Theta))\right) \qquad (4)$$

Here σ_0 is the total emission cross section, and the angle Θ is defined as before. As explained in Ref. [5], the β_8 parameter corresponds to g-waves generated by four-photon absorption from the $\ell = 0$ ground state, which is dominating in the presented case. For high intensities β_8 decreases as well as lower order β-parameters (cf. Table 1). To explain the qualitative and quantitative observations at high IR intensities, mechanisms of higher order have to be considered. In the simplest case, the emitted electron can absorb one IR photon and emit one IR photon while conserving the photoelectron energy. The PAD, however, which reflects the angular momenta, is altered by this process. This is taken into account by extending the sum of equation 4 up to β_{12}, which allows to describe a six-photon process. However, the products $\beta_{2n}P_{2n}$ for different n are not disentangled, which makes a strict quantitative statement about the contribution of higher orders tentative.

Mayer *et al.* [5] investigated the laser-intensity dependence of PADs for similar parameters in an HHG-IR laser scheme. However, their findings are only comparable with ours to a limited extent, as the periodic HHG-based XUV spectrum couples to multiple excitation pathways.

An explanation for the slight discrepancy between theory and experiment (Figs. 11, 12), but also inconsistencies in Table 1, can be found in additional resonances being involved in the ionization process. The energy difference between the $2p$ state and higher-lying np states ($n = 6, 7, 8$) is about twice the IR photon energy. Theory might populate or miss some of these states due to its narrow IR bandwidth in contrast to experiment. Slight differences in resonance energies (imperfect model energies) and intensities (experimental temporal jitter) between the calculation and experiment lead to different contributions from the Rydberg np states, thus resulting in a discrepancy between the measured and calculated PADs.

4 Summary

We investigated photoelectron emission via excited states in laser-dressed atomic helium. The experimental results are in good agreement with TDSE calculations based on an SAE model. The simultaneous interplay of XUV and IR radiation enabled populating ^1S, ^1D and ^1F states, which are not accessible by single-photon absorption from the ground state. Two-color multiphoton excitation has an additional degree of freedom in the relative orientation of the polarizations. We analyzed the dichroic effect of different relative orientations on the PAD of electrons stemming from the $(1s3d)^1D$ state. For parallel orientation we found a PAD resembling a hydrogen orbital with $\ell = 3$ and $m = 0$, while for orthogonal orientation there is $\ell = 3$ and $m = \pm 1$. Furthermore, by changing the relative polarization direction, the photoionization signal can be suppressed at specific XUV energies. This can be explained by the fact that for orthogonal polarization axes the transition from the ^1S ground state to an ^1S excited state is forbidden by the two-photon selection rules, in contrast to the case of parallel polarization.

Finally, we investigated the IR laser intensity dependence of PADs obtained from photoelectrons of fixed energy. The electrons were emitted from the $2p$ state by the absorption of three IR-photons. At high IR intensities, we found the PAD to blur and higher-order terms to come into play. This observation can be regarded as the onset of the process to transit from the multiphoton to the tunneling regime.

Data availability statement This manuscript has no associated data or the data will not be deposited. [Authors' comment: The data to create the figures is available upon request.]

References

1. P.B. Corkum, Plasma perspective on strong field multiphoton ionization. Phys. Rev. Lett. **71**, 1994–1997 (1993)

2. M. Lewenstein, P. Balcou, M.Y. Ivanov, A. L'Huillier, P.B. Corkum, Theory of high-harmonic generation by low-frequency laser fields. Phys. Rev. A **49**, 2117–2132 (1994)

3. L.H. Haber, B. Doughty, S.R. Leone, Continuum phase shifts and partial cross sections for photoionization from excited states of atomic helium measured by high-order harmonic optical pump-probe velocity map imaging. Phys. Rev. A **79**, 031401 (2009)

4. P. Ranitovic, X.M. Tong, B. Gramkow, S. De, B. DePaola, K.P. Singh, W. Cao, M. Magrakvelidze, D. Ray, I. Bocharova, H. Mashiko, A. Sandhu, E. Gagnon, M.M. Murnane, H.C. Kapteyn, I. Litvinyuk, C.L. Cocke, IR-assisted ionization of helium by attosecond extreme ultraviolet radiation. New J. Phys. **12**(1), 013008 (2010)

5. N. Mayer, P. Peng, D.M. Villeneuve, S. Patchkovskii, M. Ivanov, O. Kornilov, M.J.J. Vrakking, H. Niikura, Population transfer to high angular momentum states in infrared-assisted XUV photoionization of helium. J. Phys. B Atomic Mol. Opt. Phys. **53**(16), 164003 (2020)

6. P. Johnsson, J. Mauritsson, T. Remetter, A. L'Huillier, K.J. Schafer, Attosecond control of ionization by wavepacket interference. Phys. Rev. Lett. **99**, 233001 (2007)

7. M. Shaohao Chen, J. Bell, A.R. Beck, H. Mashiko, W. Mengxi, A.N. Pfeiffer, M.B. Gaarde, D.M. Neumark, S.R. Leone, K.J. Schafer, Light-induced states in attosecond transient absorption spectra of laser-dressed helium. Phys. Rev. A **86**, 063408 (2012)

8. W. Mengxi, S. Chen, S. Camp, K.J. Schafer, M.B. Gaarde, Theory of strong-field attosecond transient absorption. J. Phys. B Atomic Mol. Opt. Phys. **49**(6), 062003 (2016)

9. M. Justine Bell, A.R. Beck, H. Mashiko, D.M. Neumark, S.R. Leone, Intensity dependence of light-induced states in transient absorption of laser-dressed helium measured with isolated attosecond pulses. J. Mod. Opt. **60**(17), 1506–1516 (2013)

10. M. Chini, X. Wang, W. Yan Cheng, D. Yi, D.A. Zhao, S.-I. Telnov, Z.C. Chu, Sub-cycle oscillations in virtual

11. states brought to light. Scientific Reports **3**(1), 1105 (2013)

11. W.S. Chen, M.B. Mengxi, M. Gaarde, M.B. Schafer, Quantum interference in attosecond transient absorption of laser-dressed helium atoms. Phys. Rev. A **87**, 033408 (2013)

12. J.E. Bækhøj, L.B. Madsen, Light-induced structures in attosecond transient-absorption spectroscopy of molecules. Phys. Rev. A **92**, 023407 (2015)

13. M. Reduzzi, J. Hummert, A. Dubrouil, F. Calegari, M. Nisoli, F. Frassetto, L. Poletto, W. Shaohao Chen, M.B. Mengxi, K.S. Gaarde, G. Sansone, Polarization control of absorption of virtual dressed states in helium. Phys. Rev. A **92**, 033408 (2015)

14. P.O. Keeffe, A. Mihelič, P. Bolognesi, M. Žitnik, A. Moise, R. Richter, L. Avaldi, Near-threshold photoelectron angular distributions from two-photon resonant photoionization of he. New J. Phys. **15**(1), 013023 (2013)

15. S. Mondal, H. Fukuzawa, K. Motomura, T. Tachibana, K. Nagaya, T. Sakai, K. Matsunami, S. Yase, M. Yao, S. Wada, H. Hayashita, N. Saito, C. Callegari, K.C. Prince, P.O. Keeffe, P. Bolognesi, L. Avaldi, C. Miron, M. Nagasono, T. Togashi, M. Yabashi, K.L. Ishikawa, I.P. Sazhina, A.K. Kazansky, N.M. Kabachnik, K. Ueda, Photoelectron angular distributions in infrared onephoton and two-photon ionization of FEL-pumped rydberg states of helium. J. Phys. B Atomic. Mol. Opt. Phys. **46**(20), 205601 (2013)

16. S. Meister, A. Bondy, K. Schnorr, S. Augustin, H. Lindenblatt, F. Trost, X. Xie, M. Braune, R. Treusch, B. Manschwetus, N. Schirmel, H. Redlin, N. Douguet, T. Pfeifer, K. Bartschat, R. Moshammer, Photoelectron spectroscopy of laser-dressed atomic helium. Phys. Rev. A **102**, 062809 (2020)

17. K.D. Bonin, T.J. McIlrath, Two-photon electric-dipole selection rules. J. Opt. Soc. Am. B **1**(1), 52–55 (1984)

18. S. Meister, H. Lindenblatt, F. Trost, K. Schnorr, S. Augustin, M. Braune, R. Treusch, T. Pfeifer, R. Moshammer, Atomic, molecular and cluster science with the reaction microscope endstation at flash2. Appl. Sci. **10**, 2953 (2020)

19. G. Schmid, K. Schnorr, S. Augustin, S. Meister, H. Lindenblatt, F. Trost, Y. Liu, M. Braune, R. Treusch, C.D. Schröter, T. Pfeifer, R. Moshammer, Reaction microscope endstation at FLASH2. J. Synchrot. Rad. **26**(3), 854–867 (2019)

20. W. Ackermann, G. Asova, V. Ayvazyan, A. Azima, N. Baboi, J. Bähr, V. Balandin, B. Beutner, A. Brandt, A. Bolzmann, R. Brinkmann, O.I. Brovko, M. Castellano, P. Castro et al., Operation of a free-electron laser from the extreme ultraviolet to the water window. Nat. Photon. **1**(6), 336–342 (2007)

21. B. Faatz, E. Plönjes, S. Ackermann, A. Agababyan, V. Asgekar, V. Ayvazyan, S. Baark, N. Baboi, V. Balandin, N. von Bargen, Y. Bican, O. Bilani, J. Bödewadt, M. Böhnert, R. Böspflug, S. Bonfigt, H. Bolz, F. Borges, O. Borkenhagen, M. Brachmanski et al., Simultaneous operation of two soft x-ray free-electron lasers driven by one linear accelerator. New J. Phys. **18**(6), 062002 (2016)

22. T. Lang, S. Alisauskas, U. Große-Wortmann, T. Hülsenbusch, B. Manschwetus, C. Mohr, J. Müller,

F. Peters, N. Schirmel, S. Schulz, A. Swiderski, J. Zheng, I. Hartl. Versatile opcpa pump-probe laser system for the flash2 xuv fel beamline at desy, in *2019 Conference on Lasers and Electro-Optics Europe European Quantum Electronics Conference (CLEO/Europe-EQEC)*, p. 1 (2019)

23. B. Faatz, M. Braune, O. Hensler, K. Honkavaara, R. Kammering, M. Kuhlmann, E. Plönjes, J. Roensch-Schulenburg, E. Schneidmiller, S. Schreiber et al., The flash facility: advanced options for flash2 and future perspectives. Appl. Sci. **7**(11), 1114 (2017)

24. J. Ullrich, R. Moshammer, A. Dorn, R. Dörner, L. Ph, H. Schmidt, H. Schmidt-Böcking, Recoil-ion and electron momentum spectroscopy: reaction-microscopes. Reports Progr. Phys. **66**(9), 1463–1545 (2003)

25. A. Kramida, Yu. Ralchenko, J. Reader, and and NIST ASD Team. NIST Atomic Spectra Database (ver. 5.8), [Online]. https://physics.nist.gov/asd, January 14. National Institute of Standards and Technology, Gaithersburg, MD, p. 2020 (2021)

26. N. Douguet, A.N. Grum-Grzhimailo, E.V. Gryzlova, E.I. Staroselskaya, J. Venzke, K. Bartschat, Photoelectron angular distributions in bichromatic atomic ionization induced by circularly polarized vuv femtosecond pulses. Phys. Rev. A **93**, 033402 (2016)

27. P. Agostini, F. Fabre, G. Mainfray, G. Petite, N.K. Rahman, Free-free transitions following six-photon ionization of xenon atoms. Phys. Rev. Lett. **42**, 1127–1130 (1979)

28. Y. Gontier, M. Poirier, M. Trahin, Multiphoton absorptions above the ionisation threshold. J. Phys. B Atomic Mol. Phys. **13**(7), 1381–1387 (1980)

29. L.V. Keldysh, Ionization in the field of a strong electromagnetic wave. Sov. Phys. JETP. **20**, 1307–1314 (1965)

30. J. Cooper, R.N. Zare, Angular distribution of photoelectrons. J. Chem. Phys. **48**(2), 942–943 (1968)

31. L. Katharine, Reid, Photoelectron angular distributions. Ann. Rev. Phys. Chem. **54**(1), 397–424 (2003)

4.5 Two-photon double ionization of argon

In this paper we investigate the correlation between two photoelectrons of atomic argon. Results are obtained by analyzing the photoelectron angular distributions.

The single-color experiment is performed with intense XUV radiation of the FLASH. This allows to absorb two photons within the same atom. As the photon energy is chosen just above the double-ionization threshold ($E_\gamma > I_p^{2+} = 27.6\,\text{eV}$ [78]) the atom is dominantly found to be doubly ionized in two steps. Absorption of a first photon leads to ionization of the argon atom and absorption of a second photon further ionizes the Ar^+ ion. This process is called sequential double ionization (SDI). For our analysis we measure the angular distribution of both photoelectrons in SDI and simultaneously the angular distribution of photoelectrons stemming from single ionization.

We find the angular distribution of the first photoelectron in SDI to differ from photoelectrons of single ionization. A naive view on the step wise SDI process would suggest the PADs to be identical. However, the polarization of the intermediate Ar^+ ion leads to pre-selection of the first electrons in SDI and the correlation between both photoelectrons in SDI.

Furthermore, we show the importance of autoionizing states for the theoretical description of PADs.

Signatures of autoionization in the angular electron distribution in two-photon double ionization of Ar

S. Augustin,[1] M. Schulz,[2] G. Schmid,[1] K. Schnorr,[1] E. V. Gryzlova,[3] H. Lindenblatt,[1] S. Meister,[1]
Y. F. Liu,[1] F. Trost,[1] L. Fechner,[1] A. N. Grum-Grzhimailo,[3] S. M. Burkov,[4] M. Braune,[5] R. Treusch,[5]
M. Gisselbrecht,[6] C. D. Schröter,[1] T. Pfeifer,[1] and R. Moshammer[1]

[1]*Max-Planck-Institut für Kernphysik, Saupfercheckweg 1, 69117 Heidelberg, Germany*
[2]*Physics Department and LAMOR, Missouri University of Science and Technology, Rolla, Missouri 65409, USA*
[3]*Skobeltsyn Institute of Nuclear Physics, Lomonosov Moscow State University, Moscow, 119991 Russia*
[4]*Pacific National University, Tihookeanskaya Strasse 139, Khabarovsk 680035, Russia*
[5]*DESY, Notkestrasse 85, 22607 Hamburg, Germany*
[6]*Lund University, Sölvegatan 14A, Lund, Sweden*

A kinematically complete experiment on two-photon double ionization of Ar by free-electron laser radiation with a photon energy of 27.93 eV was performed. The electron energy spectra show that double ionization is dominated by the sequential process. Comparison of the electron angular distributions to our data for single ionization and to theory confirms that even in the sequential process the electrons from both ionization steps are correlated with each other through polarization of the intermediate Ar$^+$ state. Furthermore, a very important role of autoionization in both ionization steps is found.

I. INTRODUCTION

Until about 10 to 20 years ago experimental studies of nonlinear interactions between light and matter were limited to the relatively small photon energies of optical lasers. Synchrotron radiation has been used for a long time to study photon-atom interactions for photon energies as large as keV's [1]. However, the achievable intensities are smaller by orders of magnitudes compared to conventional lasers so that nonlinear effects are insignificant. For such large photon energies and small intensities transitions in the target atom are predominantly induced by the absorption of a single photon. One process that has been studied extensively is double ionization of the target, which for single photon absorption can only occur in the presence of strong electron-electron correlations [2–5]. With the development of free-electron lasers (FELs) [6] photon intensities comparable to conventional lasers are now available in the extreme ultraviolet and vacuum ultraviolet regime. At sufficiently large intensities two-photon double ionization (TPDI) can dominate over double ionization by single-photon absorption even when the latter is energetically possible [7].

Two different TPDI channels can be distinguished: in one, dubbed direct double ionization (DDI), two photons are absorbed simultaneously, leading to a doubly ionized final state through a virtual intermediate state. This process relies on correlation between the two active electrons. DDI has a threshold energy which is equal to half the double-ionization potential $I^{2+} = I^o + I^+$ of the target atom. The second channel, called sequential double ionization (SDI), can be viewed as two successive (and to a large extent independent) single ionization events: the absorption of one photon leads to the formation of a real intermediate state of the singly charged

ion which then absorbs a second photon, resulting in a doubly charged ion. The threshold energy for SDI is equal to the ionization potential of the singly charged ion I^+, which is larger than $1/2 I^{2+}$. Therefore, for photon energies between $1/2 I^{2+}$ and I^+ TPDI is only possible through the correlated DDI process. In this energy regime double ionization by three-photon absorption has also been observed [8]. In contrast, for photon energies larger than I^+ TPDI is dominated by SDI [7].

At first glance, one might expect that in SDI the two ionization steps are completely independent of each other. This would imply that the first electron ejected in double ionization behaves exactly like the electron ejected in single ionization of the neutral target atom and the second electron behaves like the electron ejected in single ionization of a singly charged, unpolarized target ion. For example, the angular distributions of each of the electrons ejected in double ionization, measured relative to the FEL polarization vector, would then be identical to those of the distributions of electrons ejected in the corresponding single ionization events. The latter is given in terms of the differential cross section by the standard dipole expression as

$$d\sigma_1/d\Omega = \sigma_1/4\pi[1 + \beta_2 p_2(\cos\theta)]. \tag{1}$$

Here, σ_1 is the partial photoionization cross section, P_2 is the second Legendre polynomial, and β_2 is the so-called asymmetry parameter, which is a measure of the final-state target anisotropy and is expressed in terms of photoionization amplitudes. However, it was pointed out that even in SDI the two electrons are not completely uncorrelated [9] and that Eq. (1) does not hold for the two ionization steps in SDI. The reason is that Eq. (1) only holds for an unpolarized initial target state, but the first ionization step in SDI generally

leaves the intermediate singly charged target state polarized, i.e., its magnetic substates are not populated uniformly. For example, the ground state of Ar^+, the $3p^5{}^2P_{3/2}$ state, has substates with $M_J = \pm 1/2$ and $\pm 3/2$, but the ionization cross sections for $|M_J| = 1/2$ and $3/2$ are not the same. It is not surprising that this polarization modifies the angular distribution of the second ejected electron. However, if both electrons are detected in a coincidence experiment, even when the second electron signal is integrated over all angles, the detection of the latter has a feedback effect on the first electron and its angular distribution is also modified as a result of entanglement between the first electron and the singly charged ion [9]. To illustrate this point let us consider an extreme scenario. Imagine that ionization of Ar^+ is only possible if the initial vacancy is in an $m_j = \pm 3/2$ substate, but single ionization of Ar^0 leads to a uniform population of the $m_j = \pm 1/2$ and $\pm 3/2$ substates. If both electrons ejected in SDI are detected in coincidence only electrons ejected from an $m_j = \pm 3/2$ substate in the first step will be observed because if the electron was ejected from an $m_j = \pm 1/2$ substate the second ionization step could not occur. Therefore, the polarization of the intermediate state of SDI is different from the polarization of the final state in single ionization. The corresponding modification of β_2 merely accounts for the statistical population of the intermediate substates. However, in addition for both electrons ejected in SDI a higher-order Legendre term has to be added in the angular distribution. This term is a direct reflection of entanglement between the first electron and the singly charged ion. The modified angular electron distribution can be expressed as

$$d\sigma_i/d\Omega = \sigma/4\pi[1+{}^{(i)}\beta_2 P_2(\cos\theta)+{}^{(i)}\beta_4 P_4(\cos\theta)] \quad (2)$$

where the index $i = 1, 2$ refers to the two electrons.

These predictions by theory were tested by several experimental studies [10–14] (for a review see [15]). The angular distribution of the second electron ejected in SDI from the np^6 shells of Ne, Ar, Kr, and Xe was measured for various photon energies by Braune *et al.* [10]. Generally, experiment and theory are in satisfactory agreement, although there are deviations between them in some cases. Furthermore, disagreement among various calculations [9,14,16] based on nonrelativistic and relativistic Hartree-Fock approaches and on the random-phase approximation with exchange exists. The fine-structure $np^5{}^2P_j$ doublet of the intermediate singly charged ion was considered both coherently and incoherently. To the best of our knowledge only one experiment was performed in which the angular distribution of both electrons was measured in coincidence. There, TPDI of Ne for a photon energy of 44 eV was studied by Kurka *et al.* [11]. Within the experimental uncertainties the ${}^{(2)}\beta$ parameters of both electrons were consistent with theory. However, the difference between the theoretical β parameters for a polarized and unpolarized intermediate singly charged target state was too small to be conclusively observable within the experimental error bars. Also, the ${}^{(2)}\beta_4$ parameters measured in the experiments reported in [10,11] were very different from each other, which was quite surprising considering that there was not a large difference in the photon energies.

In this paper we report on a coincidence experiment and on theoretical calculations on TPDI of Ar by an FEL pulse with a photon energy of 27.93 eV. Small but significant differences between the angular distributions of the first electron in TPDI and of the electron ejected in single ionization were established. Furthermore, the comparison between experiment and theory reveals a very important role of autoionization in each step of TPDI.

II. EXPERIMENT

The experiment was performed at the beamline BL2 of the FEL in Hamburg (FLASH). The setup was very similar to the one described in [17,18]. The FEL beam, with a photon energy of 27.93 ± 0.25 eV, was linearly polarized and pulsed with an effective repetition rate of 600 Hz and a single pulse duration of approximately 50 fs. The bandwidth is not known with high accuracy, which introduces substantial uncertainties which should be kept in mind when comparing experiment with theory. The averaged peak intensity was about 3×10^{13} W/cm^2 with an uncertainty of $\pm 2 \times 10^{13}$ W/cm^2. The beam was focused to a size of about 25 μm in diameter and crossed with a collimated neutral Ar beam from a supersonic jet with the intersection point of both beams located at the focal point. The propagation direction of the target beam was parallel to the polarization of the FEL beam.

The ejected electrons and the recoil ions were momentum-analyzed with a reaction microscope (ReMi) [19] located in an ultra-high-vacuum chamber with a base pressure of $\sim 10^{-11}$ mbar. Uniform weak electric and magnetic fields of 1.52 V/cm and 8.2 G were applied to extract the electrons and recoil ions in opposite directions along an axis perpendicular to both the photon and target beam directions to guide them onto time- and two-dimensional position-sensitive multichannel plate detectors. The recoil-ion detector, with a size of 110 mm in active diameter, consisted of two channel plates (chevron stack) and a delay-line anode with two pairs of wires (quadanode). The electron detector consisted of three channel plates (z stack) and a delay-line anode with three pairs of wires (hexanode). Both detectors were multihit capable so that two electrons ejected in the same double ionization event could be detected and momentum-analyzed. Although only one recoil ion is generated for each ionization event the multihit capability is nevertheless crucially important because of the large instantaneous recoil-ion detection rate due to the intense photon beam. Without multihit capability there would be a very large probability that a false recoil ion (i.e., one resulting from a different ionization event than the electrons), but not the true recoil ion, would be detected. Both detectors were set in coincidence.

The electric field was large enough to reverse the direction of electrons with an energy of up to 22 eV initially ejected away from the detector. The magnetic field forced the electrons into cyclotron orbits. For electron momenta perpendicular to the electric field of up to 1.35 a.u. (corresponding to an energy of 25 eV) the cyclotron radius was small enough for the electrons to be guided onto the detector. Therefore, all electrons with energies smaller than 22 eV and practically all recoil ions (because their kinetic energy was less than 200 μeV) were detected with 4π solid angle. From the position and time-of-flight information, contained in the coincidence times, all three momentum components of each detected
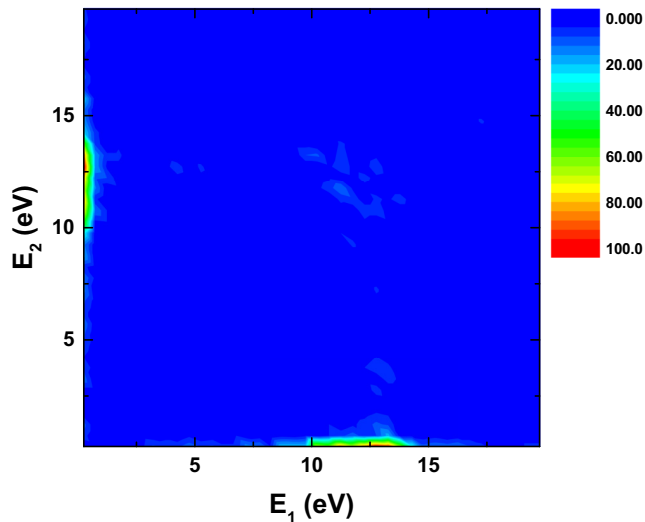
FIG. 1. Two-dimensional energy spectrum of two electrons measured in coincidence in TPDI of Ar.

particle were deduced. The electron energy resolution depends on the energy itself and is estimated to be about 0.02-eV full width at half maximum (FWHM) for the slow (second) electron and about 0.8-eV FWHM for the fast (first) electron.

III. RESULTS AND DISCUSSION

The threshold energies for DDI and sequential TPDI are 21.7 and 27.63 eV [20], respectively, so that both are energetically possible for the photon energy used in this experiment. However, the coincident two-dimensional energy spectrum of both electrons, plotted in Fig. 1, demonstrates that TPDI is completely dominated by SDI. The signature of SDI is an electron energy combination of $E_f = E_\gamma - I^o \approx 12.2$ eV and $E_s \approx E_\gamma - I^+ \approx 0.3$ eV (where E_γ is the photon energy and the subscripts stand for fast and slow, respectively), both broadened by the energy spread in the FEL beam (the energy spectrum of the fast electron is further broadened by the experimental resolution). Indeed, the two main structures are found exactly at these energy combinations. The signature of DDI, on the other hand, is $E_f + E_s = 2E_\gamma - (I^o + I^+) \approx 12.5$ eV, i.e., the diagonal line connecting the two maxima representing DSI. Virtually no intensity is found along this line illustrating that DDI is essentially absent. A very weak maximum is found for $E_1 = E_2 \approx 12$ eV (where E_1 and E_2 are the two detected electron energies), which is due to false coincidences between two single ionization events of two different Ar atoms.

Angular distributions of both ejected electrons were analyzed with a condition on the main maxima in Fig. 1 thus cleaning the SDI contributions from any background due to separate single ionization events. The angular distribution of the electron ejected in the first ionization step, measured relative to the polarization vector of the FEL light, is plotted in the left panel of Fig. 2, where the final states of the Ar$^+$ ion (i.e., the intermediate states of the TPDI process) could not be resolved. For comparison, the center panel shows the angular distribution for single ionization measured in coincidence

with Ar$^+$ ions. It should be noted that for the fast electron ejected at angles smaller than $-45°$ and larger than $45°$ it has completed nearly one cycle of the cyclotron motion generated by the magnetic field of the ReMi. In this region the electron momentum resolution is poor so that information about the ejection angle can only be obtained in the range from -45 to $45°$. Both angular distributions appear to be very similar and this is supported by fits of Eq. (2) to the measured spectra shown as black dashed curves. For single ionization this fit yields $\beta_2 = 1.4 \pm 0.035$ and $\beta_4 = -0.024 \pm 0.035$, which is consistent with the expectation that β_4 should be exactly zero for single ionization. Furthermore, these values agree very well both with theory [21] and experimental data [22,23]. For the first step of double ionization the fit yields $^{(1)}\beta_2 = 1.39 \pm 0.1$ and $^{(1)}\beta_4 = 0.13 \pm 0.11$.

Within experimental uncertainties β_2 is identical for the fast electron in SDI and single ionization. For β_4 a small difference is found, which is barely outside the error bars. The confidence level that this difference is real is less than 70% and the data cannot be regarded as conclusive in this regard. However, more significant results are obtained from the analysis of the ratios R between the angular distributions of both cases, which are shown in the right panel of Fig. 2. Since both angular distributions are recorded simultaneously under identical experimental conditions systematic uncertainties cancel to a large extent in these ratios. The data reveal a pronounced peak structure at about $90°$ and R becomes smaller than 1 on both sides of the maximum. All data points except for one depart from $R = 1$ within the statistical error bars. Furthermore, the ratio between the fits of Eq. (2) to the angular distributions (black dashed curve) agrees very well with the measured ratios. The structure in R is mainly caused by the difference in β_4; the effect due to the very small difference in β_2 would barely be visible in the plots of Fig. 2.

The blue dashed curves show our calculations, averaged over all Ar$^+$ states as described in [9,21]. The theoretical description is based on the standard statistical tensor and density matrix of angular momentum formalism [24]. This approach separates geometrical and dynamical parts in the equations describing the process, with only the latter part depending on the photoionization amplitudes. These amplitudes were calculated within first-order perturbation theory in the dipole approximation by the multiconfiguration Hartree-Fock (MCHF) approximation [25]. In the MCHF description of the ground-state wave function, we mixed the configurations $3p^m + 3p^{m-1}4s + 3p^{m-1}3d + 3p^{m-2}3d^2 + 3p^{m-2}4s3d + 3p^{m-2}4s^2$, where $m = 6$ for the neutral atom and $m = 5$ for the singly charged ion. The Hartree-Fock term-dependent $3p^m E, l$ continuum wave functions with the frozen $3p^m$ core were used for describing the final state, where E and l are the energy and orbital angular momentum of the photoelectron, respectively. The MCHF calculation yields $^{(1)}\beta_2 = 1.45$ and $^{(1)}\beta_4 = -0.08$ for the fast electron ejected in SDI and $\beta_2 = 1.35$ for single ionization. Although the differences between these theoretical parameters and those obtained from the fit to the experimental data are rather small, they nevertheless lead to some visible discrepancies in the angular distributions. The experimental ratios, on the other hand, are not even qualitatively reproduced by theory, which shows a pronounced minimum at $90°$, where
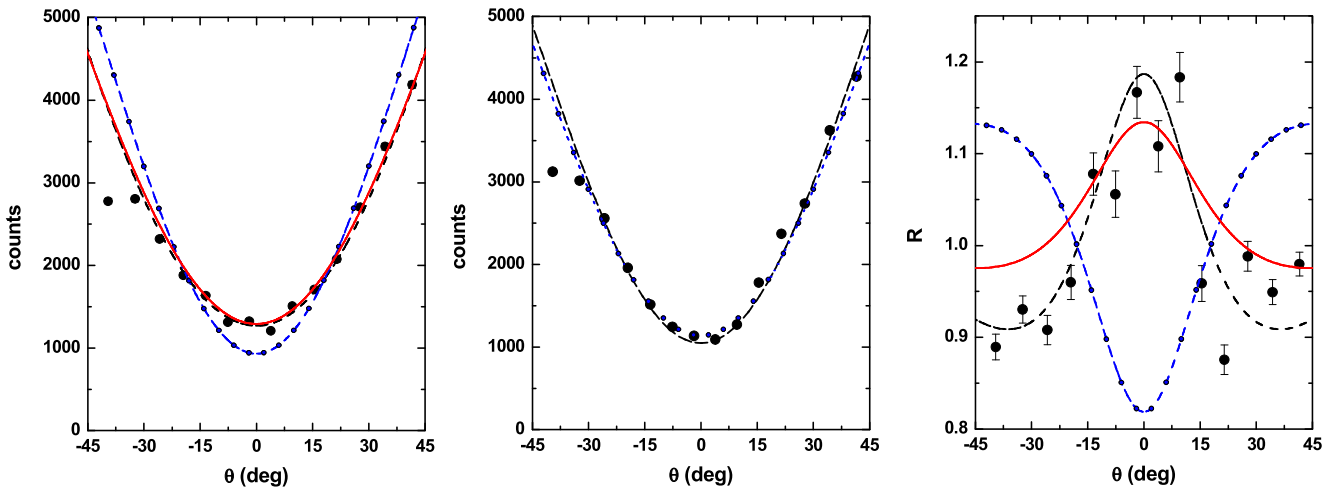
FIG. 2. Angular distribution of the fast electron ejected in the first step of TPDI (left panel) and of the electron ejected in single ionization (center panel). The right panel shows the ratio between both angular distributions. Black dashed curves, fit of Eq. (2) to the data; blue dashed curves, calculations not accounting for autoionization; red solid curves, calculations accounting for autoionization.

the measured ratios have a maximum. While theory and experiment agree that even the first electron in SDI is affected by the polarization of the intermediate state, they do not agree on how it is affected.

In the left panel of Fig. 3 we present the angular distribution of the second electron ejected in SDI averaged over all electron energies between 0 and 1 eV. For such very small energies the electrons only complete a small fraction of one cyclotron cycle so that here we obtained angular information with sufficient resolution over the entire range from -90 to $90°$. At first glance, the angular distribution of the slow electron looks quite similar to the one of the first electron. However, a fit of Eq. (2) to the measured spectrum (black dashed curves in Fig. 3) yields a substantially smaller $^{(2)}\beta_2$ parameter ($^{(2)}\beta_2 = 0.82 \pm 0.053$) for the slow electron, while the $^{(2)}\beta_4$ parameter ($^{(2)}\beta_4 = 0.06 \pm 0.07$) has, within experimental uncertainties, the same value as for the fast electron. The blue dashed curve in the left panel of Fig. 3

shows our calculation for the second electron averaged over all Ar^{2+} states, which yields $^{(2)}\beta_2 = 1.3$ and $^{(2)}\beta_4 = -0.06$. As expected, the change of the β parameters relative to those for an unpolarized intermediate state is larger than for the first electron. However, the theoretical $^{(2)}\beta_2$ parameter is in poor agreement with the experimental value.

The magnitude of the discrepancies between the experimental and theoretical value of $^{(2)}\beta_2$, as well as the poor agreement in the ratio between the angular distributions of the first electron and single ionization (Fig. 2), suggest that something qualitatively important may be missing in our theoretical model. One aspect which is not accounted for at all in the MCHF calculation is transitions of the electron to the continuum through autoionizing intermediate states. For example, instead of directly lifting the first electron to the continuum, the absorption of the first photon can lead to a transition to the $3s3p^65p\,^1P_1$ state. This is a particle-hole state with an energy (27.997 eV [20]) larger than the ground state
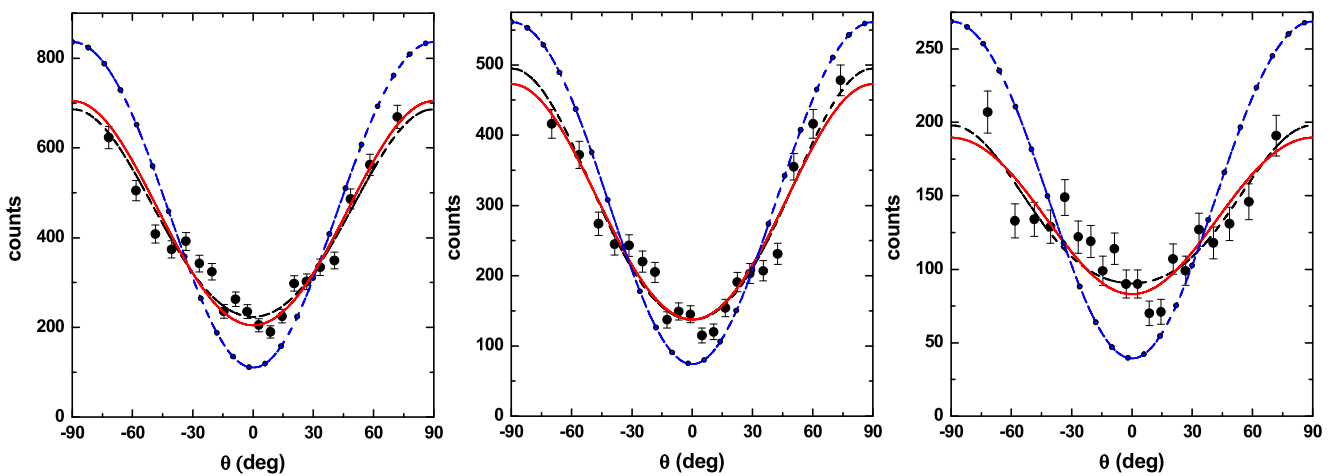
FIG. 3. Angular distribution of the slow electrons ejected in the second step of sequential two-photon double ionization averaged over all energies smaller than 1 eV (left panel). The center and right panels show the same angular distributions averaged over the energy intervals 0.2 to 0.4 eV and 0.4 to 0.6 eV, respectively. Curves: same as in Fig. 2.
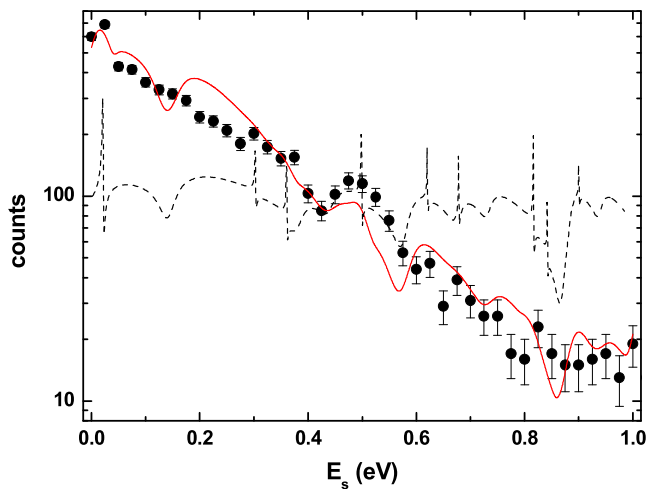
FIG. 4. Energy spectrum of the slow electron ejected in the second step of sequential TPDI. The black dashed curve shows the calculated energy spectrum not accounting for the FEL spectral profile or the electron energy resolution. The red solid curve represents the same calculation multiplied by the spectral profile and convoluted with the electron energy resolution.

FIG. 5. Electron energy dependence of the $^{(2)}\beta_2$ parameter for the electron ejected in the second step of sequential two-photon double ionization calculated with autoionization included for three different photon energies within the FEL bandwidth.

of Ar^+ and it can therefore autoionize to the $3s^2 3p^5\,{}^2 P_{1/2}$ or $3s^2 3p^5\,{}^2 P_{3/2}$ states. The excitation energy of the $3s3p^6 5p\,{}^1 P_1$ state is accessible within the FEL bandwidth of approximately ± 0.25 eV. For the second electron a multitude of Rydberg autoionizing states can contribute to the ionization of the intermediate Ar^+ ion. Such autoionizing states are known to crucially influence the angular distributions of photoelectrons in single ionization of neutral atoms by synchrotron radiation (see, e.g., [26–28]).

The energy spectrum of the second (slow) electron, plotted in Fig. 4, confirms that autoionization resonances can play an important role. The black dashed curve shows the theoretical energy spectrum incorporating the autoionizing states within the R-matrix approach (which is one standard method of incorporating autoionizing states in the theoretical treatment of photoionization) [29,30] and without accounting for the FEL bandwidth and the electron energy resolution. We performed the nonrelativistic R-matrix calculations independently for the first and the second ionization steps, the latter accounting for the alignment of the intermediate ionic state. In the calculations of the first step the states $(3p^5\,{}^2 P)$, $(3s3p^6\,{}^2 S)$, $[3p^4({}^3 P)4s\,{}^2 P]$, $[3p^4({}^3 P)3d\,{}^2 P, {}^2 D, {}^2 F]$, and $[3p^4({}^1 D)3d\,{}^2 D]$ of Ar^+ were used and for the second step the states $(3s^2 3p^4\,{}^3 P, {}^1 D, {}^1 S)$ and $(3s3p^5\,{}^1 P, {}^3 P)$ of Ar^{2+} were used. The fine structure of the residual ion was taken into account by using statistical weights of the fine-structure levels, defined by their angular momentum, and shifting the theoretical curves in accordance with experimental values of the energy splitting [20]. Six series of autoionizing states lie energetically between the $Ar^{2+}\,3p^4\,{}^3 P$ and $3p^4\,{}^1 D$ thresholds and can be excited by photoabsoption from the $Ar^+\,3p^5\,{}^2 P$ state: $(3p^4\,{}^1 D\ nd\,{}^2 D)$, $(3p^4\,{}^1 D\ nd\,{}^2 P)$, $({}^1 D\ nd\,{}^2 S)$, $(3p^4\,{}^1 D\ ns\,{}^2 D)$, $(3p^4\,{}^1 S\ nd\,{}^2 D)$, and $(3p^4\,{}^1 S\ ns\,{}^2 S)$. However, only the first two series of this list, each for $n = 6, 7, 8$, affect the energy spectrum of the slow electron in the region of interest.
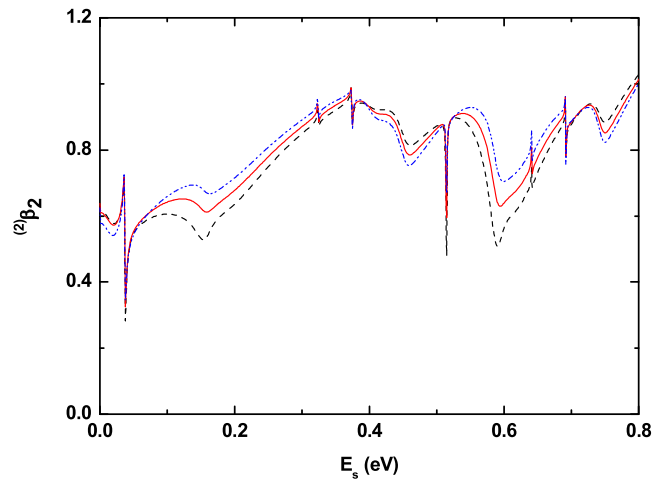
The $^2 D$ resonances are sharp and only decay by emission of d-wave electrons, while the $^2 P$ resonances are broad and decay by emission of both, s and d waves.

The resonance energies in this calculation are consistent with photoionization spectra of Ar^+ measured and calculated in the Breit-Pauli R-matrix approximation by Covington *et al.* [31]. These predicted resonances seem to coincide with corresponding structures in the experimental spectrum, most notably at an electron energy of 0.51 eV. The solid red curve shows the calculation multiplied by the spectral profile of the FEL beam, using a bandwidth of ± 0.22 eV, and convoluted with an electron energy resolution of 0.018-eV FWHM, which is in reasonably good agreement with the experimental spectrum. The values used for the FEL bandwidth and the electron energy resolution are slightly smaller than the estimated numbers provided in the experimental section. However, they yield the best agreement with the measured energy spectrum and are well within the uncertainties of these estimated values.

In Fig. 5 we show $^{(2)}\beta_2$ calculated with the autoionization resonances included as a function of the energy of the second electron. The three curves represent different photon energies within the FEL bandwidth (27.6 eV, black dashed curve; 27.9, red solid curve; and 28.2 eV, blue dash-dotted curve). The sharp structures in these plots illustrate the high sensitivity of $^{(2)}\beta_2$ on the energy of the second electron, while without accounting for autoionization the energy dependence of $^{(2)}\beta_2$ is rather smooth [9,21]. Furthermore, significant variations between different photon energies are found. Since the experimental electron energy resolution and the spread in the photon energy are significantly larger than the width of some of the structures in the theoretical $^{(2)}\beta_2$ the calculations have to be multiplied by the FEL spectral profile and convoluted with the experimental electron energy resolution.

The red solid curves in Figs. 2 and 3 show the theoretical calculations with autoionization resonances included. At first glance the changes in the β parameters of the first electron

($^{(1)}\beta_2 = 1.3$ and $^{(1)}\beta_4 = 0.05$) introduced by the inclusion of autoionization may not appear particularly significant. However, in the ratios between the angular distributions of the first electron in SDI and the electron in single ionization considerably improved agreement with the experimental data is obtained. The minimum obtained when auto-ionization is not included is now turned into a maximum, in accord with the experimental data.

At present, we cannot offer a conceptual explanation for this switch from a minimum to a maximum. However, some additional comments on the formalism might be helpful. Let us assume that a specific channel with fixed orbital angular momentum $L(L = 1, 2)$ of the final Ar^{++} state [e.g., $(3p^{4\,3}P) + e^-(\varepsilon s, \varepsilon d)$ dominates [note that $L = 0$ is forbidden in the LS-coupling approximation for the final $Ar^{++}(3p^{4\,3}P)$ state]. Furthermore, we assume that the partial cross section for the first ionization step $[Ar(3p^6) \rightarrow Ar^+(3p^5) + e^-(\varepsilon s \text{ or } \varepsilon d)]$ leading to d-wave photoelectron emission is much larger than for s-wave emission. This is fulfilled very well for our photon energy [32]. Then the procedure described in [33] leads to $^{(1)}\beta_4$ which for fixed L are just constants: $^{(1)}\beta_4^{L=1} = -\frac{108}{203}$ and $^{(1)}\beta_4^{L=2} = +\frac{108}{1057}$, where the right superscript indicates the dominant L channel. While numerical MCHF calculations without accounting for resonances and with all channels included give negative value for $^{(1)}\beta_4$, the R-matrix calculations accounting for strong autoionizing D resonances change the sign of $^{(1)}\beta_4$, which brings $^{(1)}\beta_4$ in agreement with experiment.

For the second electron the inclusion of autoionization has an even larger impact than for the first electron, especially on $^{(2)}\beta_2$, which is now smaller by about 30% ($^{(1)}\beta_2 = 0.9$). In $^{(2)}\beta_4$ the sign is reversed ($^{(2)}\beta_4 = 0.03$), as for the first electron; however, in absolute terms this difference is too small to be experimentally verifiable. These modified β parameters result in excellent agreement between the experimental and theoretical angular distributions of both electrons ejected in SDI (see Fig. 3, left panel).

As mentioned above, the inclusion of autoionization leads to pronounced structures in the electron energy dependence of the β parameters. More specifically, in the energy interval for the slow electron from 0.2 to 0.4 eV the averaged $^{(2)}\beta_2$ parameter is 0.9 and $^{(2)}\beta_4$ is 0.03, while in the interval 0.4 to 0.6 eV it changes to 0.6 and $^{(2)}\beta_4$ changes from 0.03 to -0.02. We have therefore analyzed the experimental angular

distributions for these energy intervals, which are shown in the center and right panels of Fig. 3, respectively. From these data, parameters of $^{(2)}\beta_2 = 0.94 \pm 0.06$ and $^{(2)}\beta_4 = 0.08 \pm 0.078$ for 0.2 to 0.4 eV and $^{(2)}\beta_2 = 0.56 \pm 0.075$ and $^{(2)}\beta_4 = 0.09 \pm 0.1$ for 0.4 to 0.6 eV were extracted, in very good agreement with theory.

As a final note we point out that the contributions from autoionization may also be able to explain the discrepancies in $^{(2)}\beta_4$ between the data of Braune *et al.* for Ne [10] and theory not accounting for autoionization [11,16] as well as the differences to the data of Kurka *et al.* [11] for a slightly different photon energy. For SDI of Ar at a photon energy of 27.93 eV $^{(2)}\beta_4$ remains very close to zero when autoionization is included. However, for Ne and a much larger photon energy this could be very different since the β parameters are very sensitive to both the photon energy and the atomic structure.

IV. CONCLUSIONS

In summary, we have performed a coincidence experiment on two-photon double ionization of Ar by free-electron laser radiation for a photon energy of 27.93 eV. As expected, only signatures of sequential double ionization were observed. The measured angular distributions of both photoelectrons were analyzed and compared to calculations. A theoretically predicted correlation between both electrons, resulting from the polarization of the intermediate state of the Ar^+ ion, was confirmed by the experimental data. Furthermore, the comparison between experiment and theory clearly shows the importance of autoionization resonances in both steps of sequential double ionization. This channel might also explain differences between theory and experiment as well as between two different experimental data sets reported earlier for Ne [10,11].

[1] V. Schmidt, Z. Phys. D **2**, 275 (1986).

[2] L. Avaldi and A. Huetz, J. Phys. B **38**, S861 (2005).

[3] D. Akoury *et al.*, Science **318**, 949 (2007).

[4] A. Knapp, A. Kheifets, I. Bray, T. Weber, A. L. Landers, S. Schössler, T. Jahnke, J. Nickles, S. Kammer, O. Jagutzki, L. P. Schmidt, T. Osipov, J. Rösch, M. H. Prior, H. Schmidt-Böcking, C. L. Cocke, and R. Dörner, Phys. Rev. Lett. **89**, 033004 (2002)

[5] J. Viefhaus, S. Cvejanovic, B. Langer, T. Lischke, G. Prümper, D. Rolles, A. V. Golovin, A. N. Grum-Grzhimailo, N. M. Kabachnik, and U. Becker, Phys. Rev. Lett. **92**, 083001 (2004).

[6] W. Ackermann *et al.*, Nat. Photonics **1**, 336 (2007).

[7] M. G. Makris and P. Lambropoulos, Phys. Rev. A **77**, 023401 (2008).

[8] H. Fukuzawa, E. V. Gryzlova, K. Motomura, A. Yamada, K. Ueda, A. N. Grum-Grzhimailo, S. I. Strakhova, K. Nagaya, A. Sugishima, Y. Mizoguchi, H. Iwayama, M. Yao, N. Saito, P. Piseri, T. Mazza, M. Devetta, M. Coreno, M. Nagasono, K. Tono, M. Yabashi, T. Ishikawa, H. Ohashi, H. Kimura, T. Togashi, and Y. Senba, J. Phys. B **43**, 111001 (2010).

[9] S. Fritzsche, A. N. Grum-Grzhimailo, E. V. Gryzlova, and N. M. Kabachnik, J. Phys. B **41**, 165601 (2008).

[10] M. Braune, A. Reinköster, J. Viefhaus, B. Lohmann, and U. Becker, HASYLAB Annual Report No. 457, 2007

(unpublished), http://hasyweb.desy.de/science/annual_reports/2007_report/part1/contrib/40/21686.

[11] M. Kurka, A. Rudenko, L. Foucar, K. U. Kühnel, Y. H. Jiang, T. Ergler, T. Havermeier, M. Smolarski, S. Schössler, K. Cole, M. Schöffler, R. Dörner, M. Gensch, S. Düsterer, R. Treusch, S. Fritzsche, A. N. Grum-Grzhimailo, E. V. Gryzlova, N. M. Kabachnik, C. D. Schröter, R. Moshammer, and J. Ullrich, J. Phys. B **42**, 141002 (2009).

[12] G. Hartmann, Coherence effects of diatomic homonuclear molecules and sequential two-photon processes of noble gases in the photoionization, Ph.D. thesis, Technische Universitaet Berlin (University of Technology Berlin), 2014, http://opus4.kobv.de/opus4-tuberlin/frontdoor/index/index/docId/5055.

[13] S. Mondal, R. Ma, K. Motomura, H. Fukuzawa, A. Yamada, K. Nagaya, S. Yase, Y. Mizoguchi, M. Yao, A. Rouzée, A. Hundertmark, M. J. J. Vrakking, P. Johnsson, M. Nagasono, K. Tono, T. Togashi, Y. Senba, H. Ohashi, M. Yabashi, T. Ishikawa, I. P. Sazhina, S. Fritzsche, N. M. Kabachnik, and K. Ueda, J. Phys. B **46**, 164022 (2013).

[14] M. Braune, G. Hartmann, M. Ilchen, A. Knie, T. Lischke, A. Reinköster, A. Meissner, S. Deinert, L. Glaser, O. Al-Dossary, A. Ehresmann, A. S. Kheifets, and J. Viefhaus, J. Mod. Opt. **63**, 324 (2016).

[15] A. N. Grum-Grzhimailo, E. V. Gryzlova, S. Fritzsche, and N. M. Kabachnik, J. Mod. Opt. **63**, 334 (2016).

[16] A. Kheifets, J. Phys. B **40**, F313 (2007).

[17] R. Moshammer, Y. H. Jiang, L. Foucar, A. Rudenko, T. Ergler, C. D. Schröter, S. Lüdemann, K. Zrost, D. Fischer, J. Titze, T. Jahnke, M. Schöffler, T. Weber, R. Dörner, T. J. M. Zouros, A. Dorn, T. Ferger, K. U. Kühnel, S. Düsterer, R. Treusch, P. Radcliffe, E. Plönjes, and J. Ullrich, Phys. Rev. Lett. **98**, 203001 (2007).

[18] A. Rudenko, L. Foucar, M. Kurka, T. Ergler, K. U. Kühnel, Y. H. Jiang, A. Voitkiv, B. Najjari, A. Kheifets, S. Lüdemann, T. Havermeier, M. Smolarski, S. Schössler, K. Cole, M. Schöffler, R. Dörner, S. Düsterer, W. Li, B. Keitel, R. Treusch, M. Gensch, C. D. Schröter, R. Moshammer, and J. Ullrich, Phys. Rev. Lett. **101**, 073003 (2008).

[19] J. Ullrich, R. Moshammer, A. Dorn, R. Dörner, L. Schmidt, and H. Schmidt-Böcking, Rep. Prog. Phys. **66**, 1463 (2003).

[20] *NIST Atomic Spectra Database, version 5.3*, National Institute of Standards and Technology, Gaithersburg, MD, 2015, http://physics.nist.gov/asd.

[21] A. N. Grum-Grzhimailo, E. V. Gryzlova, S. I. Strakhova, N. M. Kabachnik, and S. Fritzsche, J. Phys. Conf. Series **194**, 012004 (2009).

[22] R. G. Houlgate, J. B. West, K. Codling, and G. V. Marr, J. Phys. B **7**, L470 (1974).

[23] M. Y. Adam, P. Morin, and G. Wendin, Phys. Rev. A **31**, 1426 (1985).

[24] V. V. Balashov, A. N. Grum-Grzhimailo, and N. M. Kabachnik, *Polarization and Correlation Phenomena in Atomic Collisions: A Practical Theory Course* (Plenum, New York, 2000).

[25] C. Froese Fischer, T. Brage, and P. Jonsson, *Computational Atomic Structure: An MCHF Approach* (Institute of Physics, Bristol, 1997).

[26] D. R. Cooper, D. Cubric, D. B. Thompson, P. Bolognesi, M. C. A. Lopes, and G. C. King, J. Electr. Spectrosc. Rel. Phemon. **112**, 129 (2000).

[27] D. Dill, Phys. Rev. A **7**, 1976 (1973).

[28] J. A. R. Samson and J. L. Gardner, Phys. Rev. Lett. **31**, 1327 (1973).

[29] P. G. Burke, *R-Matrix Theory of Atomic Collisions. Application to Atomic, Molecular and Optical Processes* (Springer, Berlin, 2011).

[30] K. A. Berrington, W. B. Eissner, and P. H. Norrington, Comp. Phys. Commun. **92**, 290 (1995).

[31] A. M. Covington, A. Aguilar, I. R. Covington, G. Hinojosa, C. A. Shirley, R. A. Phaneuf, I. Álvarez, C. Cisneros, I. Dominguez-Lopez, M. M. Sant'Anna, A. S. Schlachter, C. P. Ballance, and B. M. McLaughlin, Phys. Rev. A **84**, 013413 (2011).

[32] J. R. Swanson and L. Armstrong, Jr., Phys. Rev. A **15**, 661 (1977).

[33] E. V. Gryzlova, A. N. Grum-Grzhimailo, S. Fritzsche, and N. M. Kabachnik, J. Phys. B **43**, 225602 (2010).

4.6 Further publications

During my Phd period I was involved in several beamtimes resulting in further publications. These are listed in the following. In order to get brief information about the physics and the involved people the abstract and affiliations are printed.

Terahertz-Field-Induced Time Shifts in Atomic Photoemission

Georg Schmid,[1,*] Kirsten Schnorr,[1,†] Sven Augustin,[1] Severin Meister,[1] Hannes Lindenblatt,[1] Florian Trost,[1] Yifan Liu,[1] Nikola Stojanovic,[2] Alaa Al-Shemmary,[2] Torsten Golz,[2] Rolf Treusch,[2] Michael Gensch,[3] Matthias Kübel,[4,5] Lutz Foucar,[6] Artem Rudenko,[7] Joachim Ullrich,[8] Claus Dieter Schröter,[1] Thomas Pfeifer,[1] and Robert Moshammer[1,‡]

[1]*Max-Planck-Institut für Kernphysik, Saupfercheckweg 1, D-69117 Heidelberg, Germany*
[2]*Deutsches Elektronen-Synchrotron (DESY), Notkestraße 85, D-22607 Hamburg, Germany*
[3]*Helmholtz-Zentrum Dresden-Rossendorf, Bautzner Landstraße 400, D-01328 Dresden, Germany*
[4]*Department of Physics, Ludwig-Maximilians-Universität München, D-85748 Garching, Germany*
[5]*Max-Planck-Institut für Quantenoptik, Hans-Kopfermann-Straße 1, D-85748 Garching, Germany*
[6]*Max-Planck-Institut für medizinsche Forschung, Jahnstraße 29, D-69120 Heidelberg, Germany*
[7]*Kansas State University, 116 Cardwell Hall, Manhattan, Kansas 66506, USA*
[8]*Physikalisch-Technische Bundesanstalt (PTB), Bundesallee 100, D-38116 Braunschweig, Germany*

Time delays for atomic photoemission obtained in streaking or reconstruction of attosecond bursts by interference of two-photon transitions experiments originate from a combination of the quantum mechanical Wigner time and the Coulomb-laser coupling. While the former was investigated intensively theoretically as well as experimentally, the latter attracted less interest in experiments and has mostly been subject to calculations. Here, we present a measurement of the Coulomb-laser coupling-induced time shifts in photoionization of neon at 59.4 eV using a terahertz (THz) streaking field ($\lambda = 152$ μm). Employing a reaction microscope at the THz beamline of the free-electron laser in Hamburg (FLASH), we have measured relative time shifts of up to 70 fs between the emission of $2p$ photoelectrons (∼38 eV) and low-energetic (<1 eV) photoelectrons. A comparison with theoretical predictions on Coulomb-laser coupling reveals reasonably good agreement.

Imaging multiphoton ionization dynamics of CH₃I at a high repetition rate XUV free-electron laser

Yu-Chen Cheng[1] ⓘ**, Bart Oostenrijk**[1]**, Jan Lahl**[1] ⓘ**, Sylvain Maclot**[1,2] ⓘ**,
Sven Augustin**[3,4,5] ⓘ**, Georg Schmid**[3]**, Kirsten Schnorr**[3,5]**,
Severin Meister**[3] ⓘ**, Dimitrios Rompotis**[6,7] ⓘ**, Bastian Manschwetus**[6] ⓘ**,
Harald Redlin**[6]**, Cédric Bomme**[6]**, Benjamin Erk**[6] ⓘ**, Daniel Rolles**[4,6] ⓘ**,
Rebecca Boll**[6,7] ⓘ**, Pavel Olshin**[8] ⓘ**, Artem Rudenko**[4]**, Michael Meyer**[7]**,
Per Johnsson**[1]**, Robert Moshammer**[3] **and Mathieu Gisselbrecht**[1,*] ⓘ

[1] Department of Physics, Lund University, P.O. Box 118, 22100 Lund, Sweden
[2] Department of Physics, University of Gothenburg, Origovägen 6B, 41296 Gothenburg, Sweden
[3] Max-Planck-Institut für Kernphysik, D-69117 Heidelberg, Germany
[4] J R Macdonald Laboratory, Department of Physics, Kansas State University, Manhattan, KS 66506, United States of America
[5] Paul Scherrer Institut, Forschungsstrasse 111, 5232 Villigen, Schweiz
[6] Deutsches Elektronen-Synchrotron (DESY), D-22607 Hamburg, Germany
[7] European XFEL GmbH, D-22869 Schenefeld, Germany
[8] Saint-Petersburg State University, 199034 St. Peterburg, Russia

E-mail: mathieu.gisselbrecht@sljus.lu.se

CrossMark

Abstract
XUV multiphoton ionization of molecules is commonly used in free-electron laser experiments to study charge transfer dynamics. However, molecular dissociation and electron dynamics, such as multiple photon absorption, Auger decay, and charge transfer, often happen on competing time scales, and the contributions of individual processes can be difficult to unravel. We experimentally investigate the Coulomb explosion dynamics of methyl iodide upon core–hole ionization of the shallow inner-shell of iodine (4d) and classically simulate the fragmentation by phenomenologically introducing ionization dynamics and charge transfer. Under our experimental conditions with medium fluence and relatively long XUV pulses (∼75 fs), we find that fast Auger decay prior to charge transfer significantly contributes to the charging mechanism, leading to a yield enhancement of higher carbon charge states upon molecular dissociation. Furthermore, we argue for the existence of another charging mechanism for the weak fragmentation channels leading to triply charged carbon atoms. This study shows that classical simulations can be a useful tool to guide the quantum mechanical description of the femtosecond dynamics upon multiphoton absorption in molecular systems.

Keywords: recoil-ion momentum spectroscopy, methyl iodide dissociation, sequential ionization, charge transfer, Auger decay

(Some figures may appear in colour only in the online journal)

THz Streaking of the Autoionization Dynamics of O_2 at the Free-Electron-Laser FLASH

Y.F. Liu[*,1], K. Schnorr[*], G. Schmid[*], S. Augustin[*], S. Meister[*], H. Lindenblatt[*], A. Rudenko[†],
M. Kübel[‡], C. Burger[‡], N. Stojanovic[§], R. Treusch[§], S. Düsterer[§], T. Jahnke[¶], M.F. Kling[‡],
C.D. Schröter[*], T. Pfeifer[*], R. Moshammer[*,2]

[*] Max-Planck-Institut für Kernphysik, Saupfercheckweg 1, 69117 Heidelberg, Germany
[†] J.R. Macdonald Laboratory, Kansas State University, Manhattan, 66506 Kansas, USA
[‡] Physics Department, Ludwig-Maximilians-Uniersität München, 85748 Garching, Germany
[§] Deutsches Elektronen-Synchrotron (DESY), Notkestrasse 85, 22607 Hamburg, Germany
[¶] Institut für Kernphysik, Goethe Universität, Max-von-Laue-Strasse 1, 60438 Frankfurt, Germany

Synopsis With a XUV-pump/THz-probe scheme the decay of excited O_2 cations that were produced by irradiation with XUV photons has been investigated using a Reaction Microscope (ReMi) at the free-electron-laser FLASH in Hamburg. The temporal profile of electrons emitted due to autoionization of Rydberg states $C^4\Sigma_u^- (nl\sigma_g)$ has been traced using THz streaking. This way the relaxation dynamics was followed. The relative shift in phase between photoelectrons and autoionization electrons was analyzed with respect to emission time delays or autoionization lifetimes.

Tracing charge transfer in argon dimers by XUV-pump IR-probe experiments at FLASH

Georg Schmid,[1,a] Kirsten Schnorr,[1,b] Sven Augustin,[1,b] Severin Meister,[1] Hannes Lindenblatt,[1] Florian Trost,[1] Yifan Liu,[1] Tsveta Miteva,[2,3] Mathieu Gisselbrecht,[4] Stefan Düsterer,[5] Harald Redlin,[5] Rolf Treusch,[5] Kirill Gokhberg,[2] Alexander I. Kuleff,[2] Lorenz S. Cederbaum,[2] Claus Dieter Schröter,[1] Thomas Pfeifer,[1] and Robert Moshammer[1,c]

AFFILIATIONS

[1] Max-Planck-Institut für Kernphysik, Saupfercheckweg 1, 69117 Heidelberg, Germany
[2] Theoretische Chemie, Physikalisch-Chemisches Institut, Universität Heidelberg, Im Neuenheimer Feld 229, 69120 Heidelberg, Germany
[3] Sorbonne Université, CNRS, Laboratoire de Chimie Physique Matière et Rayonnement, F-75005 Paris, France
[4] Department of Physics, Lund University, PO Box 118, SE-22100 Lund, Sweden
[5] Deutsches Elektronen-Synchrotron, Notkestraße 85, 22607 Hamburg, Germany

[a] Electronic mail: Georg.Schmid@mpi-hd.mpg.de
[b] Current address: Paul Scherrer Institut, 5232 Villigen PSI, Switzerland.
[c] Electronic mail: Robert.Moshammer@mpi-hd.mpg.de

ABSTRACT

Charge transfer (CT) at avoided crossings of excited ionized states of argon dimers is observed using a two-color pump-probe experiment at the free-electron laser in Hamburg (FLASH). The process is initiated by the absorption of three 27-eV-photons from the pump pulse, which leads to the population of Ar^{2+*}–Ar states. Due to nonadiabatic coupling between these one-site doubly ionized states and two-site doubly ionized states of the type Ar^{+*}–Ar^+, CT can take place leading to the population of the latter states. The onset of this process is probed by a delayed infrared (800 nm) laser pulse. The latter ionizes the dimers populating repulsive Ar^{2+}–Ar^+ states, which then undergo a Coulomb explosion. From the delay-dependent yields of the obtained Ar^{2+} and Ar^+ ions, the lifetime of the charge-transfer process is extracted. The obtained experimental value of (531 ± 136) fs agrees well with the theoretical value computed from Landau-Zener probabilities.

SCIENTIFIC REPORTS

natureresearch

Check for updates
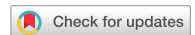
OPEN

A synchronized VUV light source based on high-order harmonic generation at FLASH

Elisa Appi[1,2,7], Christina C. Papadopoulou[3,7], Jose Louise Mapa[1,2], Nishad Wesavkar[1,2], Christoph Jusko[1,2,4], Philip Mosel[1,2,4], Skirmantas Ališauskas[3], Tino Lang[3], Christoph M. Heyl[3,5], Bastian Manschwetus[3], Maciej Brachmanski[3], Markus Braune[3], Hannes Lindenblatt[6], Florian Trost[6], Severin Meister[6], Patrizia Schoch[6], Rolf Treusch[3], Robert Moshammer[6], Ingmar Hartl[3], Uwe Morgner[1,2,4] & Milutin Kovacev[1,2,4 ✉]

Ultrafast measurements in the extreme ultraviolet (XUV) spectral region targeting femtosecond timescales rely until today on two complementary XUV laser sources: free electron lasers (FELs) and high-harmonic generation (HHG) based sources. The combination of these two source types was until recently not realized. The complementary properties of both sources including broad bandwidth, high pulse energy, narrowband tunability and femtosecond timing, open new opportunities for two-color pump-probe studies. Here we show first results from the commissioning of a high-harmonic beamline that is fully synchronized with the free-electron laser FLASH, installed at beamline FL26 with permanent end-station including a reaction microscope (REMI). An optical parametric amplifier synchronized with the FEL burst mode drives the HHG process. First commissioning tests including electron momentum measurements using REMI, demonstrate long-term stability of the HHG source over more than 14 hours. This realization of the combination of these light sources will open new opportunities for time-resolved studies targeting different science cases including core-level ionization dynamics or the electron dynamics during the transformation of a molecule within a chemical reaction probed on femtosecond timescales in the ultraviolet to soft X-ray spectral region.

A synchronized VUV beamline for time domain two-color dynamic studies at FLASH2

Elisa Appi[1,2], **Christina C. Papadopoulou**[4], **Jose Mapa**[1,2], **Nishad Wesavkar**[1,2],
Christoph Jusko[1,2,3], **Philip Mosel**[1,2,3], **Skirmantas Alisauskas**[4], **Tino Lang**[4],
Christoph M. Heyl[4,5], **Bastian Manschwetus**[4], **Markus Braune**[4], **Maciej Brachmanski**[4], **Hannes Lindenblatt**[6], **Florian Trost**[6], **Severin Meister**[6], **Patrizia Schoch**[6], **Rolf Treusch**[4], **Robert Moshammer**[6], **Ingmar Hartl**[4], **Uwe Morgner**[1,2,3], **Milutin Kovacev**[1,2,3]

1. Institut für Quantenoptik, Leibniz Universität Hannover, Hannover, 30167, Germany
2. Cluster of Excellence PhoenixD, Hannover, Germany
3.EXC 2123/1 QuantumFrontiers, Leibniz Universität Hannover, Welfengarten 1, D-30167 Hannover, Germany
4. DESY, Notkestrasse 85, Hamburg, 22607, Germany
5. Helmholtz-Institute Jena, Fröbelstieg 3 1, Jena, 07743, Germany
6. Max-Planck-Institut für Kernphysik, Saupfercheckweg 1, Heidelberg, 69117, Germany
kovacev@iqo.uni-hannover.de

Abstract: We present a HHG-based vacuum ultraviolet (VUV) source at the free electron laser FLASH2. The source provides ultrashort pulses from 10 to 40 eV, coupled to the REMI end-station (beamline FL26) for VUV-FEL pump-probe experiments. © 2020 The Author(s)

Chapter 5

Discussion and Summary

This work comprises a technical part and a physics part. The technical focus was set in the first third of this Phd project. In this period a permanent REMI endstation at FLASH2 was set up and commissioned. The main features of the REMI endstation and the REMI working principle in general, as well as the mirror chamber commissioning results were presented in the publication of section 4.1. Extensions to the endstation and three exemplary experiments were presented in the publication of section 4.2.

The physics part comprises studies of laser-dressing effects in helium (sections 4.3 and 4.4) and electron correlation effects in argon (section 4.5). In both cases FEL-XUV radiation was employed and the measurement of photoelectrons provided a detailed insight into the atomic processes.

After several years of temporarily campaigning our group at MPIK got the opportunity to set up a permanent REMI endstation at the FLASH2 (cf. publications in sections 4.1 and 4.2). While the main concept was already existing, the permanent setup enabled to implement new designs and sections which go beyond the scope of a temporary beamtime setup. A major renewal is the in-line split, delay and focusing mirror chamber which replaces the back-reflecting mirror geometry. First, the XUV beam is reflected on a split mirror where two replica of a pulse are produced. A path length difference between the replica can be introduced by moving the two mirror halves with respect to each other. This difference translates into a temporal delay between the pulses and allows to perform XUV-XUV pump-probe measurements. A second reflection takes place on an ellipsoidal mirror which focuses the beams into the REMI. Both mirrors are carbon coated and used under grazing-incidence to ensure a high reflectivity over a large XUV energy range. This is specifically beneficial at FLASH2 where the photon energy can be changed within seconds.

Two other extensions, the HHG-source [71] and the IR laser [70], were implemented in collaboration with the University of Hanover and DESY respectively. In combination with the FEL, these extensions open up a variety of radiation combinations for multicolor experiments. By harnessing the characteristic benefits of each source in a smart experimental scheme, unprecedented atomic and molecular investigations can be performed. A further, future extension will be a grating spectrometer to characterize FEL pulses on a shot-to-shot basis. The spectrometer will be installed

behind the REMI and can be used in parallel to the experiment, because the dilute gas targets do not affect the FEL beam.

Besides construction and commissioning of the endstation the papers in sections 4.1 and 4.2 explain the measuring scheme of the REMI. They cover the target preparation, the working principle of the detectors and the spectrometer and the data acquisition. Furthermore they give detailed information on the setup, like dimensions, geometries and vacuum conditions, which are not given in the physics publications in sections 4.3 to 4.5.

In the following, the two publications in sections 4.3 and 4.4 are discussed together, as both are based on the same experiment. In both studies laser-dressing and multi-photon effects in atomic helium are investigated. This is achieved by the combined interaction of XUV and IR radiation which allows to couple to excited states of various quantum numbers n, l, m. These states are referred to, depending on the context, as dark or light-induced states and are investigated for varying XUV photon energy, IR intensity and light polarization.

In a first simple scenario the XUV pulses precede the IR pulses. For matching XUV photon energies the helium atom can be excited from the $1s^2\,^1S$ ground state to $1snp\,^1P$ excited states. The subsequent absorption of IR photons ionizes the excited atom and the emitted photoelectrons are measured. Their energy and angular distribution allows not only to determine the number of absorbed IR photons, but also the share of outgoing S, P, D etc. continuum waves. Detailed investigations with this scheme have been performed with synchrotron radiation [76], HHG radiation [79, 36, 80] and FEL radiation [77]. In these studies helium atoms were excited to $1snp\,^1P$ states by an XUV pulse and ionized by a subsequent IR laser pulse of mostly 800 nm. They analyzed phase shift differences and ratios of the outgoing S and D continuum waves.

Here we focus on the different situation of temporally overlapping pulses where the XUV and IR radiation are simultaneously available. A combination of one XUV photon and IR photons can populate excited states of helium which are not accessible by single-photon absorption. The helium atom is said to be "dressed" in the laser field where it can absorb and emit IR photons. Both processes are described in section 4.3 where ionization via the $1s3d\,^1D$ (abbreviated as $3d$) state and via the $1s2s\,^1S$ (abbreviated as $2s$) state is observed. In the first case the excitation involves the combined absorption of one XUV photon and one IR photon:

$$He\,(1s^2\,^1S) + \gamma_{\mathsf{XUV}}(21.8\,\mathrm{eV}) + \gamma_{\mathsf{IR}}(1.55\,\mathrm{eV}) \Rightarrow He^*\,(1s3d\,^1D), \qquad (5.1)$$
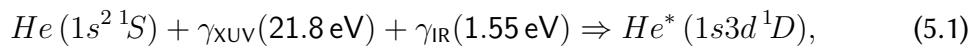
while in the second case one XUV photon is absorbed and one IR photon is emitted:

$$He\,(1s^2\,^1S) + \gamma_{\mathsf{XUV}}(22.4\,\mathrm{eV}) - \gamma_{\mathsf{IR}}(1.55\,\mathrm{eV}) \Rightarrow He^*\,(1s2s\,^1S). \qquad (5.2)$$
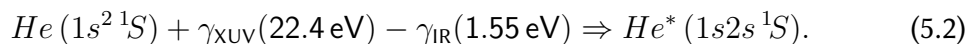
Where it has to be noted that the given excitation energies are Stark-shifted and therefore do not exactly match the field-free levels listed in NIST [78].

As mentioned before, similar investigations were performed in transient absorption (TA) measurements where these multi-color multiphoton excited states were denoted as light-induced states (LIS) [21, 81, 73, 72]. In TA light is transmitted through a dense gas target and spectrally analyzed. The specified publications employed broadband XUV pulses generated by an HHG source. In combination with the intrinsically synchronized IR radiation LIS where observed as absorption features for temporally overlapping pulses. These measurements can be seen as complementary to the approach in this thesis. While absorption features emerge without a following ionization, photoelectron measurements require ionization to take place. This leads to an additional laser intensity dependence, as the number of ionizing IR photons can vary for different excited states. These factors make a direct comparison of the two experimental techniques tentative. Nevertheless TA measurements find the same dominant LIS at comparable excitation energies than in the presented investigation (cf. ref. [74]). While the assignment of LIS in TA is exclusively based on excitation energies, photoelectrons additionally carry information of the state they where emitted from. This allows in some cases a more reliable assignment of these states.
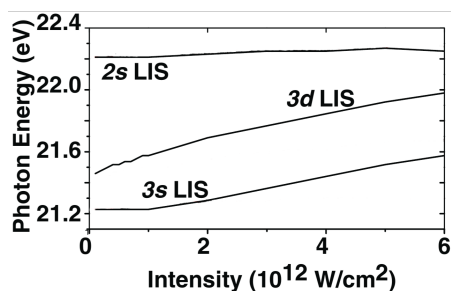
figure 5.1: *Level shifts calculated by Chen et. al. Adopted from [75]*

Besides assignments of the states their laser intensity dependence is analyzed. The $3d$ excitation peak for example (cf. section 4.3 figure 3) is shifted from 21.8 eV at about $1 \times 10^{12}\,\mathrm{W\,cm^{-2}}$ to 22.4 eV at about $8 \times 10^{12}\,\mathrm{W\,cm^{-2}}$. This comparably large shift is reproduced by the calculation provided in section 4.3 and by the calculation of Chen et. al [75]. In contrast, the $2s$ state exhibits a shift below the experimental precision. Theory of this work also predicts only a minor shift, as well as the calculation depicted in figure 5.1. This is also in accordance with the tendency of a more pronounced Stark shift with increasing principal quantum number n [82].

Another laser intensity depended effect is the relative strength of LIS peaks. While for low IR intensities in the experiment the $3d$ peak is dominating, at high intensities the $2s$ peak exhibits a considerable contribution. This is owed to the fact that the number of absorbed IR photons differs in both cases. Ionizing an atom in the $3d$ state requires the absorption of one additional IR photon, while the low lying $2s$ state requires the absorption of three IR photons. In total we are dealing with an effective

two- and four-photon transition when the IR photon of the excitation is included as well. The transition rate R in multiphoton processes follows the scaling law: $R \propto I^N$, where I denotes the laser intensity and N the number of photons ([22] p.266). The observation that higher order processes become more relevant with increasing intensity is in accordance with the scaling law. For the absolute scaling of the peaks however, one also has to consider the transition probability of each individual state. We also report on the ionization via the $1s4f\,^1F$ state where the excitation already involves three photons. The absorption of one XUV and two IR photons excites the atom and the absorption of one additional IR photon leads to ionization.

A further investigated aspect is the polarization dependence of the two-color multi-photon excited states. Both the XUV and the IR radiation is linearly polarized and can be rotated with respect to each other. For parallel orientation of polarizations the magnetic quantum number m is conserved in a transition. For other orientations however, this is no longer the case. It gets evident by assuming the IR polarization to define the quantization axis. In this basis the XUV radiation can be expressed in a superposition of left and right circularly polarized light, which involve a change of $\Delta m = \pm 1$ in a transition. The change of m in LIS upon the orientation of polarization axes is experimentally demonstrated in section 4.4. A detailed analysis is done for ionization via the $3d$ state. For parallel orientation the PAD exhibits an axial symmetry around the polarization axes and resembles a hydrogen orbital with $\ell = 3$ and $m = 0$. For orthogonal orientation the PAD changes completely and resembles a hydrogen orbital with $\ell = 3$ and $m = \pm 1$. In fact the PAD is the absolute square of the superposition of the two final continuum states $|l, m\rangle = |3, 1\rangle$ and $|3, -1\rangle$ [72]. The PAD can be reproduced to good precision by numerically solving the Schrödinger equation for a helium atom irradiated with XUV and IR pulses. In section 4.4 III B a direct comparison of experimental and theoretical PADs is given for two different states.

Moreover, polarization can be used as a switch for photoionization to occur. This is demonstrated in section 4.4 III A for the $2s$ state. At XUV energies of 22.3 eV and parallel polarization axes the ground state $1s^2\,^1S$ can be coupled to the $1s2s\,^1S$ excited state by the absorption of an XUV photon and the simultaneous emission of an IR photon. The ionization yield via this state can be suppressed by rotating the polarization axes to orthogonal orientation while keeping all other parameters in place. In this case the coupling between the two S-states ($L = 0$) is forbidden by the two photon dipole selection rules. There is again a straightforward explanation for this observation. The orthogonal orientation implies a change of $\Delta m = \pm 1$ and therefore a target state with $m = \pm 1$, which however is not available for S-states. As a result there is no resonance enhancement via the $2s$ state for orthogonal polarization axes. This behavior can also serve as a test to distinguish S-states from others. In the presented example the S-state vanishes while the D-state remains upon rotation of the polariza-

tion. Analogous findings are reported by Reduzzi *et. al* [72] in a transient absorption scheme employing a broadband XUV pulse of a HHG-source. In combination with the driving IR laser they revealed several LIS in helium. For parallel polarization they find the $2s$ and the $3d$ LIS to dominate in the energy region between the $1s2p\,^1P$ and the $1s3p\,^1P$ state (21.2 eV–23.1 eV). In accordance with our investigation they observe for orthogonal polarization the $2s$ LIS to vanish and the $3d$ LIS to persist.

Experiments which are based on HHG-XUV radiation observe oscillations in transient absorption [73, 83] features or photoelectron yields [84], which is not the case in the presented investigation. These oscillations manifest along the delay between XUV and IR pulses and arise from two-path interference, quantum optical interference or quantum beating. In short, interference occurs due to the combination of broadband XUV and IR radiation which enables multiple excitation or ionization pathways resulting in the same quantum state. In two-path interference for example an atom can be ionized via two different pathways which both yield photoelectrons of the same continuum state. The XUV can either directly ionize an atom from the ground state or just excite the atom while a following absorption of two IR photons leads to ionization.

These effects are not observed in the presented investigation for two reasons. First, FEL-XUV radiation does not exhibit spectral bandwidths as large as HHG-XUV radiation can do (example values: $\Delta E_{\text{FEL}} \approx 0.1$ eV [85], $\Delta E_{\text{HHG}} \approx 10$ eV [84]). This reduces the number of possible scenarios where two pathways lead to the same outcome. Second, the FEL-XUV and IR radiation are not intrinsically synchronized like in the HHG case. Therefore, our experiment in sections 4.3 and 4.4 is subject to a temporal jitter between pulses and no constant phase relation can be achieved. This blurs out any interference patterns in our experiment which relies on counting independent events. The last section of this investigation focuses on the laser-intensity dependence of PADs and its implications on the underlying ionization mechanism. For this, we consider photoelectrons which were ionized by the two temporally overlapping radiation fields, were the XUV photon energy was tuned to the $1s2p\,^1P$ resonance (21.2 eV). The angular distribution exhibits the form of a G continuum wave, which is explained by the dominant absorption of one XUV photon and three IR photons from the S ground state. This distribution changes distinctively by increasing the laser intensity from $1 \times 10^{12}\,\text{W\,cm}^{-2}$ to $8 \times 10^{12}\,\text{W\,cm}^{-2}$. At high intensity minima and maxima at around $\cos(\Theta) = \pm 0.8$ level out, which is quantified in the β asymmetry parameters and reproduced by the TDSE calculation. This can be explained by higher order effects which come into play at higher intensities. In addition to the aforementioned involved photons, one IR photon can be absorbed and re-emitted. This leaves the photoelectron energy unchanged, but alters the PAD. For even larger laser intensities one would have to consider also higher terms of absorption and emission, blurring the PAD even more. In the extreme, high-intensity case the classical picture gets applicable where electrons are predominantly emitted along the polarization direction and PADs show

no distinctive features anymore. Our investigation shows the onset of this transition from the multiphoton regime to the tunnel regime.

From the results and the experimental challenges of the presented investigation several improvements, extensions and successive experiments were figured out. To start from the technical side, it would be beneficial to improve the energy resolution in order to distinguish nearby features when scanning the XUV photon energy. The feature size in the $E\gamma$-plots is predominantly determined by the radiation sources and not by the detector resolution. Improvement can be realized in several ways. One can employ a monochromator beamline or a seeded FEL to strongly reduce the XUV bandwidth. This would narrow down the horizontal spread in the $E\gamma$-plots of section 4.4. In order to handle the SASE owed shot-to-shot fluctuations, a post-experiment sorting can be implemented by means of an XUV spectrometer. If the XUV radiation is spectrally analyzed on a single shot basis, one can determine the mean photon energy and sort photoelectron events accordingly. The other potential candidate for improvements is the IR laser. The photoelectron energy spread is mainly determined by the IR radiation, as it is solely responsible for the ionization out of the discrete excited states. Here special care has to be taken for chirps on the IR pulse which lead to broad photoelectron peaks.

Another broadening contribution arises from the temporal jitter between XUV and IR pulses. Depending on the relative delay, ionization can take place at the rising edge or in the maximum of the IR pulse, or at any other intermediate situation. As a consequence, atoms experience a variety of laser intensities which leads to varying Stark and ponderomotive shifts and finally to a peak broadening.

From a physical point of view it would be interesting to extend the presented scheme on more complex targets and light-induced processes. The large XUV energy scanning range allows to track the opening and closing of ionization channels and gives a detailed overview. This can be especially beneficial for molecules which exhibit complex potential energy surfaces and (ro)-vibronic transitions. Certain states which are only detectable in a multiphoton scheme can be revealed and exhibit a decisive role in photochemistry and other radiationless processes [86]. Furthermore, the combination of XUV and IR radiation enables a less perturbed investigation as the XUV photon delivers the main energy contribution for excitation. In this way, less intense fields can by employed compared to purely long-wavelength schemes. The large photon energy would also allow to perform REMPI like measurements in higher charged cationic atoms, molecules and clusters [87]. These exhibit large excitation energies which are not accessible with optical or IR radiation. Moreover, our scheme can contribute to the more recent investigation on light-induced conical intersections in molecules [88, 89]. Here, the dressing laser field can couple electronic states and create a concical intersection during the time being applied. Additionally scanning the XUV energy with a variable delay towards the IR can be used to pump or probe

population across such an intersection while receiving dynamical information.

Similar to the previous investigations the fifth publication deals with multiphoton effects and angular distributions of photoelectrons. In contrast, the target being employed is argon in a single-color XUV radiation scheme. We investigate the correlation of the two emitted electrons in two-photon double ionization (TPDI). Intense FEL-XUV radiation allows the absorption of two photons within the same atom. The chosen photon energy ($E_\gamma = 27.93$ eV) is above the ionization threshold of Ar^+ ($I^+ = 27.63$ eV). This opens up the channel for sequential double ionization, which is found to be the dominant channel. Experimentally this manifests in photoelectron kinetic energies accumulating at $E_f = E_\gamma - I^0 \approx 12.2$ eV from the first electron and at $E_s = E_\gamma - I^+ \approx 0.3$ eV from the second electron. In principal the channel of direct double ionization is also accessible. This however is not found in the data where it would yield a continuous energy sharing between electrons with a sum energy of $E_f + E_s = 2E_\gamma - (I^0 + I^+) \approx 12.5$ eV.

The PAD of the first electron in TPDI is found to differ from the one in single ionization. At first glance this seems surprising as the stepwise character of sequential double ionization suggests the first ionization to be independent of the second. However, the two electrons in TPDI are found to be correlated by the polarization of the intermediate Ar^+ state, which pre-selects TPDI processes by its orientation. Consequently the first emitted electron in TPDI experiences modifications of its angular distribution compared to an electron of single ionization. The subtle differences get apparent by displaying the quotient of both PADs (cf.section 4.5 Fig.2). Furthermore, systematic errors are canceled for the most part as both channels are recorded simultaneously under the same experimental conditions. The standard theoretical description of the multi-configuration Hartree-Fock (MCHF) approximation does not reproduce the measured quotient of PADs, not even qualitatively. It is found that autoionizing states in the Ar and Ar^+ continuum play a crucial role in the description of PADs in TPDI. Due to the bandwidth of the FEL (≈ 0.25 eV) several of these states are in reach. They are accounted for within the R-matrix approach which describes the measured PAD satisfactorily. The missing consideration of autoionizing states might be the key point why theory and experiment in previous studies exhibited discrepancies [90]. A very recent study, building upon our investigation, performed an analogous experiment in krypton [91]. They also confirmed a more complete description of TPDI by including autoionizing states. Furthermore, they could resolve the finestructure in the intermediate Kr^+ ion and to some extend in the Ar^{2+} ion, which was not possible in the presented study. Further related investigations, which were published subsequently to ours, were performed on sequential TDPI in neon [92] and neon/argon [93] with the seeded FERMI at Elettra. Here, the energy resolution allowed not only to distinguish finestructure levels, but also to follow the change of asymmetry parameters

with photon energy over an autoionizing resonance. There is also an extended theoretical investigation by Gryzlova *et al.* [94] directly referring to our experiment and in the same energy range. Besides reproducing our experimental findings, they provide cross-sections and asymmetry parameters and also angular correlation functions for the two emitted electrons.

The only experiment recording an angular correlation function, i.e. PADs for both photoelectrons in coincidence, was performed in neon by Kurka *et al.* [95]. The angular correlation encodes the effect of the alignment of the intermediate state, as well as the influence of autoionizing states for both the neutral atom and the singly charged ion. The experiment however lacks of statistical significance and the bandwidth of the FEL-XUV radiation was too large to distinguish the different autoionizing states. Improving on these two points can be seen as an experimental outlook to test theory-based angular correlations for example from Gryzlova *et al.* [94] and to gain a more complete insight into the process.

An interesting variant of our study can be the implementation of a pump-probe scheme. Irradiating the target atom with two XUV pulses of variable delay allows to temporally separate the photoabsorption steps in TPDI. For a sufficiently short pump pulse, i.e. a bandwidth which is larger than the finestructure splitting in the intermediate state, quantum beating can be triggered. The angular distribution of the second electron is then found to be a function of the delay. Moreover, in this scheme the depolarization of the intermediate state can be analyzed.

It was demonstrated how the presented results make a contribution to current field of research. This was rendered possible by the combination of FEL-XUV radiation, IR laser radiation and sophisticated momentum spectroscopy. Moreover, successive investigations which were triggered by our findings were discussed. The stated open questions and new ideas will be tackled in upcoming beamtimes supported by technical improvements. The synchronization of FEL and IR laser was recently improved by an order of magnitude, which allows investigations of fast dynamics. Furthermore, funnel micro channel plates increase the detection efficiency, were especially multi-particle coincidence measurements can benefit from. In addition, the newly implemented HHG-source will have its first beamtime in combination with the FEL. This unique composition will enable unprecedented investigations and increase the versatility of the REMI endstation.

Über die letzten vier Jahre hinweg habe ich mit vielen Menschen zusammengarbeitet und Zeit verbracht, wofür sich sehr dankbar bin. Einigen möchte ich im Speziellen danken:

Robert, dessen Rat ich immer einholen konnte. Seine Mischung aus Pragmatismus und Humor waren immer gute Wegbegleiter.

Thomas, der immer ansprechbar war und mit seinem Optimismus stets für gute Stimmung sorgte

meinen ehemaligen Kollegen Georg, Kirsten und Sven, von denen ich viel lernen konnte und mit denen ich viele aufregende und lustige Zeiten in Hamburg hatte.

Claus-Dieter für sein unerschöpfliches Detailwissen und die Unterstützung in technischen und philosophischen Fragen.

Hannes und Florian mit denen ich die REMI endstation betreue. Danke für die Kurzweiligkeit in anstrengenden Phasen und das gute Arbeitsklima!

Frans danke ich für Vieles, aber an dieser Stelle hat es leider für nichts gereicht!

unseren Mechanikern, allen voran Christian Kaiser, Bernd Knape und Alexander von der Dellen, die mit viel Geschick und Pragmatismus stets zur Seite standen.

Frans danke ich für den Spaß an der Freud!

John danke ich dafür jeden Tag am Elfenbeinturm gesägt zu haben.

Ein Dank auch an meine Eltern, auf die ich immer zählen kann.

... und zu guter Letzt ein riesen Dank an Marieke, die mir in jeder Situation zur Seite steht!

Bibliography

[1] G. Öhrwall, M. Tchaplyguine, M. Lundwall, R. Feifel, H. Bergersen, T. Rander, A. Lindblad, J. Schulz, S. Peredkov, S. Barth, S. Marburger, U. Hergenhahn, S. Svensson, and O. Björneholm. Femtosecond Interatomic Coulombic Decay in Free Neon Clusters: Large Lifetime Differences between Surface and Bulk. *Phys. Rev. Lett.*, 93:173401, Oct 2004.

[2] K. Schnorr, A. Senftleben, M. Kurka, A. Rudenko, L. Foucar, G. Schmid, A. Broska, T. Pfeifer, K. Meyer, D. Anielski, R. Boll, D. Rolles, M. Kübel, M. F. Kling, Y. H. Jiang, S. Mondal, T. Tachibana, K. Ueda, T. Marchenko, M. Simon, G. Brenner, R. Treusch, S. Scheit, V. Averbukh, J. Ullrich, C. D. Schröter, and R. Moshammer. Time-Resolved Measurement of Interatomic Coulombic Decay in Ne_2. *Phys. Rev. Lett.*, 111:093402, Aug 2013.

[3] D. Iablonskyi, K. Nagaya, H. Fukuzawa, K. Motomura, Y. Kumagai, S. Mondal, T. Tachibana, T. Takanashi, T. Nishiyama, K. Matsunami, P. Johnsson, P. Piseri, G. Sansone, A. Dubrouil, M. Reduzzi, P. Carpeggiani, C. Vozzi, M. Devetta, M. Negro, F. Calegari, A. Trabattoni, M. C. Castrovilli, D. Faccialà, Y. Ovcharenko, T. Möller, M. Mudrich, F. Stienkemeier, M. Coreno, M. Alagia, B. Schütte, N. Berrah, A. I. Kuleff, G. Jabbari, C. Callegari, O. Plekan, P. Finetti, C. Spezzani, E. Ferrari, E. Allaria, G. Penco, C. Serpico, G. De Ninno, I. Nikolov, B. Diviacco, S. Di Mitri, L. Giannessi, K. C. Prince, and K. Ueda. Slow Interatomic Coulombic Decay of Multiply Excited Neon Clusters. *Phys. Rev. Lett.*, 117:276806, Dec 2016.

[4] He Wang, Michael Chini, Shouyuan Chen, Chang-Hua Zhang, Feng He, Yan Cheng, Yi Wu, Uwe Thumm, and Zenghu Chang. Attosecond Time-Resolved Autoionization of Argon. *Phys. Rev. Lett.*, 105:143002, Oct 2010.

[5] Ahmed H. Zewail. Femtochemistry: Atomic-Scale Dynamics of the Chemical Bond. *The Journal of Physical Chemistry A*, 104(24):5660–5694, Jun 2000.

[6] Benedikt Rudek, Sang-Kil Son, Lutz Foucar, Sascha W. Epp, Benjamin Erk, Robert Hartmann, Marcus Adolph, Robert Andritschke, Andrew Aquila, Nora Berrah, et al. Ultra-efficient ionization of heavy atoms by intense X-ray free-electron laser pulses. *Nature Photonics*, 6(12):858–865, Dec 2012.

[7] L S Vasilenko, V P Chebotaev, and A U Shishaev. Line shape of two-photon absorption in a standing-wave field in a gas. *JETP Lett.*, 12(3):161–165, 1970.

[8] C. Wieman and T. W. Hänsch. Doppler-Free Laser Polarization Spectroscopy. *Phys. Rev. Lett.*, 36:1170–1173, May 1976.

[9] N. K. Berezhetskaya, G. S. Voronov, G. A. Delone, N. B. Delone, and G. K. Piskova. Effect of a Strong Optical-frequency Electromagnetic Field on the Hydrogen Molecule. *Soviet Journal of Experimental and Theoretical Physics*, 31:403, January 1970.

[10] S. L. Chin. Multiphoton Ionization of Molecules. *Phys. Rev. A*, 4:992–996, Sep 1971.

[11] W. Martin McClain. Two-photon molecular spectroscopy. *Accounts of Chemical Research*, 7(5):129–135, May 1974.

[12] L. V. KELDYSH. Ionization in the field of a strong electromagnetic wave. *Sov. Phys. JETP.*, 20:1307–1314, 1965.

[13] N B Delone and Vladimir P Krainov. AC Stark shift of atomic energy levels. *Physics-Uspekhi*, 42(7):669–687, jul 1999.

[14] A M Bonch-Bruevich, N N Kostin, V A Khodovoi, and V V Khromov. Changes in the atomic absorption spectrum in the field of a light wave. *Soviet Physics JETP*, 29(1):144–150, jul 1969.

[15] NASA Inductiveload. Em spectrum properties. Wiki Commons, CC BY-SA 3.0, Feb. 2021.

[16] E. Goulielmakis, M. Schultze, M. Hofstetter, V. S. Yakovlev, J. Gagnon, M. Uiberacker, A. L. Aquila, E. M. Gullikson, D. T. Attwood, R. Kienberger, F. Krausz, and U. Kleineberg. Single-Cycle Nonlinear Optics. *Science*, 320(5883):1614–1617, 2008.

[17] J. J. Macklin, J. D. Kmetec, and C. L. Gordon. High-order harmonic generation using intense femtosecond pulses. *Phys. Rev. Lett.*, 70:766–769, Feb 1993.

[18] Tenio Popmintchev, Ming-Chang Chen, Dimitar Popmintchev, Paul Arpin, Susannah Brown, Skirmantas Ališauskas, Giedrius Andriukaitis, Tadas Balčiunas, Oliver D. Mücke, Audrius Pugzlys, Andrius Baltuška, Bonggu Shim, Samuel E. Schrauth, Alexander Gaeta, Carlos Hernández-García, Luis Plaja, Andreas Becker, Agnieszka Jaron-Becker, Margaret M. Murnane, and Henry C. Kapteyn. Bright Coherent Ultrahigh Harmonics in the keV X-ray Regime from Mid-Infrared Femtosecond Lasers. *Science*, 336(6086):1287–1291, 2012.

[19] B. Dromey, S. Kar, C. Bellei, D. C. Carroll, R. J. Clarke, J. S. Green, S. Kneip, K. Markey, S. R. Nagel, P. T. Simpson, L. Willingale, P. McKenna, D. Neely, Z. Najmudin, K. Krushelnick, P. A. Norreys, and M. Zepf. Bright Multi-keV Harmonic Generation from Relativistically Oscillating Plasma Surfaces. *Phys. Rev. Lett.*, 99:085001, Aug 2007.

[20] Eberhard J. Jaeschke, Shaukat Khan, Jochen R. Schneider, and Jerome B. Hastings. *Synchrotron Light Sources and Free-Electron Lasers.* Springer, Cham, 2016.

[21] Shaohao Chen, M. Justine Bell, Annelise R. Beck, Hiroki Mashiko, Mengxi Wu, Adrian N. Pfeiffer, Mette B. Gaarde, Daniel M. Neumark, Stephen R. Leone, and Kenneth J. Schafer. Light-induced states in attosecond transient absorption spectra of laser-dressed helium. *Phys. Rev. A*, 86:063408, Dec 2012.

[22] Ingolf Volker Hertel and Claus-Peter Schulz. *Atome, Moleküle und optische Physik 1.* Springer Spektrum, Berlin, Heidelberg, 2017.

[23] Keith D. Bonin and Thomas J. McIlrath. Two-photon electric-dipole selection rules. *J. Opt. Soc. Am. B*, 1(1):52–55, Mar 1984.

[24] H. A. Bethe and E. E. Salpeter. *Quantum Mechanics of One- and Two-Electron Systems*, pages 88–436. Springer Berlin Heidelberg, Berlin, Heidelberg, 1957.

[25] P. Agostini, F. Fabre, G. Mainfray, G. Petite, and N. K. Rahman. Free-Free Transitions Following Six-Photon Ionization of Xenon Atoms. *Phys. Rev. Lett.*, 42:1127–1130, Apr 1979.

[26] Y Gontier, M Poirier, and M Trahin. Multiphoton absorptions above the ionisation threshold. *Journal of Physics B: Atomic and Molecular Physics*, 13(7):1381–1387, apr 1980.

[27] A. A. Sorokin, S. V. Bobashev, T. Feigl, K. Tiedtke, H. Wabnitz, and M. Richter. Photoelectric Effect at Ultrahigh Intensities. *Phys. Rev. Lett.*, 99:213002, Nov 2007.

[28] A. Rudenko, L. Foucar, M. Kurka, Th. Ergler, K. U. Kühnel, Y. H. Jiang, A. Voitkiv, B. Najjari, A. Kheifets, S. Lüdemann, T. Havermeier, M. Smolarski, S. Schössler, K. Cole, M. Schöffler, R. Dörner, S. Düsterer, W. Li, B. Keitel, R. Treusch, M. Gensch, C. D. Schröter, R. Moshammer, and J. Ullrich. Recoil-Ion Momentum Distributions for Two-Photon Double Ionization of He and Ne by 44 eV Free-Electron Laser Radiation. *Phys. Rev. Lett.*, 101:073003, Aug 2008.

[29] R. Moshammer, Y. H. Jiang, L. Foucar, A. Rudenko, Th. Ergler, C. D. Schröter, S. Lüdemann, K. Zrost, D. Fischer, J. Titze, T. Jahnke, M. Schöffler, T. Weber, R. Dörner, T. J. M. Zouros, A. Dorn, T. Ferger, K. U. Kühnel, S. Düsterer, R. Treusch,

P. Radcliffe, E. Plönjes, and J. Ullrich. Few-Photon Multiple Ionization of Ne and Ar by Strong Free-Electron-Laser Pulses. *Phys. Rev. Lett.*, 98:203001, May 2007.

[30] L. Young, E. P. Kanter, B. Krässig, Y. Li, A. M. March, S. T. Pratt, R. Santra, S. H. Southworth, N. Rohringer, L. F. DiMauro, G. Doumy, C. A. Roedig, N. Berrah, L. Fang, M. Hoener, P. H. Bucksbaum, J. P. Cryan, S. Ghimire, J. M. Glownia, D. A. Reis, J. D. Bozek, and M. Bostedt, C.and Messerschmidt. Femtosecond electronic response of atoms to ultra-intense X-rays. *Nature*, 466(7302):56–61, Jul 2010.

[31] H. Fukuzawa, S.-K. Son, K. Motomura, S. Mondal, K. Nagaya, S. Wada, X.-J. Liu, R. Feifel, T. Tachibana, Y. Ito, M. Kimura, T. Sakai, K. Matsunami, H. Hayashita, J. Kajikawa, P. Johnsson, M. Siano, E. Kukk, B. Rudek, B. Erk, L. Foucar, E. Robert, C. Miron, K. Tono, Y. Inubushi, T. Hatsui, M. Yabashi, M. Yao, R. Santra, and K. Ueda. Deep Inner-Shell Multiphoton Ionization by Intense X-Ray Free-Electron Laser Pulses. *Phys. Rev. Lett.*, 110:173005, Apr 2013.

[32] A. A. Sorokin, M. Wellhöfer, S. V. Bobashev, K. Tiedtke, and M. Richter. X-ray-laser interaction with matter and the role of multiphoton ionization: Free-electron-laser studies on neon and helium. *Phys. Rev. A*, 75:051402, May 2007.

[33] P. Lambropoulos, L. A. A. Nikolopoulos, and M. G. Makris. Signatures of direct double ionization under xuv radiation. *Phys. Rev. A*, 72:013410, Jul 2005.

[34] Katharine L. Reid. Photoelectron Angular Distributions. *Annual Review of Physical Chemistry*, 54(1):397–424, 2003. PMID: 12574491.

[35] J. Cooper and R. N. Zare. Angular Distribution of Photoelectrons. *The Journal of Chemical Physics*, 48(2):942–943, 1968.

[36] Nicola Mayer, Peng Peng, David M Villeneuve, Serguei Patchkovskii, Misha Ivanov, Oleg Kornilov, Marc J J Vrakking, and Hiromichi Niikura. Population transfer to high angular momentum states in infrared-assisted XUV photoionization of helium. *Journal of Physics B: Atomic, Molecular and Optical Physics*, 53(16):164003, jul 2020.

[37] R. R. Freeman, P. H. Bucksbaum, H. Milchberg, S. Darack, D. Schumacher, and M. E. Geusic. Above-threshold ionization with subpicosecond laser pulses. *Phys. Rev. Lett.*, 59:1092–1095, Sep 1987.

[38] Lars Jönsson. Energy shifts due to the ponderomotive potential. *J. Opt. Soc. Am. B*, 4(9):1422–1425, Sep 1987.

[39] P. H. Bucksbaum, R. R. Freeman, M. Bashkansky, and T. J. McIlrath. Role of the ponderomotive potential in above-threshold ionization. *J. Opt. Soc. Am. B*, 4(5):760–764, May 1987.

[40] R R Freeman and P H Bucksbaum. Investigations of above-threshold ionization using subpicosecond laser pulses. *Journal of Physics B: Atomic, Molecular and Optical Physics*, 24(2):325–347, jan 1991.

[41] Donald H Bilderback, Pascal Elleaume, and Edgar Weckert. Review of third and next generation synchrotron light sources. *Journal of Physics B: Atomic, Molecular and Optical Physics*, 38(9):S773–S797, apr 2005.

[42] Joachim Ullrich, Artem Rudenko, and Robert Moshammer. Free-Electron Lasers: New Avenues in Molecular Physics and Photochemistry. *Annual Review of Physical Chemistry*, 63(1):635–660, 2012. PMID: 22404584.

[43] John M. J. Madey. Stimulated Emission of Bremsstrahlung in a Periodic Magnetic Field. *Journal of Applied Physics*, 42(5):1906–1913, 1971.

[44] A. M. Kondratenko and E. L. Saldin. Generation of coherent radiation in an ondulator by a relativistic electron beam. *Zhurnal Tekhnicheskoj Fiziki*, 51(8):1633–1642, 1981.

[45] V. Ayvazyan, N. Baboi, J. Bähr, V. Balandin, B. Beutner, A. Brandt, I. Bohnet, A. Bolzmann, R. Brinkmann, Brovko, et al. First operation of a free-electron laser generating GW power radiation at 32 nm wavelength. *The European Physical Journal D - Atomic, Molecular, Optical and Plasma Physics*, 37(2):297–303, Feb 2006.

[46] E. Allaria, R. Appio, L. Badano, W. A. Barletta, S. Bassanese, S. G. Biedron, A. Borga, E. Busetto, D. Castronovo, Cinquegrana, et al. Highly coherent and stable pulses from the FERMI seeded free-electron laser in the extreme ultraviolet. *Nature Photonics*, 6(10):699–704, Oct 2012.

[47] Tetsuya Ishikawa, Hideki Aoyagi, Takao Asaka, Yoshihiro Asano, Noriyoshi Azumi, Teruhiko Bizen, Hiroyasu Ego, Kenji Fukami, Toru Fukui, Yukito Furukawa, et al. A compact X-ray free-electron laser emitting in the sub-ångström region. *Nature Photonics*, 6(8):540–544, Aug 2012.

[48] P. Emma, R. Akre, J. Arthur, R. Bionta, C. Bostedt, J. Bozek, A. Brachmann, P. Bucksbaum, R. Coffee, Decker, et al. First lasing and operation of an ångstrom-wavelength free-electron laser. *Nature Photonics*, 4(9):641–647, Sep 2010.

[49] W. Decking, S. Abeghyan, P. Abramian, A. Abramsky, A. Aguirre, C. Albrecht, P. Alou, M. Altarelli, P. Altmann, Amyan, et al. A MHz-repetition-rate hard X-ray free-electron laser driven by a superconducting linear accelerator. *Nature Photonics*, 14(6):391–397, Jun 2020.

[50] Christopher J. Milne, Thomas Schietinger, Masamitsu Aiba, Arturo Alarcon, Juergen Alex, Alexander Anghel, Vladimir Arsov, Carl Beard, Paul Beaud, Simona Bettoni, et al. SwissFEL: The Swiss X-ray Free Electron Laser. *APPLIED SCIENCES-BASEL*, 7(7), JUL 2017.

[51] Heung-Sik Kang, Chang-Ki Min, Hoon Heo, Changbum Kim, Haeryong Yang, Gyujin Kim, Inhyuk Nam, Soung Youl Baek, Hyo-Jin Choi, Geonyeong Mun, et al. Hard X-ray free-electron laser with femtosecond-scale timing jitter. *NATURE PHOTONICS*, 11(11):708+, NOV 2017.

[52] Zhentang Zhao, Dong Wang, Qiang Gu, Lixin Yin, Ming Gu, Yongbin Leng, and Bo Liu. Status of the SXFEL Facility. *Applied Sciences*, 7(6), 2017.

[53] John N. Galayda. The lcls-ii: A high power upgrade to the lcls. *9th International Particle Accelerator Conference (IPAC2018)*, pages 18–23, 2018.

[54] Siegfried Schreiber and Bart Faatz. The free-electron laser flash. *High Power Laser Science and Engineering*, 3:e20, 2015.

[55] E A Seddon, J A Clarke, D J Dunning, C Masciovecchio, C J Milne, F Parmigiani, D Rugg, J C H Spence, N R Thompson, K Ueda, et al. Short-wavelength free-electron laser sources and science: a review. *Reports on Progress in Physics*, 80(11):115901, oct 2017.

[56] TESLA Test Facility Linac: Design report. Version 1.0, March 1, 1995. 10 1995.

[57] B Faatz, E Plönjes, S Ackermann, A Agababyan, V Asgekar, V Ayvazyan, S Baark, N Baboi, V Balandin, N von Bargen, et al. Simultaneous operation of two soft x-ray free-electron lasers driven by one linear accelerator. *New Journal of Physics*, 18(6):062002, jun 2016.

[58] C. Pellegrini, A. Marinelli, and S. Reiche. The physics of x-ray free-electron lasers. *Rev. Mod. Phys.*, 88:015006, Mar 2016.

[59] Brian W. J. McNeil and Neil R. Thompson. X-ray free-electron lasers. *Nature Photonics*, 4(12):814–821, Dec 2010.

[60] A. M. Kondratenko and E. L. Saldin. Generation of coherent radiation in an ondulator by a relativistic electron beam. *Zhurnal Tekhnicheskoj Fiziki*, 51(8):1633–1642, 1981.

[61] R. Bonifacio, C. Pellegrini, and L.M. Narducci. "collective instabilities and high-gain regime in a free electron laser". *Optics Communications*, 50(6):373 – 378, 1984.

[62] Rosen Ivanov, Ivette J Bermúdez Macias, Jia Liu, Günter Brenner, Juliane Roensch-Schulenburg, Gabor Kurdi, Ulrike Frühling, Katharina Wenig, Sophie Walther, Anastasios Dimitriou, Markus Drescher, Irina P Sazhina, Andrey K Kazansky, Nikolay M Kabachnik, and Stefan Düsterer. Single-shot temporal characterization of XUV pulses with duration from ∼10 fs to ∼350 fs at FLASH. *Journal of Physics B: Atomic, Molecular and Optical Physics*, 53(18):184004, jul 2020.

[63] Markus Braune, Günter Brenner, Siarhei Dziarzhytski, Pavle Juranić, Andrey Sorokin, and Kai Tiedtke. A non-invasive online photoionization spectrometer for FLASH2. *Journal of Synchrotron Radiation*, 23(1):10–20, Jan 2016.

[64] Ulrike Frühling, Marek Wieland, Michael Gensch, Thomas Gebert, Bernd Schütte, Maria Krikunova, Roland Kalms, Filip Budzyn, Oliver Grimm, Jörg Rossbach, Elke Plönjes, and Markus Drescher. Single-shot terahertz-field-driven X-ray streak camera. *Nature Photonics*, 3(9):523–528, Sep 2009.

[65] S. Düsterer, M. Rehders, A. Al-Shemmary, C. Behrens, G. Brenner, O. Brovko, M. DellAngela, M. Drescher, B. Faatz, J. Feldhaus, U. Frühling, N. Gerasimova, N. Gerken, C. Gerth, T. Golz, A. Grebentsov, E. Hass, K. Honkavaara, V. Kocharian, M. Kurka, Th. Limberg, R. Mitzner, R. Moshammer, E. Plönjes, M. Richter, J. Rönsch-Schulenburg, A. Rudenko, H. Schlarb, B. Schmidt, A. Senftleben, E. A. Schneidmiller, B. Siemer, F. Sorgenfrei, A. A. Sorokin, N. Stojanovic, K. Tiedtke, R. Treusch, M. Vogt, M. Wieland, W. Wurth, S. Wesch, M. Yan, M. V. Yurkov, H. Zacharias, and S. Schreiber. Development of experimental techniques for the characterization of ultrashort photon pulses of extreme ultraviolet free-electron lasers. *Phys. Rev. ST Accel. Beams*, 17:120702, Dec 2014.

[66] T. A. Callcott, K. L. Tsang, C. H. Zhang, D. L. Ederer, and E. T. Arakawa. HighâĂŘefficiency soft xâĂŘray emission spectrometer for use with synchrotron radiation excitation. *Review of Scientific Instruments*, 57(11):2680–2690, 1986.

[67] C. Dallera, E. Puppin, G. Trezzi, N. Incorvaia, A. Fasana, L. Braicovich, N. B. Brookes, and J. B. Goedkoop. Soft X-ray Emission Spectroscopy at ESRF Beamline 26 Based on a Helical Undulator. *Journal of Synchrotron Radiation*, 3(5):231–238, Sep 1996.

[68] T. Tanikawa, A. Hage, M. Kuhlmann, J. Gonschior, S. Grunewald, E. Plönjes, S. Düsterer, G. Brenner, S. Dziarzhytski, M. Braune, M. Brachmanski, Z. Yin,

F. Siewert, T. Dzelzainis, B. Dromey, M.J. Prandolini, F. Tavella, M. Zepf, and B. Faatz. First observation of SASE radiation using the compact wide-spectral-range XUV spectrometer at FLASH2. *Nuclear Instruments and Methods in Physics Research Section A: Accelerators, Spectrometers, Detectors and Associated Equipment*, 830:170–175, 2016.

[69] S. Düsterer, P. Radcliffe, G. Geloni, U. Jastrow, M. Kuhlmann, E. Plönjes, K. Tiedtke, R. Treusch, J. Feldhaus, P. Nicolosi, L. Poletto, P. Yeates, H. Luna, J. T. Costello, P. Orr, D. Cubaynes, and M. Meyer. Spectroscopic characterization of vacuum ultraviolet free electron laser pulses. *Opt. Lett.*, 31(11):1750–1752, Jun 2006.

[70] T. Lang, S. Alisauskas, U. GroÃ§e-Wortmann, T. Hülsenbusch, B. Manschwetus, C. Mohr, J. Müller, F. Peters, N. Schirmel, S. Schulz, A. Swiderski, J. Zheng, and I. Hartl. Versatile opcpa pump-probe laser system for the flash2 xuv fel beamline at desy. In *2019 Conference on Lasers and Electro-Optics Europe European Quantum Electronics Conference (CLEO/Europe-EQEC)*, pages 1–1, 2019.

[71] Elisa Appi, Christina C. Papadopoulou, Jose Louise Mapa, Nishad Wesavkar, Christoph Jusko, Philip Mosel, Skirmantas Ališauskas, Tino Lang, Christoph M. Heyl, Bastian Manschwetus, et al. A synchronized VUV light source based on high-order harmonic generation at FLASH. *Scientific Reports*, 10(1):6867, Apr 2020.

[72] Maurizio Reduzzi, Johan Hummert, Antoine Dubrouil, Francesca Calegari, Mauro Nisoli, Fabio Frassetto, Luca Poletto, Shaohao Chen, Mengxi Wu, Mette B. Gaarde, Kenneth Schafer, and Giuseppe Sansone. Polarization control of absorption of virtual dressed states in helium. *Phys. Rev. A*, 92:033408, Sep 2015.

[73] Michael Chini, Xiaowei Wang, Yan Cheng, Yi Wu, Di Zhao, Dmitry A. Telnov, Shih-I Chu, and Zenghu Chang. Sub-cycle Oscillations in Virtual States Brought to Light. *Scientific Reports*, 3(1):1105, Jan 2013.

[74] M. Justine Bell, Annelise R. Beck, Hiroki Mashiko, Daniel M. Neumark, and Stephen R. Leone. Intensity dependence of light-induced states in transient absorption of laser-dressed helium measured with isolated attosecond pulses. *Journal of Modern Optics*, 60(17):1506–1516, 2013.

[75] Shaohao Chen, M. Justine Bell, Annelise R. Beck, Hiroki Mashiko, Mengxi Wu, Adrian N. Pfeiffer, Mette B. Gaarde, Daniel M. Neumark, Stephen R. Leone, and Kenneth J. Schafer. Light-induced states in attosecond transient absorption spectra of laser-dressed helium. *Phys. Rev. A*, 86:063408, Dec 2012.

[76] P O'Keeffe, A Mihelič, P Bolognesi, M Žitnik, A Moise, R Richter, and L Avaldi. Near-threshold photoelectron angular distributions from two-photon resonant photoionization of He. *New Journal of Physics*, 15(1):013023, jan 2013.

[77] S Mondal, H Fukuzawa, K Motomura, T Tachibana, K Nagaya, T Sakai, K Matsunami, S Yase, M Yao, S Wada, et al. Photoelectron angular distributions in infrared one-photon and two-photon ionization of FEL-pumped Rydberg states of helium. *Journal of Physics B: Atomic, Molecular and Optical Physics*, 46(20):205601, oct 2013.

[78] A. Kramida, Yu. Ralchenko, J. Reader, and and NIST ASD Team. NIST Atomic Spectra Database (ver. 5.8), [Online]. Available: https://physics.nist.gov/asd [2021, January 15]. National Institute of Standards and Technology, Gaithersburg, MD., 2020.

[79] P Ranitovic, X M Tong, B Gramkow, S De, B DePaola, K P Singh, W Cao, M Magrakvelidze, D Ray, I Bocharova, H Mashiko, A Sandhu, E Gagnon, M M Murnane, HC Kapteyn, I Litvinyuk, and C L Cocke. IR-assisted ionization of helium by attosecond extreme ultraviolet radiation. *New Journal of Physics*, 12(1):013008, jan 2010.

[80] Louis H. Haber, Benjamin Doughty, and Stephen R. Leone. Continuum phase shifts and partial cross sections for photoionization from excited states of atomic helium measured by high-order harmonic optical pump-probe velocity map imaging. *Phys. Rev. A*, 79:031401, Mar 2009.

[81] Mengxi Wu, Shaohao Chen, Seth Camp, Kenneth J Schafer, and Mette B Gaarde. Theory of strong-field attosecond transient absorption. *Journal of Physics B: Atomic, Molecular and Optical Physics*, 49(6):062003, feb 2016.

[82] N B Delone and Vladimir P Krainov. AC Stark shift of atomic energy levels. *Physics-Uspekhi*, 42(7):669–687, jul 1999.

[83] Michael Chini, Xiaowei Wang, Yan Cheng, and Zenghu Chang. Resonance effects and quantum beats in attosecond transient absorption of helium. *Journal of Physics B: Atomic, Molecular and Optical Physics*, 47(12):124009, jun 2014.

[84] J. Mauritsson, T. Remetter, M. Swoboda, K. Klünder, A. L'Huillier, K. J. Schafer, O. Ghafur, F. Kelkensberg, W. Siu, P. Johnsson, M. J. J. Vrakking, I. Znakovskaya, T. Uphues, S. Zherebtsov, M. F. Kling, F. Lépine, E. Benedetti, F. Ferrari, G. Sansone, and M. Nisoli. Attosecond Electron Spectroscopy Using a Novel Interferometric Pump-Probe Technique. *Phys. Rev. Lett.*, 105:053001, Jul 2010.

[85] Deutsches Elektronen-Synchrotron DESY. Free-electron laser flash, May 2021.

[86] MCCLAIN WM. Two-photon molecular spectroscopy. *ACCOUNTS CHEM. RES.; U.S.A.; DA. 1974; VOL. 7; NO 5; PP. 129-135; BIBL. 11 REF.*, 1974.

[87] Caroline E. H. Dessent and Klaus Müller-Dethlefs. Hydrogen-Bonding and van der Waals Complexes Studied by ZEKE and REMPI Spectroscopy. *Chemical Reviews*, 100(11):3999–4022, 2000. PMID: 11749337.

[88] Nimrod Moiseyev, Milan Šindelka, and Lorenz S Cederbaum. Laser-induced conical intersections in molecular optical lattices. *Journal of Physics B: Atomic, Molecular and Optical Physics*, 41(22):221001, nov 2008.

[89] M. Kübel, M. Spanner, Z. Dube, A. Yu. Naumov, S. Chelkowski, A. D. Bandrauk, M. J. J. Vrakking, P. B. Corkum, D. M. Villeneuve, and A. Staudte. Probing multiphoton light-induced molecular potentials. *Nature Communications*, 11(1):2596, May 2020.

[90] M. Braune, G. Hartmann, M. Ilchen, A. Knie, T. Lischke, A. Reinköster, A. Meissner, S. Deinert, L. Glaser, O. Al-Dossary, A. Ehresmann, A.S. Kheifets, and J. Viefhaus. Electron angular distributions of noble gases in sequential two-photon double ionization. *Journal of Modern Optics*, 63(4):324–333, 2016.

[91] Lazaros Varvarezos, Stefan Düsterer, Maksim D. Kiselev, Rebecca Boll, Cedric Bomme, Alberto De Fanis, Benjamin Erk, Christopher Passow, Sergei M. Burkov, Gregor Hartmann, Markus Ilchen, Per Johnsson, Thomas J. Kelly, Bastian Manschwetus, Tommaso Mazza, Michael Meyer, Dimitrios Rompotis, Oleg Zatsarinny, Elena V. Gryzlova, Alexei N. Grum-Grzhimailo, and John T. Costello. Near-threshold two-photon double ionization of Kr in the vacuum ultraviolet. *Phys. Rev. A*, 103:022832, Feb 2021.

[92] P. A. Carpeggiani, E. V. Gryzlova, M. Reduzzi, A. Dubrouil, D. Faccialá, M. Negro, K. Ueda, S. M. Burkov, F. Frassetto, F. Stienkemeier, Y. Ovcharenko, M. Meyer, O. Plekan, P. Finetti, K. C. Prince, C. Callegari, A. N. Grum-Grzhimailo, and G. Sansone. Complete reconstruction of bound and unbound electronic wavefunctions in two-photon double ionization. *Nature Physics*, 15(2):170–177, Feb 2019.

[93] M D Kiselev, P A Carpeggiani, E V Gryzlova, S M Burkov, M Reduzzi, A Dubrouil, D Faccialá, M Negro, K Ueda, F Frassetto, F Stienkemeier, Y Ovcharenko, M Meyer, M Di Fraia, O Plekan, K C Prince, C Callegari, G Sansone, and A N Grum-Grzhimailo. Photoelectron spectra and angular distribution in sequential two-photon double ionization in the region of autoionizing resonances of ArII and KrII. *Journal of Physics B: Atomic, Molecular and Optical Physics*, 53(24):244006, nov 2020.

[94] Elena V. Gryzlova, Alexei N. Grum-Grzhimailo, Maksim D. Kiselev, and Sergey M. Burkov. Two-photon sequential double ionization of argon in the region of Rydberg autoionizing states of Ar+. *The European Physical Journal D*, 73(5):93, May 2019.

[95] M Kurka, A Rudenko, L Foucar, K U Kühnel, Y H Jiang, Th Ergler, T Havermeier, M Smolarski, S Schössler, K Cole, M Schöffler, R Dörner, M Gensch, S Düsterer, R Treusch, S Fritzsche, A N Grum-Grzhimailo, E V Gryzlova, N M Kabachnik, C D Schröter, R Moshammer, and J Ullrich. Two-photon double ionization of Ne by free-electron laser radiation: a kinematically complete experiment. *Journal of Physics B: Atomic, Molecular and Optical Physics*, 42(14):141002, jun 2009.

Erklärung:

Ich versichere, dass ich diese Arbeit selbstständig verfasst habe und keine anderen als die angegebenen Quellen und Hilfsmittel benutzt habe.

Heidelberg, den ....